Multi-spacecraft analysis of the solar coronal plasma

Von der Fakultät für Elektrotechnik, Informationstechnik, Physik
der Technischen Universität Carolo-Wilhelmina zu Braunschweig

zur Erlangung des Grades einer
Doktorin der Naturwissenschaften (Dr. rer. nat.)

genehmigte Dissertation

von Iulia Ana Maria Chifu

aus Bukarest, Rumänien

eingereicht am: 11.02.2015

Disputation am: 07.05.2015

1. Referent: Prof. Dr. Sami K. Solanki
2. Referent: Prof. Dr. Karl-Heinz Glassmeier

Druckjahr: 2016

Bibliografische Information der Deutschen Nationalbibliothek

Die Deutsche Nationalbibliothek verzeichnet diese Publikation in der Deutschen Nationalbibliografie; detaillierte bibliografische Daten sind im Internet über http://dnb.d-nb.de abrufbar.

Dissertation an der Technischen Universität Braunschweig,
Fakultät für Elektrotechnik, Informationstechnik, Physik

ISBN

uni-edition GmbH 2016
http://www.uni-edition.de

Printed in Germany

Vorveröffentlichung der Dissertation

Teilergebnisse aus dieser Arbeit wurden mit Genehmigung der Fakultät für Elektrotechnik, Informationstechnik, Physik, vertreten durch den Mentor der Arbeit, in folgenden Beiträgen vorab veröffentlicht:

Publikationen

- Mierla, M., Chifu, I., Inhester, B., Rodriguez, L., Zhukov, A., 2011, Low polarised emission from the core of coronal mass ejections, Astronomy and Astrophysics, 530, L1

- Chifu, I., Inhester, B., Mierla, M., Chifu, V., Wiegelmann, T., 2012, First 4D Reconstruction of an Eruptive Prominence Using Three Simultaneous View Directions, Solar Physics, 281, 121-135

- Mierla, M.; Seaton, D. B.; Berghmans, D.; Chifu, I.; De Groof, A.; Inhester, B.; Rodriguez, L.; Stenborg, G.; Zhukov, A. N., 2013, Study of a Prominence Eruption using PROBA2/SWAP and STEREO/EUVI Data, Solar Physics, 286, 241-253

- Chifu, I., Inhester, B., Wiegelmann, T., 2015, Coronal magnetic field modeling using stereoscopy constraints, Astronomy and Astrophysics, 577, 123

Tagungsbeiträge

- Chiricuta O., Chifu I., Besliu-Ionescu D., Mierla M., Studies of Solar - Terrestrial Connections: Geomagnetic Storms Induced by Coronal Mass Ejections in: Modern Topics in Astronomy Conference, Bucharest, Romania, 19 November 2010, (poster);

- Chiricuta O., Chifu I., Mierla M., Maris G., Study of Earth-directed Halo Coronal Mass Ejections observed between 1996 and 2008, Assessment and Validation of Space Weather Models, Alcala de Henares, Spain, 14 - 18 March 2011, (poster);

- Chifu I., Inhester B., 3D reconstruction of a prominence from three views, in: 4th SOLAIRE network meeting, Teistungen, Germany, 9 - 13 May 2011, (poster)

- Chifu I., Inhester B., 3D reconstruction of the eruptive prominence on 1 August 2010 from three views in Stereo4/SDO2/SOHO25 workshop, Kiel, Germany, 25-29 July 2011, (poster)

- Oprea C., Chifu I., Mierla M., The Dynamics of the 8 April 2010 Coronal Mass Ejection into the Interplanetary Space in AOGS - AGU (WPGM) Joint Assembly, Sentosa, Singapore, 13 - 17 August, 2012, (poster)
- Mierla M, Chifu I, Inhester B., Rodriguez L., Zhukov A., Low polarised emission from the core of coronal mass ejections in Nature of Prominences and their role in Space Weather, Paris, France, 10-14 June 2013, (oral)
- Chifu I., Inhester B., Wiegelmann Th, Coronal magnetic field modeling using stereoscopy constraints in IAUS300, Nature of Prominences and their role in Space Weather, Paris, France, 10-14 June 2013, (poster)

Contents

Abstract

The thesis “Multi-spacecraft analysis of the solar coronal plasma” deals with two different approaches in the analysis of the solar corona: an observational and a theoretical one.

The first approach aims at the reconstruction of the 3D structure of phenomena in the solar corona using data obtained by multiple spacecraft. We used observations from three spacecraft: Solar Terrestrial Relation Observatory (STEREO) A and B and Solar Dynamic Observatory. The observed and analyzed solar phenomena were prominences and CMEs. For the analysis of the observed phenomena we extended and applied a 3D stereoscopic reconstruction method, called MBSR (Multi-view B-spline Stereoscopic Reconstruction) which was developed as part of this thesis. The MBSR method has a large spectrum of possible applications to solar phenomena, from coronal loops to coronal mass ejections (CME). We applied the MBSR method to two eruptive prominences which evolved into CMEs.

In one of the events a bright patch of low polarized radiation was observed in coronagraph images of the CME core, which was presumably caused by a Hα resonant scattering. This effect is not common since at the usual coronal temperatures at the height of the analyzed CME, one expects the plasma to be fully ionized. The polarization ratio method failed to retrieve a meaningful location of the bright patch. Therefore, we applied the MBSR method and determined its probable 3D position in the CME core. For the second event we make use of simultaneous data from three space probes to reconstruct the 3D location of the highest ridge of a rising prominence and the core and leading edge of the CME which evolved from it. We follow the evolution of the eruption from the time of the initial rise of the prominence until the CME core leaves the field of view of the COR1 coronagraph. We calculate various parameters which characterize the 3D curves, such as the propagation direction, the rise velocity, the angular width of the prominence and of the CME core and their rotation.

The second approach is related to the extrapolation of the coronal magnetic field from a photospheric magnetogram using the NLFFF (non-linear force-free field) model. It is generally accepted that coronal loops observed in EUV images outline magnetic field lines. The results from many conventional magnetic field extrapolations show, however, large discrepancies between the extrapolated magnetic field lines and the observed coronal loops, typically they deviate by angles of the order of 20 degrees. We therefore introduced an additional observational constraint to the extrapolation scheme by requiring the field also reproduces 3D reconstructed coronal loops. This is achieved by minimizing the local angles between the extrapolated magnetic field and the tangents to the coronal loops. We call this new method stereoscopic - nonlinear force-free field (S-NLFFF) extrapolation method because the shape of the coronal loops is reconstructed from EUV images by stereoscopy. In the thesis we present the S-NLFFF method and tests of it with synthetic

data.

The thesis is structured in six chapters: in Chapter 1 we give an introduction to the studied solar coronal phenomena; in Chapter 2 we present the methods which we developed for analyzing prominences, coronal loops and CMEs as well as those for computing the coronal magnetic field. Already existing methods employed here are also described. in Chapter 3 we present the spacecraft and instruments which we have used for our data analysis. Chapter 4 presents the application of the MBSR code and the analysis of two coronal events. In Chapter 5 we present the tests for S-NLFFF model. Chapter 6 contains conclusions and a brief outlook.

Glossary

Acronyms

AIA	Atmospheric Image Assembly
AR	Active Region
AW	Angular Width
CME	Coronal Mass Ejections
COR	Coronagraph
DEM	Differential Emission Measure
EM	Emission Measure
EUV	Extreme Ultra Violet
EUVI	Extreme Ultra Violet Imager
HEEQ	Heliospheric Earth Equatorial
HI	Heliospheric Imager
LE	Leading Edge
LOS	Line Of Sight
LTE	Local Thermodynamic Equilibrium
MBSR	Multi-view B-spline Stereoscopic Reconstruction
MHD	Magnetohydrodynamics
NLFFF	NonLinear Force Free Field
PCTR	Prominence to Corona Transition Region
PIL	Photospheric Inversion Line
POS	Plane Of Sky
SDO	Solar Dynamic Observatory
SECCHI	Sun-Earth-Connection Coronal and Heliospheric Investigation
S-NLFFF	Stereoscopy-NonLinear Force Free Field
SOHO	Solar and Heliospheric Observatory
STEREO	Solar Terrestrial Relation Observatory
STPLN	STEREO Plane
SW	Solar Wind
UV	Ultra Violet

1 Physics of the solar corona

1.1 Introduction

The corona is the outer most layer of the solar atmosphere [1]. It starts at around 3000 km above the solar surface, but it does not have a well defined outer boundary. During a total solar eclipse, the solar corona can be observed very accurately. However, solar eclipses are relatively rare and short-lived events. Therefore, ground-based instruments which replace the Moon by an artificial occulter were constructed after the beginning of the 20th century.
The solar corona is highly influenced by the magnetic activity of the photosphere. We can observe this influence in Fig. 1.1 which shows two different snapshots of the solar corona during solar eclipses.

Figure 1.1: Images taken during two solar eclipses. The upper image was recorded in 2001 during maximum solar activity (http://www.mreclipse.com). In the lower panel we see an eclipse during minimum solar activity recorded in 1998 (http://solar-center.stanford.edu).

[1]The solar atmosphere is composed of four layers: the photosphere, the chromosphere, the transition region and the corona.

A strong magnetic activity at the photosphere corresponds to streamers, i.e. bright regions of closed field line oriented in all different directions. As the coronal plasma is trapped on magnetic field lines, the appearance of the corona is as in the upper panel of Fig. 1.1. In contrast, at low magnetic activity, coronal magnetic field is dominated by a bipolar configurations and the appearance of the coronal streamers is more elongated at the equatorial plane (lower panel of Fig. 1.1).

The coronal radiation in white-light, as observed during eclipses, has two components: F-corona and K-corona. The F-corona (F for Fraunhofer) is mostly present from approximately 2 $R_\odot$ (solar radii) and is due to the scattering of the photospheric light at the interplanetary dust particles. The spectrum of the F-corona shows the dark Fraunhofer absorption lines of the photospheric spectrum. The K-corona (K for “Kontinuum”) is due to the scattering of the photospheric light on the free electrons. Its continuous spectrum resembles the photospheric spectrum without the absorption lines (Stix 2002).

Another component of the solar corona is the E-corona (E from emission) which is due to the spectral emission (from radio waves to extreme ultra violet and X-rays) produced by highly ionized atoms at temperatures of millions of Kelvin. Fig. 1.2 shows two images of the solar corona in two emission wavelengths. In most emission lines the plasma is

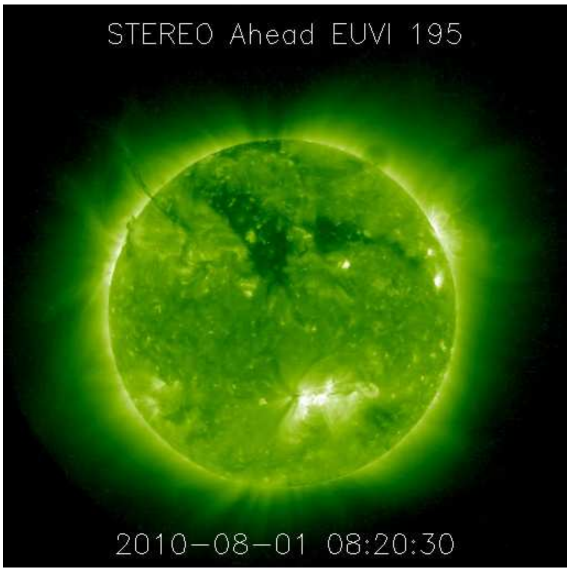

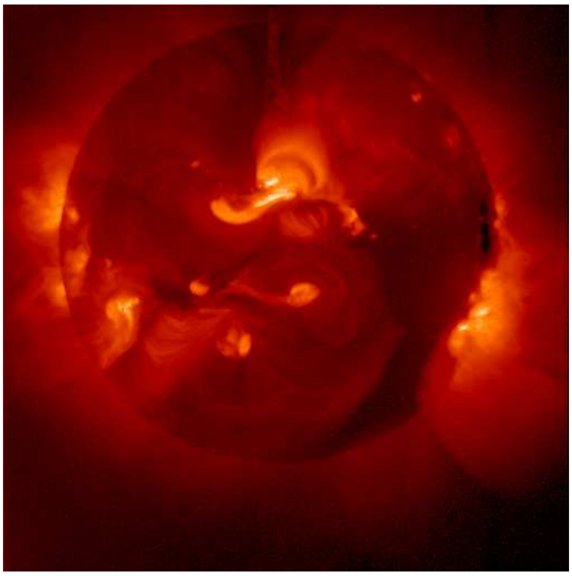

Figure 1.2: The left image shows the Sun in the emission line at $\lambda = 195$ Å of Fe XII recorded by EUVI onboard STEREO (http://cdaw.gsfc.nasa.gov). The right image was recorded by the Yohkoh spacecraft. It shows the Sun in the wavelength range between 3 – 45 Å of soft X-rays (http://solar.physics.montana.edu).

optically thin and hot with temperatures larger than 10 000 K, in a steady state and in ionization [2] and thermal equilibrium.

Some of the processes which contribute to the emission in the corona are:

- Spontaneous emission occurs when an electron falls from a higher energy level (E_n) to a lower energy level (E_m) with the emission of a photon with the energy

[2] The ionization equilibrium is the equilibrium between the collisional ionization and the radiative and di-electronic recombination (Aschwanden 2004).

$h\nu = E_n - E_m$.

- Free-free emission (also called bremsstrahlung) occurs when an electron with energy E_e is non-elastically scattered off an ion and emits a photon with the energy $h\nu = E_e - E_f$, where E_f is the energy of the out coming electron.

- Radiative recombination occurs when a free electron recombines with an ion. When the energy of the free electron is higher than the energy level in which was trapped (E_n), a photon is emitted with the energy $h\nu = \frac{1}{2}m_e v^2 - E_n$.

- Di-electronic recombination occurs when a free electron is captured into an excited state and at the same time a bound electron is excited followed by a decay of one or both of the electrons into a lower energy level.

For the theoretical understanding of the physics of the corona on large scales, we have to introduce the laws of magnetohydrodynamics. By "large scales" we here mean scales well beyond the ion gyroradius and the ion inertial length at which the coronal plasma can be described as a fluid. Typically, the above mentioned ion scales are only a few kilometers and well below the spatial resolution of current solar telescopes.

1.2 Magnetohydrodynamics

Magnetohydrodynamics (MHD) describes the dynamics of a highly conductive fluid ("hydro") in a magnetic field ("magneto").

MHD can be applied to fluids which fulfill certain criteria (Priest 1982):

- The fluid is electrically conductive.

- Plasma can be considered as a single fluid.[3]

- Plasma is electrically neutral ($n_+ - n_- << n_+, \approx n_-$ with the number densities of positive and negative ions).

- The evolution of the plasma is considered to be slow in the sense that its time-scale of evolution is larger than the collision times and its length-scale is larger than the mean free paths of individual particles, ions and electrons. The plasma is assumed to be in local thermodynamic equilibrium (LTE).

- Since material and phase speeds involved are much lower than the speed of light, the plasma evolution is treated non-relativistically.

The magnetohydrodynamic equations combine the non-relativistic approximation of Maxwell's equations and the Navier-Stokes equation for the dynamics of the neutral plasma extended by the Lorentz-force term, the adiabatic gas law, the continuity equation of the plasma and Ohm's law. As we are interested more in the magnetic field's behavior, we will present only the electromagnetic equations.

[3]The single fluid condition may be used due to the slow evolution of the electrons and the ions.

In the reduced form of Maxwell equations, the non-relativistic assumption above allows us to neglect the displacement current from Ampere's law:

$$\nabla \times \mathbf{B} = \mu_0 \mathbf{j} \,, \tag{1.1}$$

$$\nabla \times \mathbf{E} = -\frac{\partial \mathbf{B}}{\partial t} \,, \tag{1.2}$$

$$\nabla \cdot \mathbf{B} = 0 \,, \tag{1.3}$$

where **E** and **B** are the electric and magnetic field, **j** represents the current density and μ_0 is the magnetic permeability in vacuum. The Ohm's law gives the relation between the current density and the total electric field:

$$\mathbf{j} = \sigma(\mathbf{E} + \mathbf{v} \times \mathbf{B}) \,, \tag{1.4}$$

where **v** is the flow velocity and σ is the electric conductivity assumed here to be isotropic.

A very important equation for solar physics which describes the evolution of the magnetic field with time when the velocity field is known, is the induction equation. The induction equation can be obtain from Maxwell's equations combined with Ohm's law. Rewriting the Ohm's law (Eq. 1.4) as $-\mathbf{E} = \mathbf{v} \times \mathbf{B} - \mathbf{j}/\sigma$, applying the curl operator on the new equation, then inserting into it the Faraday (Eq. 1.2) and Ampere's law (Eq. 1.1) and using the vector triple product, we obtain the induction equation:

$$\frac{\partial \mathbf{B}}{\partial t} = \nabla \times (\mathbf{v} \times \mathbf{B}) + \frac{1}{\mu_0 \sigma} \nabla^2 \mathbf{B} \,, \tag{1.5}$$

We can introduce $\eta = 1/(\mu_0 \sigma)$, which is called the magnetic diffusivity. The induction equation is valid in this form for a constant σ. The ratio between the two terms from the right hand side of the induction equation (1.5) is called magnetic Reynolds number and indicates when one of the two terms can be omitted to lowest order:

$$R_m = \frac{|\nabla \times (\mathbf{v} \times \mathbf{B})|}{|\eta \Delta \mathbf{B}|} \,. \tag{1.6}$$

For a typical length scale l_0 and velocity V_0, Reynolds number can be approximated with $R_m \approx \frac{V_0 l_0}{\eta}$.

When $R_m << 1$ the Lorentz force is small and we are in the diffusive limit. In this case, the time change of the magnetic field is characterized by the diffusive term, $\eta \nabla^2 \mathbf{B} = \eta B/(l_0)^2$. In this diffusive limit, the magnetic field can move freely through the plasma. For a certain length scale l_0, magnetic field diffuses according to a diffusion time scale given by $\tau_d = l_0^2/\eta$. In a fully ionized plasma the diffusion time scale depends on the plasma temperatures, $\tau_d \approx 10^{-9} \left[\frac{l_0}{\mathrm{Mm}}\right]^2 \left[\frac{T}{\mathrm{K}}\right]^{-3/2}$ s. For the solar corona, where the typical length scale is $l_0 = 10^6$ m and typical temperature is $T = 10^6$ K, we obtain a diffusion time scale of $\tau_d \approx 10^{12}$s ≈ 31710 years.

For a typical velocity in the corona of $\approx 10^3$ ms^{-1}, the Reynolds number amounts to $R_m = \frac{l_0}{V_0}\tau_d \cong 10^{10}$. Therefore, for the corona the conducting limit applies($R_m >> 1$). In this case the evolution of the magnetic field is described by $\frac{\partial \mathbf{B}}{\partial t} = \nabla \times (\mathbf{v} \times \mathbf{B})$ which means that the plasma can move freely along the field lines but for motion perpendicular to the magnetic field lines the plasma and the field are intimately tied together. This is the so-called frozen-in flux condition.

1.3 Plasma beta

Plasma β is the ratio of the plasma pressure over the magnetic pressure. Gary (2001) calculated the plasma beta in different regions of the solar atmosphere, above a solar active region. For these calculations, he combined a potential field magnetic model with various density and temperature observations at different heights. The resulting profile of the plasma beta with height above an active region from the photosphere is presented in Fig. 1.3. The gray area indicates the range of estimated β values. The left boundary

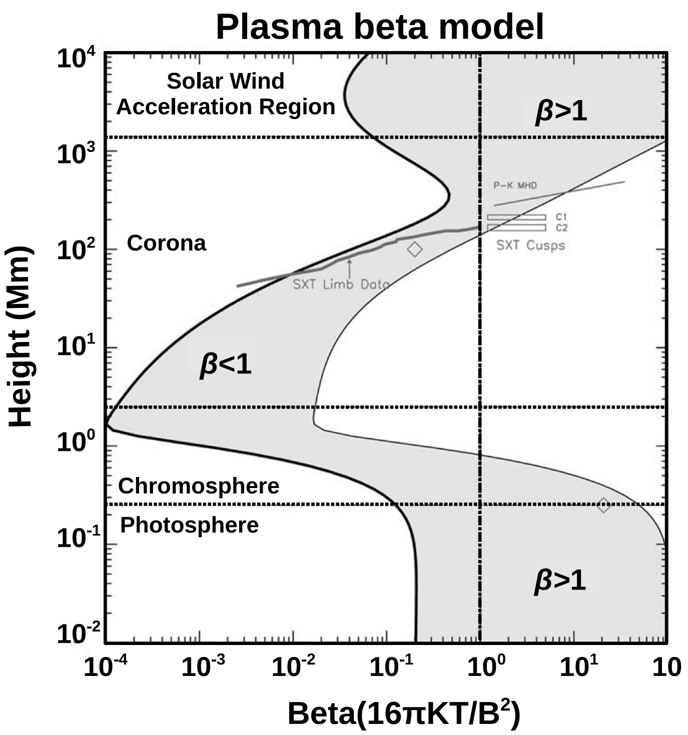

Figure 1.3: Approximate range of the plasma beta versus height above an active region in the solar atmosphere adapted from Gary (2001). The left boundary (black thick line) corresponds to the sunspot region while the right boundary corresponds to the plage area of the active region (Gary 2001).

of the gray area in Fig. 1.3 corresponds to a sunspot umbra. Because of the very strong magnetic field over the umbral area, the plasma beta remains less than unity at all heights down to the photosphere. The right hand side boundary in Fig. 1.3 corresponds to plage areas which occupy most of the active region (AR). According to this model (Fig. 1.3), in plage areas, β may rise to 100 which is the value assumed to dominate below the solar surface. But at coronal heights, above the transition region, β decreases well below unity.

If we consider a coronal temperature $T = 2 \cdot 10^6$ K and a number density $n = 1.2 \cdot 10^{16}$ m^{-3}, typical for bright loops from active regions (Reale 2010), we obtain a plasma pressure of

$$p = nK_BT = 0.5 \text{ Pa} , \tag{1.7}$$

where $K_B = 1.38 \cdot 10^{23}$ JK^{-1} is the Bolzmann constant. For a magnetic field of $B =$ 100 G $= 10^{-2}$ T, the plasma beta becomes

$$\beta = \frac{p}{B^2/2\mu_0} = \frac{2\mu_0 p}{B^2} = 0.01 , \tag{1.8}$$

where μ_0 is the vacuum permeability.

1.4 Creation and the emergence of the magnetic flux

The coronal magnetic field is generated below the solar surface. In order to understand how the magnetic field is created we need a short introduction to the inner layers of the Sun. The interior of the Sun is composed of three main layers, the core, the radiative zone and the convective zone. Much of the knowledge about these layers has been gained from modeling stellar evolution and more recently from helioseismological observations.

The core extends from the Sun's center to approximately 0.2 $R_\odot$. Here, the energy is generated by nuclear fusion of hydrogen. The temperature and the density drops (see Fig. 1.4) from $15 \cdot 10^6$ K at the center to $\approx 5 \cdot 10^6$ K at the outer boundary of the core, which causes the nuclear reaction rate to decrease towards the core boundary. The energy generated by fusion process is mainly set free in the form of high energy photons and neutrinos.

The radiative zone surrounds the core and extends to approximately 0.7 $R_\odot$. In this layer the high-energy photons produced inside the core are radiated to the outer layers of the Sun. The time for a photon to arrive at the outer boundary of this zone is very long due to its repeated scattering at free electrons. The temperature continues to drop from $5 \cdot 10^6$ K at the core boundary to $2 \cdot 10^6$ K at the outer boundary of the radiative zone (see Fig. 1.5).

The tachocline is a very thin layer centered at $\sim$ 0.7 $R_\odot$ and with a thickness of $\sim$ 0.04 $R_\odot$ (Charbonneau et al. 1999). Helioseismic observations have shown that at this interface region, between the radiative zone and the convective zone, the rotation which is approximately solid below, becomes latitude dependent (so called differential rotation) towards the surface, in the way that the Sun's equator rotates $\approx$ 28% faster than the pole regions.

The convection zone is the subsequent region which reaches up to the photosphere (see Fig. 1.4). The negative outward temperature gradient of three orders of magnitude provides the gravitationally unstable condition for an intense convection and an efficient

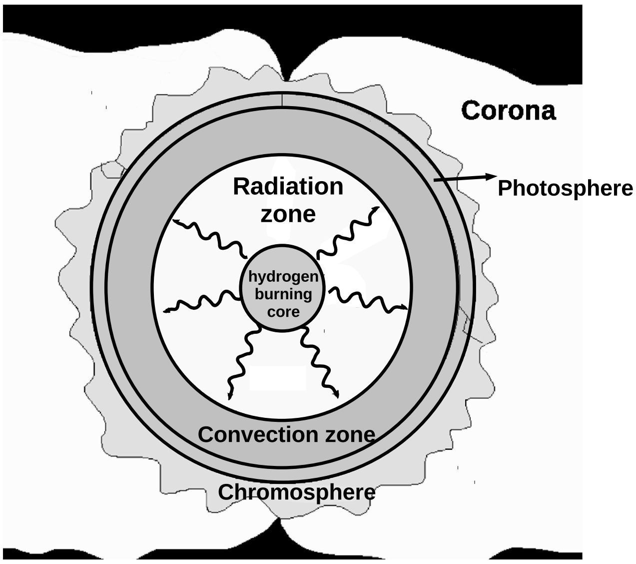

Figure 1.4: The internal structure of the Sun (adapted from http://www.astro.cornell.edu/academics/courses/astro201/sun_inside.htm).

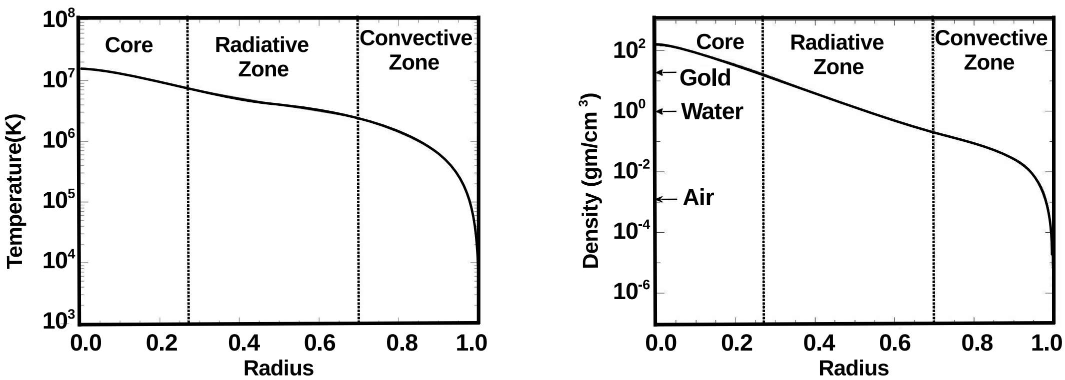

Figure 1.5: The radial temperature (left) and density (right) profiles in the Sun (adapted from http://solarscience.msfc.nasa.gov/interior.shtml).

transport of energy (Fig. 1.5). This layer is of great importance for the creation, sustenance and emergence of the magnetic flux in the outer layers.

At the bottom of the convection zone which coincides with the tachocline, the magnetic flux is generated by differential rotation (Fisher et al. 2000). The mechanism which generates and maintains the magnetic flux is considered to be a self-excited dynamo (Solanki et al. 2006). An essential ingredient of the solar dynamo is differential rotation. The essential conditions for the dynamo to work are:

1. high magnetic Reynolds number (Eq. 1.6). For the convection zone the typical value is estimated to be 500 (Brun 2004) in order to keep the magnetic flux frozen in the plasma movement.

2. non-axisymmetric field and flow [4]. The flow in the convection zone can be decomposed into a mean flow and a turbulent one.

3. the differential rotation is axisymmetric with respect to the solar rotation axis and anti-symmetric with respect to the equatorial plane.

The models which deal with the solar dynamo solve the magnetohydrodynamic equations, the induction equation and the equation of motion (Priest 1982). The magnetic field can be separated into its poloidal (B_p) and toroidal (B_t) component (Charbonneau 2010). Making use of the mean-field theory (the separation of fields into an average and a fluctuating part) applied to the induction equation, the two components of the magnetic field are revealed as solutions of the induction equation (Dikpati and Gilman 2009).

One concept which is considered to drive the solar convective zone dynamo is the so called $\alpha - \Omega$ effect combined with the meridional circulation of the convection zone (Dikpati and Gilman 2009). To illustrate the concept consider a poloidal field as an initial seed magnetic field. The Ω effect consists of a wrapping of the initial poloidal magnetic field by the differential rotation around the Sun (see Fig. 1.6 a).

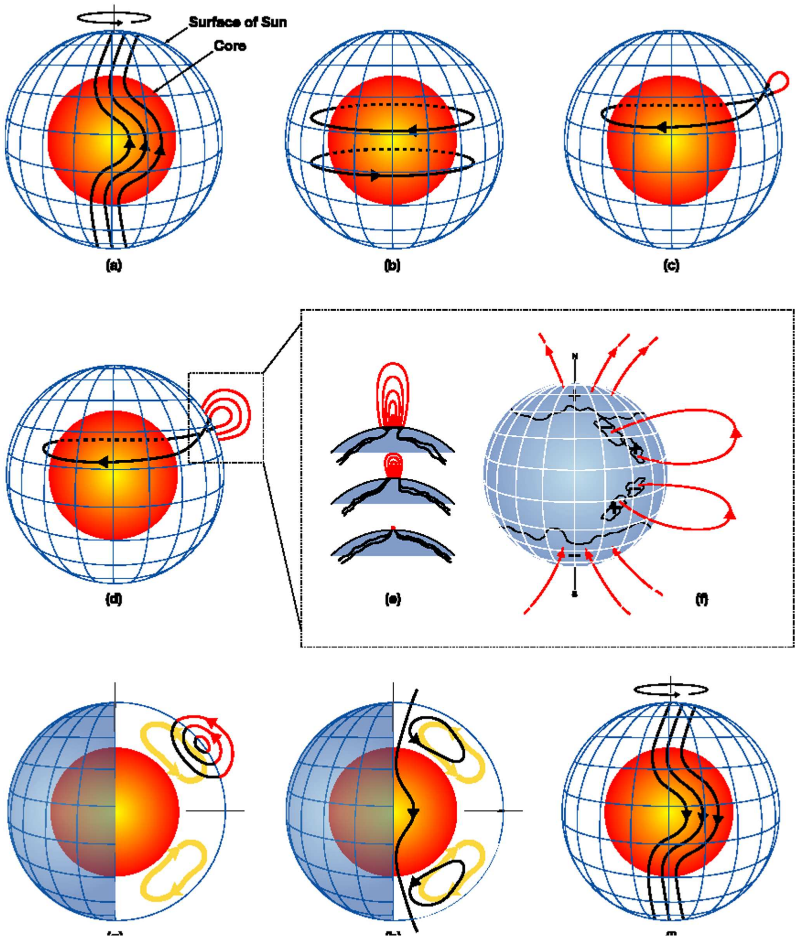

Figure 1.6: Idealized evolution steps of the dynamo action in the convection zone of the Sun taken from Dikpati and Gilman (2009).

[4] According to Cowling theorem a rotationally symmetric magnetic field (like a dipole field) cannot be maintain by dynamo (Solanki et al. 2006).

By this action the field changes into a strong toroidal field (see Fig. 1.6 b). The toroidal field is transported to the surface of the Sun by the convective motions. During the transport through the convective zone the toroidal field exhibits a kink due to the Coriolis force (α effect) (see Fig. 1.6 c, d).

Meridional flow (see Fig. 1.6 g) transport the magnetic fluxes from the Sun's surface along meridian lines polward. Some of the flux is then transported from the poles to the equator below the surface (Dikpati and Gilman 2009). Various observations have proven the existence of a poleward meridional flow of about 10-20 m s^{-1} in the near-surface layer. The observation could not reveal the equatorward return flow expected below the near surface layer. Dikpati and Gilman (2009) argue that the return flow must exist because the mass cannot pile up at the solar poles.

As we mentioned earlier, the plasma is transported from interior of the Sun to its surface (photosphere) by convection. The temperature gradient in most of the convective zone is nearly adiabatic except close to the surface where it becomes super-adiabatic. The adiabatic temperature gradient is a direct consequence of the convective motion. The super-adiabatic gradient near the surface is due to the cooling of the surface plasma by radiation into space. The observable consequence of convection at the photosphere is the appearance of the granulation (see Fig. 1.7), organized in so-called convective cells.

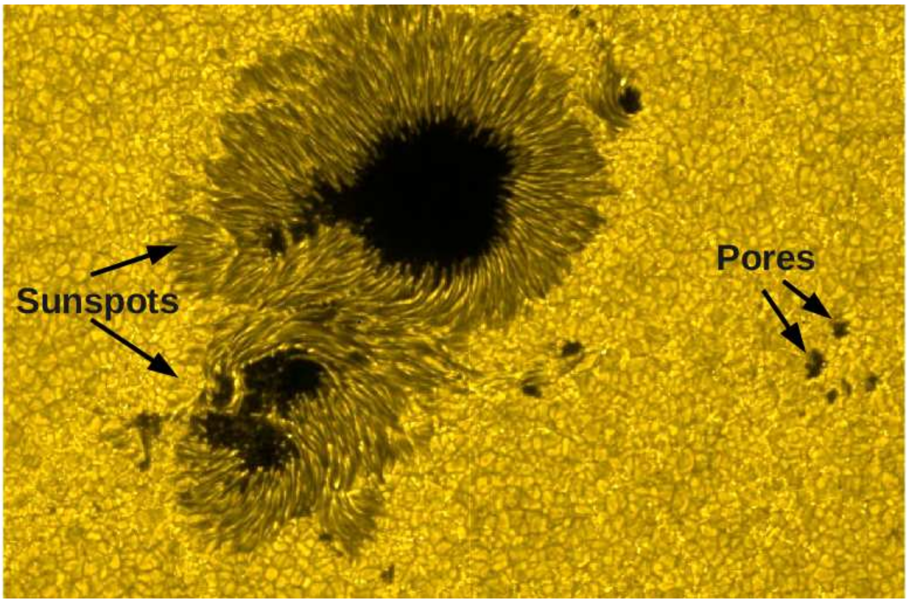

Figure 1.7: View of sunspots, pores and granules (in the remaining area outside sunspots and pores) recorded with the SOT (Solar Optical Telescope) on board Hinode spacecraft (adapted from http://www.nasa.gov).

As a result of the convective motion in the cells at the surface, the magnetic flux penetrating the surface is pushed into the inter-granular downflow lanes between the convection cells (Solanki et al. 2006).

Sunspots (Fig. 1.7) are the manifestation of large magnetic flux concentrations at the solar surface (Solanki et al. 2006). From an azimuthally oriented magnetic flux tube located in the deep convection zone, strands of magnetic flux become detached and rise to the surface where they emerge and form bipolar magnetic regions and sunspots (Solanki et al. 2006).

Well below solar surface, the sunspot flux tube can be modeled in ideal MHD by a thin flux tube surrounded by field-free plasma. The flux tube is thin in the sense that its diameter is smaller than the other physical relevant length scales (Fisher et al. 2000). The forces acting on the dynamic flux tube are the buoyancy force, the Coriolis force, the magnetic tension force, the hydrodynamic drag force. The enhanced magnetic pressure in the flux tube is compensated by a reduced density which gives rise to an upward buoyancy force (Solanki et al. 2006, Parker 1975).

1.5 The magnetic field in the solar corona

While below the solar surface β is large and the magnetic field is pushed around almost passively by the convective flow, in the solar corona this condition changes. In the corona $\beta << 1$ and we find that the magnetic field imposes its shape on a variety of coronal structures. We can find the magnetic field in the shape of coronal loops and streamers, of plumes in the "open" field of the coronal holes or as arcades in the prominence systems. The plasma density variation along the field lines in these phenomena is often assumed to be in a hydrostatic equilibrium. This allows to deduce the temperatures from the variation of the plasma density with height (Aschwanden 2004).

Sometimes, coronal loops or magnetic arcades in prominence structures are observed to be in steady state for a quite long period of time. The respective regions of the corona can therefore be assumed to be close to a magneto-hydrostatic equilibrium. In this case, the main forces acting on a plasma volume element, the plasma pressure, the gravity force and Lorenz force, are in balance:

$$-\nabla p + \rho \mathbf{g} + \mathbf{j} \times \mathbf{B} = 0 \; . \tag{1.9}$$

Here p and ρ are the plasma pressure and density, $\mathbf{j}$ is the current density and $\mathbf{B}$ is the magnetic field.

1.5.1 Active region loops

1.5.1.1 Introduction

Active regions (AR) are localized regions on the solar surface from which strong magnetic fields emerge, most often in two nearby areas of opposite polarity. During the active region development, the intense changes of the magnetic configuration (flux emergence, flux cancellation, changing in magnetic topology) can trigger dynamic processes like flares or coronal mass ejections (CMEs) (Aschwanden 2004). Due to their bipolar nature, active regions mostly form closed magnetic field lines (Aschwanden 2004). Active regions loops are magnetic flux tubes filled with a sufficient amount of hot plasma so that they radiate effectively in extreme ultra violet (EUV) wavelengths. In EUV images recorded by solar telescopes, the flux tubes are often observed to emerge from the low corona/chromosphere with at least one foot point rooted in an active region. Due to the low β of the solar corona, the plasma is well confined by the magnetic field. The low β in the corona allows to approximate a stationary magnetic coronal loop as an isolated mini-atmosphere in hydrostatic equilibrium (Aschwanden 2004) which has nearly the same temperature along its arc length (Petrie 2006), but varies between different flux tubes. The material inside the flux tubes is assumed as a compressible fluid moving and transporting energy only along the flux tubes (Reale 2010). Different conditions at the two foot-points can induce a considerable plasma and heat flow along the loop from one foot-point to the other (e.g. siphon flow).

1.5.1.2 Observations and models

Coronal loops are only visible on the solar disk in EUV and shorter wavelengths. Hence they could only be discovered after spacecraft equipped with EUV telescopes could escape the Earth's atmosphere. The first images of coronal loops were made by the Skylab spacecraft launched in 1973. The emission of plasma from the flux tubes at temperatures sampled by different EUV wavelength gives rise to the classification of cool, warm and hot loops (Reale 2010). Cool coronal loops are detected in ultraviolet (UV) lines emitted in thermodynamic equilibrium at temperatures between 10^5 K and 10^6 K. Warm loops have temperatures between 10^6 K and $1.5 \cdot 10^6$ K and are observed better in EUV lines and the hot loops emits around or above $2 \cdot 10^6$ K and are visible in X-ray observations.

The three type of loops can be part of the same bundle of loops emanating from one active region, while each of them emits at different wavelengths. An image recorded at a certain wavelength monitors the line-of-sight (LOS) integration of the radiation emitted by all the loops in that particular wavelength band.

The observed line intensity ($I_{\lambda_{ij}}$) emitted by the transition from an atomic level (j) to another (i) at the wavelength λ_{ij} from an ion X^{+m} is given by (Aschwanden 2004)

$$I_{\lambda_{ij}} = \frac{\hbar\nu_{ij}}{2i} \int N_j(X^{+m}) A_{ji} dh \; [\text{Kg m}^{-2}\text{s}^{-3}] \, , \tag{1.10}$$

where $\nu_{ij} = c/\lambda_{ij}$ is the wave frequency, A_{ji} is the Einstein coefficient for spontaneous emission, $N_j(X^{+m})$ is the number density of the emitting ion X^{+m} in the state of the upper level j and h is the line-of-sight coordinate. In the corona, in general, collisional excitation and ionization dominate over radiative processes. The population of the level j can be rewritten as

$$N_j(X^{+m}) = \frac{N_j(X^{+m})}{N(X^{+m})} \frac{N(X^{+m})}{N(X)} \frac{N(X)}{N(H)} \frac{N(H)}{N_e} N_e \, . \tag{1.11}$$

1. $\frac{N_j(X^{+m})}{N(X^{+m})}$ is the ratio of the number density of the ion X^{+m} excited at level j relative to the total number density of the ion X^{+m}.

2. $\frac{N(X^{+m})}{N(X)}$ represents the ratio of the number density of ion X^{+m} relative to the total number density of the element X.

3. $\frac{N(X)}{N(H)} = A_X$ is the element abundance relative to that of hydrogen.

4. $\frac{N(H)}{N_e}$ is the ratio of hydrogen number density to the electron density. For a fully ionized plasma, this ratio is ≈ 0.83.

The line intensity then can be written as

$$I_{\lambda_{ij}} = A_X \int C(T, \lambda_{ij}, N_e) N_e N_H dh \,, \tag{1.12}$$

$$C(T, \lambda_{ij}, N_e) = \frac{\hbar \nu_{ij}}{2} \frac{A_{ji}}{N_e} \frac{N_j(X^{+m})}{N(X^{+m})} \frac{N(X^{+m})}{N(X)} \,. \tag{1.13}$$

$C(T, \lambda_{ij}, N_e)$ is the contribution function which contains all the relevant atomic physics parameters and is peaked in a narrow temperature range through the temperature dependence of $N(X^{+m})/N(X)$. The temperature here is considered $T = T_e = T_{ion}$. The separation of the ratio $\frac{N(X)}{N(H)} = A_X$ from the contribution function arises from the assumption that the abundances are constant along the line-of sight. An alternative definition of the contribution function is

$$G_{ij}(T, \lambda_{ij}, A_X, N_e) = A_X C(T, \lambda_{ij}, N_e) \,. \tag{1.14}$$

Based on observational data of a certain line intensity $I(\lambda_{ij})$ at wavelength λ_{ij}, the contribution function can be calculated from the CHIANTI spectral code (Dere et al. 1997).

The most commonly used EUV lines for coronal observations are the emission lines of iron at different ionization levels. Fig. 1.8 shows coronal loops from an AR in different emission lines.

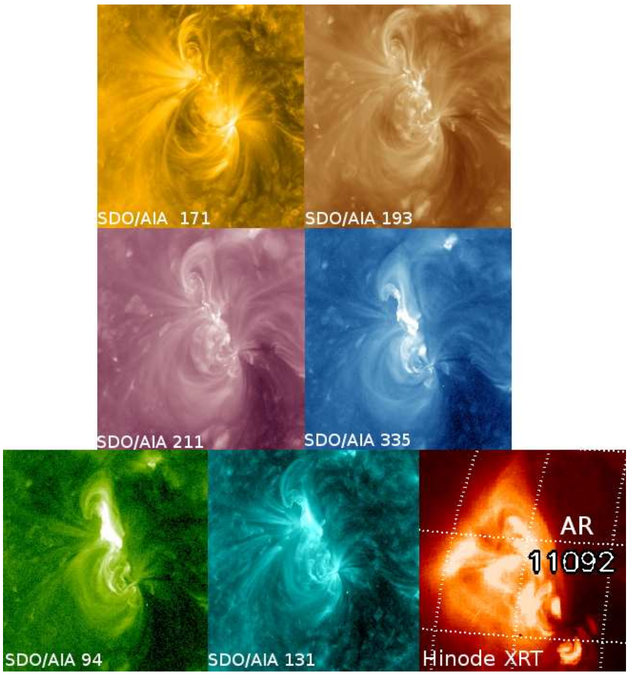

Figure 1.8: Coronal loops observed on 01 August 2010 with the AIA telescope on board the SDO spacecraft in the wavelengths of λ = 171Å (top left), λ = 193 Å (top right), 211 Å (middle left), 335 Å (middle right), 94 Å (bottom left) and 131 Å (bottom middle) (adapted from http://sdo.gsfc.nasa.gov/data/aiahmi/) and with XRT (X Ray Telescope) on board Hinode spacecraft (bottom right) (adapted from http://www.solarmonitor.org).

Typically, EUV intensity measurements are reduced to the differential emission measure (DEM) which is defined as the derivative of the emission measure (EM) with respect to the temperature ($DEM(T) = dEM(T)/dT = N_e N_H (dT/dh)^{-1}$. It is used in the approximation of local thermodynamic equilibrium and estimates the emitted intensity in terms of the local temperature and its gradient. Under the assumption of the density profile $N(h) = N_e(h) \approx N_H(h)$, the differential emission measure is expressed as $DEM(T) = N_e^2 (dT/dh)^{-1}$ where dT/dh is the gradient of the temperature along the LOS. The line intensity can be written in terms of the DEM as

$$I_{ij} = \frac{1}{4\pi} \int G_{ij}(T, \lambda_{ij}, A_X, N_e) DEM(T) dT \ . \tag{1.15}$$

With the CHIANTI code which consists of an atomic database and a suite of computer programs to calculate the optically thin emission spectrum of a large number of EUV lines (Landi et al. 2013), the differential emission measure of various EUV lines can be fitted to the observational data. This way information about the density and temperature at the emission site can be obtained. From the variation of emission measure with temperature $dEM(T)/dT \approx N_e^2(\Delta h/\Delta T)$, the squared average density can be estimated as it should be directly proportional to $dEM(T)/dT$ and inversely proportional to the local loop diameter Δh. This relation, $N_e^2(T) = (dEM(T)/dT)(\Delta T/\Delta h)$ can be estimated for a range of temperatures T (Aschwanden 2004).

Using observations of the DEM of coronal loops, Winebarger et al. (2011) suggested a stationary heating model of active region loops. They claim to be able to reproduce the density-sensitive spectral lines from the core of the AR and the DEM of the loops. Their model is based on the assumptions that the potential field extrapolation replicates the geometry of the AR core and the heating along a loop is constant.

The evolution of observational instruments and the increase in computational power allows the development of analysis techniques which reveal the physical characteristics in more detail. Using the DEM technique, Aschwanden (2011) developed an automatic code for the analysis of the temperature distribution not only over the entire Sun but also for structures like active region loops. Using observations from six different EUV wavelengths emitted from different iron ions, Aschwanden (2011) could built a temperature map for an active region (see Fig. 1.9). The authors concluded that the highest temperature in the active region is found in the core with values between $8 - 10 \cdot 10^6$ K (white part of the Fig. 1.9) while at the periphery of the AR, the temperatures are 1.5-2.5$\cdot 10^6$ K.

Under the assumption of local thermodynamic and hydrostatic equilibrium one can calculate the total emission measure (EM) of a loop from the integration of a known DEM over the whole temperature range. In such a calculation one has to take into account the LOS integration over all observed loops as the coronal plasma in the corona can be assumed to be optically thin in most EUV lines. One common assumption in these calculations is that the loops are isothermal.

A way to derive the temperature of the loop is to observe a coronal loop in two EUV emission lines. The observed intensities depend on the emission measure at the effective loop temperature and on instrument characteristics (Vaiana et al. 1973). The ratio of the two emission measures depends on the temperature and is independent of the local density if the pair of EUV lines are suitably chosen. The emission measure method is

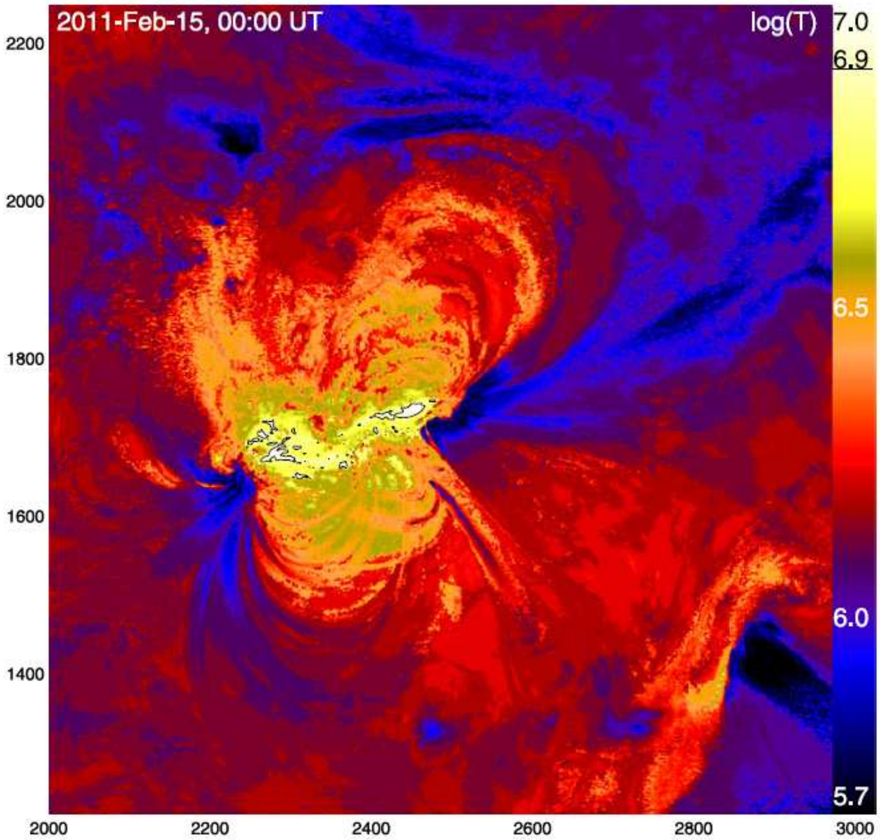

Figure 1.9: Temperature map derived using differential emission measure technique taken from Aschwanden (2011).

limited by the capability to separate the background emission of the solar surface or of other overlapping loops from the emission of the loop to be investigated. This difficulty also arises when the diagnostic is applied to loops above the limb (Reale 2010) because of scattering from the non-negligible coronal background.

Coronal loop models often treat the flux tubes as monolithic (static) and at equilibrium (Reale 2010) with a uniform temperature along the loop. They are assumed to be heated and cooled as an homogeneous unit (Klimchuk 2009). From observations, most of these loops live longer than their cooling time where the cooling time can be determined from observations. The cooling time depends on temperature, density and the length of the loop (Klimchuk 2009).

The structured (dynamic) types of loops are multi-stranded bundles often below observational resolution. The strands are dynamic, behave independently and are assumed to be heated impulsively. Averaged over the entire bundle, the entire loop appears to evolve slowly (Klimchuk 2009).

From observations at a pixel size larger than 1 arcsec, one often cannot distinguish clearly between different loops. With the launch of Solar Dynamic Observatory (SDO), it has become possible to continuously image the low corona in EUV wavelengths at a pixel size of 0.6 arcsec. Another instrument with an even higher resolution (0.1 arcsec/pixel) is High-resolution Coronal Imager (HI-C). Peter et al. (2013) did not find the substructures in Hi-C observations that are expected from the existence of resolvable loop bundles. Their conclusion was that the observed loops are either monolithic with diameter of typically 2 to 3 arcsec, or the loops are multi-stranded with the strand diameter below the HI-C resolution. According to their calculations, they derived a diameter of a strand to be about 15 km.

The heating mechanism of coronal loops and of the corona has been the topic of intensive research since a couple of years. The details of the conversion of magnetic energy which forms the dominant energy reservoir into thermal energy is still unsolved (Reale 2010). Currently there are two main mechanisms of coronal loop heating discussed, namely Direct Current (DC) heating through moderate and frequent explosive events (nanoflares) and Alternating Current (AC) heating by Alfvén waves (Reale 2010).

Winebarger et al. (2011) classified loop and heating models according to the number of strands which exist in a flux tube. If a coronal loop is composed of only one strand and the heating events occur infrequently, the temperature and density along the strand will strongly vary in time. The heating mechanism is then assumed to be the “nanoflare heating” mechanism. If the heating occurs almost continuously the temperature and density along the loop will reach an equilibrium and time variations in temperature and density are moderate. If the flux tube consists of few strands which encounter heat pulses almost simultaneously, the intensity of the loop will evolve in the same manner as the individual strands evolve. This heating scenario is called “short nanoflare storm” (Winebarger et al. 2011). A “long nanoflare storm” scenario takes place in the case that many sub-resolution strands are heated individually and randomly. The entire loop then evolves more smoothly in time according to the average strand.

Klimchuk (2009) concluded that EUV loops with temperature $\simeq 10^6$ K are composed of multiple strands which are heated by storms of nanoflares. In the case of loops with temperatures $> 2 \cdot 10^6$ K, the author found no clear evidence whether the nanoflare heating mechanism applies.

In another study Petrie (2006) analyzed the coronal loop widths and pressure scale heights using the approach of isothermal monolithic flux tubes with a steady-state plasma flow. He studied how the cross-section of the loop varies with height solving the mass flow conservation equation with the flux tube expansion taken into account. Motivated by Landi and Feldman (2004), who found that static loop models overestimate the foot-point emission by orders of magnitude, Reale (2010) concluded the necessity of introducing non-uniformity in the cross-section of the loop.

1.5.2 Prominences

1.5.2.1 Introduction

Prominences consist of dense, partially ionized plasma clouds with several thousand km above the solar surface sustained by the coronal magnetic field and embedded in the hot, highly ionized solar corona. When observed in detail, prominences are build from fine threads partially filled with cool material which outline magnetic flux tubes (Arregui et al. 2012). In general the main body of the prominence has a three part structure (the spine, the barbs, the legs). The spine is the main axis of the prominence, the legs are placed at the two ends of the spine and the barbs (see Fig. 1.10b) are fine striations which extend from the main axis sideways down to the chromosphere (Mackay et al. 2010).

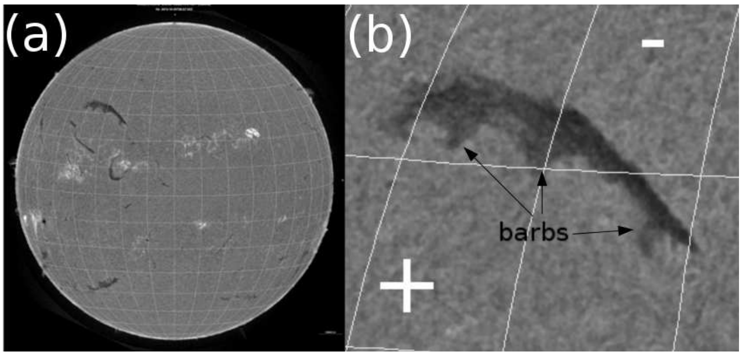

Figure 1.10: a) Cut from an image recorded in Hα emission by the BBSO (Big Bear Solar Observatory) showing dark filaments/prominences and b) a dark filament with barbs recorded in Hα emission by the BBSO.

The plasma which forms the prominences is kept in equilibrium by the magnetic field against gravity. Observers often distinguish between prominence and filament. The term prominence is used when it is observed above the solar limb as bright structure in the emission of hydrogen (see Fig. 1.10a) and helium. When observed on the solar disk a prominence appears dark and is also called a filament (see Fig. 1.10a). The dark appearance of prominences in Hα on the solar disk is due to the absorption of the incident radiation from the photosphere by the cool filament material (Solanki et al. 2006). Because prominences and filaments appear so different, it was not realized in the beginning of their observations that they are one and the same phenomenon. In the thesis I will use both terms synonymously.

Filaments are formed above photospheric inversion lines (PIL) between opposite magnetic polarities along a so-called filament channel, which is defined as the volume in which the filament will form and live. A necessary condition for the filaments to form is that the horizontal filament magnetic field has a component along the PIL (Martin 2000). Chromospheric fibrils (horizontal fine threads of plasma distributed over the solar surface) are often aligned with the surface horizontal field. Consequently, the fibrils cannot be normal to the PIL (filament channel) in sections where filaments may form. It is possible that a filament channel exists without being filled with chromospheric material (Martin 2000). Another condition for the formation of prominences is the existence of closed magnetic field arcades across the filament channel which connect the opposite polarities (Martin 1990). The sense of rotation of the oblique H_α fibrils relative to the PIL or to the filament axis defines the chirality of the filament (see Fig. 1.11). Typically, this sense of rotation is also shown by the barbs. The two senses of chirality are called dextral and sinistral (see Fig. 1.11). Fig. 1.10b shows an example of a filament with a sinistral chirality. Chirality is correlated with the sign of the magnetic helicity of the prominence flux tube. In general, negative magnetic helicity dominates in the northern hemisphere of the corona, while positive helicity dominates in the southern hemisphere (Pevtsov et al. 2003). In a similar way, the sense of the chirality differs in the two hemispheres. Studying the chirality of 2310 filaments, Pevtsov et al. (2003) found that almost 80% of the filaments follow the hemispheric helicity rule.

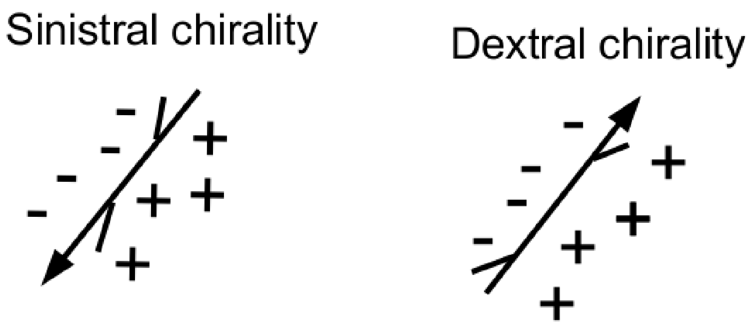

Figure 1.11: Sketch illustrating the chirality rule of filaments. The configuration from the left hand side is dominant in the southern hemisphere while the one from the right hand site is dominant in the northern hemisphere. The arrow represents the spine of the prominence while the lateral lines stands for the barbs.

Prominence foot points are rooted in the chromosphere, while most of the prominence mass resides in coronal heights. The mechanism by which the magnetic prominence structure is filled with cool plasma is still unclear.

The magnetic field plays a key role not only in the formation of the filament but also in its evolution and disappearance/eruption. Instabilities in the magnetic field can trigger eruptions of prominences which may evolve as coronal mass ejections (CMEs).

1.5.2.2 Observations

Prominences were observed long before the spacecraft era, first, during solar eclipses. The reddish color of prominences in these observations is due to the Hα (λ = 6562.8 Å) emission of the prominence plasma (see Fig. 1.12).

Figure 1.12: Crop of an image taken during an eclipse from 1991, which shows a prominence (http://www.company7.com/meade/gallery/11b.html).

Many of the prominence observations are made in this wavelength (see Fig. 1.10) and in the EUV (extreme ultra violet) wavelength of He II (λ = 304 Å). At 304 Å , filaments appear dark because of He II self-absorption.

In contrast, the brightness of the prominence with respect to the background when observed off-limb is due to the emission of the prominence plasma or to the scattering of the radiation emitted from the solar surface (see Fig. 1.13). The region which surrounds the prominence and where the temperature gradient is very high (from prominence temperatures to coronal temperatures) is called prominence to corona transition region (PCTR).

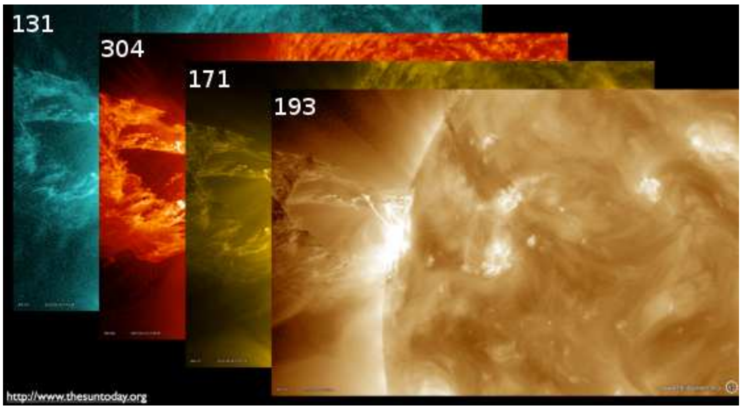

Figure 1.13: Composition of images of the same prominence observed in different EUV (extreme ultra-violet) wavelengths. From left to right at wavelength: λ = 131Å, 304 Å, 171Å, 193Å. The images were recorded by AIA onboard SDO (www.thesuntoday.org).

In some cases, the prominences can be observed in EUV emission lines of ionized iron at λ = 171, 193, 131 Å. These lines corresponds to equilibrium temperatures of $T = 0.6,\ 1.2\ , 10 \cdot 10^6$ K, respectively (Parenti et al. 2012). In these wavelengths, prominences appear dark also when observed above the limb. The bright background is in these observations provided by coronal emission. An explanation of the prominence emission for the low line intensity at these wavelengths has been given by Anzer and Heinzel (2005) who propose two responsible mechanisms. One mechanism is the absorption of a fraction of the coronal radiation from behind the prominence (when observed along LOS). The second explanation is the low emission from the prominence material (Parenti et al. 2012) in these hot coronal EUV lines.

Labrosse et al. (2010) proposed two models of the prominence structure which can explain observations in UV-EUV wavelengths. In one model, the prominence has a cool core surrounded by a thin transition layer which is hot enough to emit in the EUV spectrum. The second model assumes that the prominence is structured in isothermal threads with different temperatures some of which are hot enough to emit at UV-EUV wavelengths.

The prominences have been classified from their first observations. Secchi (1875) divided them into quiescent and active prominences. Petit (1925) separates prominences into five types: eruptive, tornado, quiescent, sunspot-related or active. Tandberg-Hanssen (1963) introduced a classification based on relative intensities of spectral lines from prominences observed in emission above the solar limb (Tandberg-Hanssen 1977).

Another classification of the prominences is based on their location and on the strength of the magnetic field. This classification distinguishes active region (AR) filaments (see Fig. 1.14, upper right image) and polar crown prominences, magnetic field configuration (dextral or sinistral), structures (as observed at limb) (arch-like or horizontal threads (see Fig. 1.14, bottom images) (Chifu et al. 2012).

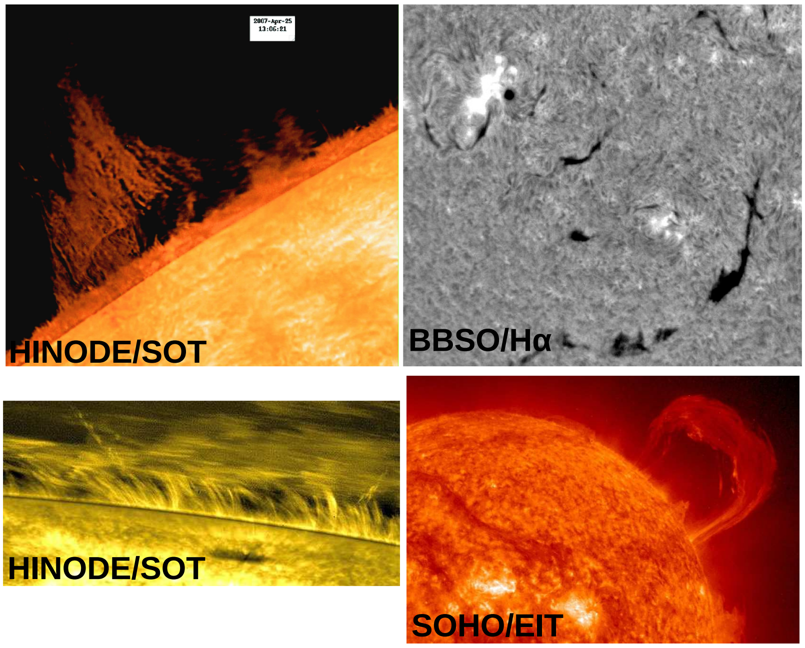

Figure 1.14: Different types of prominences. Images on the left side images were recorded SOT onboard Hinode, top right image by BBSO, bottom right image by EIT (Extreme ultraviolet Imaging Telescope) on board the SOHO (Solar and Heliospheric Observatory) spacecraft.

The strength and the dynamics of the magnetic field has significant impact on the morphology and lifetime of the prominences. The magnetic field in the active region is stronger and more dynamic than in quiet Sun regions. As a consequence, it is observed that the lifetime of the prominences above active regions is shorter than those which form in a weak magnetic field. This is the background for the classification in active and quiescent prominences. AR prominences/filaments can last from a few hours to days, while quiescent prominences can last for weeks (Gosain and Schmieder 2010).

The dimensions of prominences can vary significantly. Quiescent prominences can reach 10^5 km in length, 10^4 km in thickness and 10^5 km in height (Labrosse et al. 2010). while the AR prominences are smaller and barely reach 10^4 km in height (Filippov and Den 2000).

The typical temperature of prominences is substantially lower than typical coronal temperatures in which the prominence is suspended. Typical temperatures of prominence plasma spans between 6000 K and 80000 K (Anzer and Heinzel 2008).

It is considered that the temperature varies between threads, but also along each thread, which makes the determination of the temperature difficult. According to Park et al. (2013) the most common way to calculate the temperature in the core of a prominence is by measuring the absorption width of a spectral line. Ionization and excitation processes of the atoms in the prominence plasma depend on the temperature. Besides the thermal contribution to the line width one has to take into account the non-thermal broadening which might be due to unresolved LOS (line-of-sight) motions induced by waves or turbulence (Labrosse et al. 2010). In this case, the Doppler width is given by:

$$\Delta\lambda_D = \frac{\lambda}{c}\sqrt{\frac{2kT}{m} + \xi^2}\,, \tag{1.16}$$

where $\Delta\lambda_D$ is the observed line width, λ is the diagnostic wavelength at rest, T is the ion temperature, m is the mass of the ion and ξ is a non-thermal turbulent velocity. Using observations of emissions from ions/atoms of different mass, e.g., Hα and Ca II, and applying formula (1.16), Park et al. (2013) found temperatures between $4 \cdot 10^3$ and $2 \cdot 10^4$ K and non-thermal velocities (NTV) between 4 and 11 km s^{-1}. Using even more spectral lines, Parenti and Vial (2007) derived NTV inside a prominence at different temperatures. The temperature was considered to be the LTE emission temperature of the observed line. They covered the range between 10^4 and $2.5 \cdot 10^6$ K. The analysis was performed for a quiet-Sun region (considered as reference region) and two different locations of a quiescent prominence. From their analysis, Parenti and Vial (2007) found that in the quiet region the turbulent motions are increasing with temperature and reach a peak in the transition region at $T = 6 \cdot 10^5$ K. They decrease at larger altitudes and coronal temperatures. The prominence velocities were found to be lower than those found in quiet-Sun regions for $T = 6 \cdot 10^5$ K. There was also a difference in between the two locations of the prominence studied. While at one location, the plasma showed an increase of turbulence motion between $3 \cdot 10^4$ K $< T < 2 \cdot 10^5$ K, the velocity remained almost unchanged in the other region.

Using the observations from Parenti and Vial (2007), Anzer and Heinzel (2008) derived the PCTR temperature of the prominence along a 1D profile through the prominence. Assumptions of their model are a constant electron pressure in the entire system and the minimum temperature of $2.3 \cdot 10^4$ K in the center of the prominence. A fit of the theoretically calculated DEM with the observed one yields a width of only $1.9 \cdot 10^4$ km for the prominence along LOS.

The electron densities vary along the prominence and between different types of prominences. Most of the prominence densities observations revealed values between 10^9 and 10^{11} cm^{-3} (Labrosse et al. 2010).

Using the line-ratio technique, Parenti and Vial (2007) derived densities at two different locations on a quiescent prominence of the order of $6 \cdot 10^8$ - $3.6 \cdot 10^9$ cm^{-3}.

Observations show that the plasma which forms a prominence is very dynamic. It is continuously entering and exiting the filament on a time scale shorter than the filament life time (Martin 1998). Flow velocities normal to the LOS in a prominence have been derived by tracking plasma irregularities. The line-of-sight (LOS) velocity can be obtained through Doppler shift measurements, which has the disadvantage that the bulk spectral shift is proportional to some average of all velocities along the LOS. Labrosse et al. (2010) reports of observations by the tracking method of counter-streaming flows of about 5 - 20 km s^{-1}. From the Doppler shift method, values of ± 15 km s^{-1} have been obtained. Analyzing Hα time-sequence images, Chae et al. (2008) observed horizontal flows in a prominence at a speed of 10 km s^{-1} which after a few minutes became vertical flows with a velocity of 35 km s^{-1}.

1.5.2.3 Models

There are many models which are trying to explain the formation and evolution of the prominences. Some models assume that filaments are supported by a nearly force-free flux rope which stretches horizontally above the PIL. One of the early models has been described by Kuperus and Raadu (1974). Their model is essentially two-dimensional with a magnetic field arcade bridging the PIL. At elevated altitudes, the arcade field ends in an x-point which suspends a plasmoid above. The plasmoid is again surrounded by a magnetic arcade which prevents the plasmoid to lift (bootstrap field). The filament plasma is thought to reside in the upwardly bent pockets of the plasmoid magnetic field such that it cannot sink down to the surface. The system consist of three magnetically well separated regions: a low density zone of the bootstrap arcade field in the corona, a high density plasmoid above the x-point and a low density arcade below the x-point. In the plasmoid region the magnetic field is closed and in the 2D model of Kuperus and Raadu unconnected to the photosphere while above and below the filament, the magnetic field is closed and connected at the photosphere. The field is basically force-free except for the vicinity x-point.

van Ballegooijen and Martens (1989) have demonstrated how the Kuperus-Raadu configuration can be obtained through surface motion combined with steady reconnection at the x-point above the neutral line. The surface motion is a combination of shear along the neutral line and convergence towards the neutral line to achieve the required reconnection rate. The consequence is the formation of a helical flux tube which is able to support the prominence. This process is illustrated in Fig. 1.15.

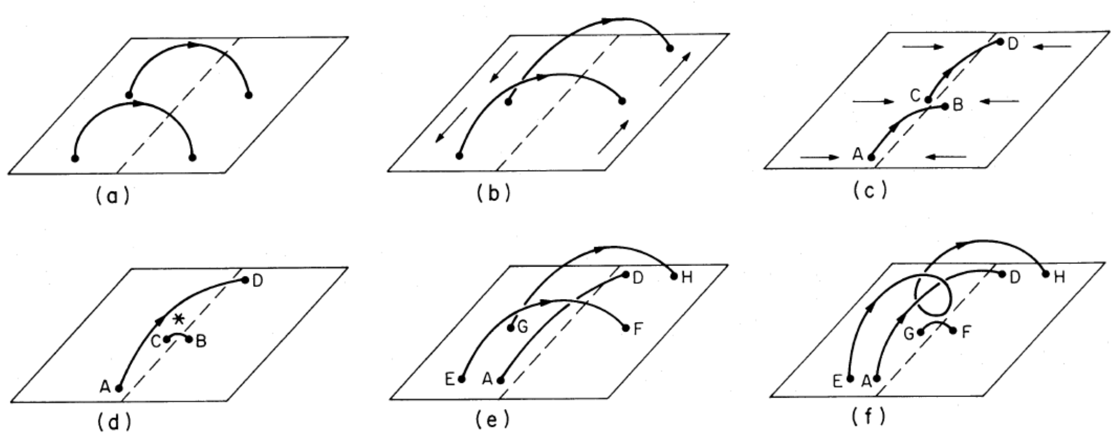

Figure 1.15: Schematic of flux cancellation in a sheared magnetic field taken from (van Ballegooijen and Martens 1989). The rectangle represents part of the photospheric plane. The dash line represents the PIL. (a) Initial potential field; (b) sheared magnetic field produced by flows along the neutral line; (c) the magnetic shear is increased further due to flows toward the neutral line; (d) reconnection produces long loop AD and a shorter loop CB which subsequently submerges; (e) overlying loops EF and GH are pushed to the neutral line; (f) reconnection produces the helical loop EH and a shorter loop GF which again submerges (van Ballegooijen and Martens 1989).

The initial magnetic field has a simple unsheared arcade configuration and is located normal to the PIL (see Fig. 1.15 a). By applying a foot point shear across the PIL the necessary field component along PIL is generated. An additional converging motion toward the PIL then leads to reconnection and the formation of a closed helical flux tube detached from the surface (see Fig. 1.15 b). The shear motions near quiescent prominences are considered to be due to the differential rotation. The newly created small loop below the flux tube may eventually submerge because its strong curvature and converging foot points which will give rise to a downward magnetic tension. van Ballegooijen and Martens (1989) proposed that by siphon flow cool plasma is transported along the helical fields and forms the prominence. Increasing shear will enhance the magnetic pressure due to an increased field component along the PIL, which causes the entire arcade system to flare. Sudden eruptions can only be modeled by a three-dimensional system (Mikić and Lee 2006).

1.5.3 Coronal Mass Ejections (CMEs)

1.5.3.1 Introduction

Probably the first observation of a coronal mass ejection was recorded in 1860 by G. Tempel during a total solar eclipse. Even if the method of recording was a simple drawing, Eddy (1974) concluded that the pictures show a major coronal transient. In 1975, Hildner et al. (1975) were the first who used the term "coronal mass ejection". A CME is a sudden release of plasma which caries a frozen-in magnetic flux and which propagates and expands from the Sun into the interplanetary space (Aschwanden 2004).

A typical CMEs has a three-parts structure which comprises a leading edge (LE), a dark cavity and a bright core (Illing and Hundhausen 1986). An example of a typical coronagraph observation is shown in Fig. 1.16.

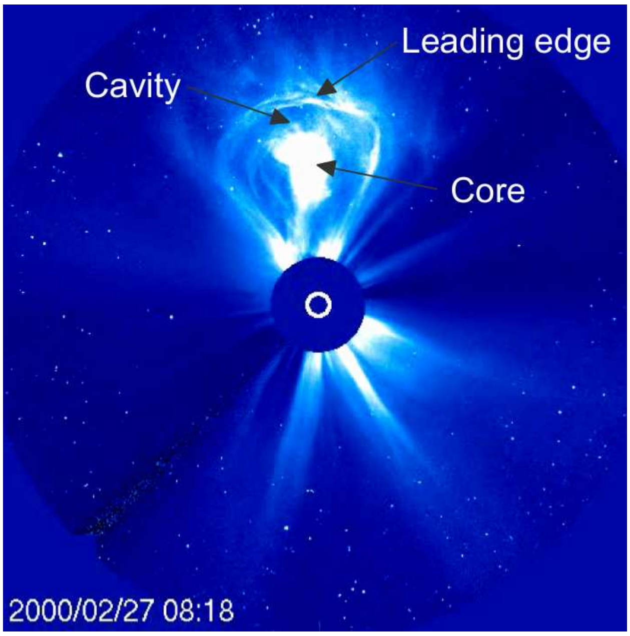

Figure 1.16: A typical three-parts structure of a CME. Figure adapted from http://sohowww.nascom.nasa.gov.

The bright core

The core is usually associated with plasma material expelled from the active region flares or prominence eruptions. The cool prominence plasma is then often swept away with the CME and forms an amorphous high-density core more or less at the center of the CME cloud.

The dark cavity

This part has a circular or semi-circular shape surrounding the bright core. The cavity is often interpreted as an expanding helical flux tube, which has its extremities connected to the solar surface.

The leading edge

There are alternative explanations given in the literature for the leading edge of a CME. One of them considers the leading edge being shaped by the background coronal magnetic field lines filled with plasmas which piled up by a shock or compression wave at the forefront of the CME. Another interpretation is that the overlying arcades of the erupting flux rope are stretched resulting in a compression of the coronal plasma on the outer side of the field line, thus producing a local density enhancement (Chen 2011).

The source site of CMEs are regions with closed magnetic field where free magnetic energy has been accumulated and is released during an eruption. It is therefore not surprising that the occurrence of CMEs is strongly correlated with the number of sunspots (Gopalswamy 2010) and with the solar magnetic activity. Often, they are also associated with the sources of flares in active regions. The CME-flare relation is however not a one-to-one relation and several studies have shown that sometimes flares are produced well before or after a CME. Also, some CMEs are not associated with a flare at all. The statistical correlation between sunspot numbers, flares and CMEs is displayed in Fig. 1.17.

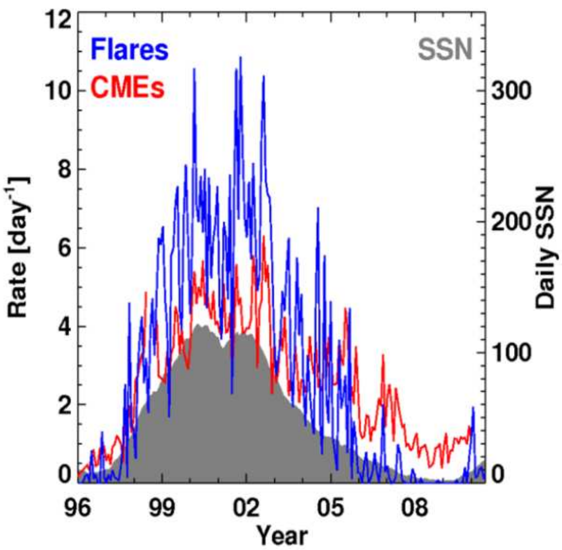

Figure 1.17: Daily CME and soft X -ray flare rates compared with daily sunspot number taken from Gopalswamy (2010).

During the minimum activity of the Sun, CME sources are distributed over all latitudes. As the activity of the Sun increases, one can observe a preference of CME occurrence at equatorial latitudes (Webb and Howard 2012).

CMEs are visible in optical wavelengths by Thomson scattering of the sunlight at the free electrons of the plasma cloud. Since the scattering cross section is small, the intensity of the scattered light is several orders of magnitude below the direct sunlight. Carefully designed instruments are required to limit the internal scatter of the direct sunlight of the instrument so that CME clouds becomes visible.
Since the Thomson scattering cross section per volume is proportional to the electron density, the intensity of the scattered light allows to estimate the CME mass. Vourlidas et al. (2010) calculated the density, mass and kinetic energy of several thousand CMEs during Solar cycle 23 (from 1996 to 2009) using data from the SOHO/LASCO instrument. The values for the CME mass spans between $\approx 10^9$ kg and $\approx 10^{13}$ kg, the average electron column density varies between $\approx 10^{13}$ cm^{-2} and $\approx 10^{16}$ cm^{-2} and for the energy between 10^{19} J and 10^{25} J.
The speed of CMEs just after launch varies from about some 10 km s^{-1} to very rapid CMEs with 3000 km s^{-1} (Gopalswamy 2010, Webb and Howard 2012). The speed listed in CME catalogs and calculated by some authors is often the speed of the CME projected on the plane of sky (POS) [5] which underestimates the real 3D speed. It was observed that during minimum solar activity, slow CMEs tend to be accelerated in the interplanetary medium to 400 km s^{-1}, the speed of the ambient solar wind. In contrast, at maximum solar activity, CMEs often start at high initial velocities and then tend to be decelerated. This is probably a consequence of an interaction with the solar wind (SW). It is well known that SW velocities vary with the solar cycle. At minimum solar activity, we have a distinct slow SW of around 400 km s^{-1} in the solar equatorial plane embedded in a dilute fast SW of about 700 km s^{-1} at higher latitudes. The slow solar wind plane coincides with the interplanetary current sheet. At higher solar activity, the current sheet warps so that slow and fast SW is found at almost all latitudes. When a CME is released into interplanetary space it encounters a drag force from the ambient solar wind which depends on velocity difference so that the CME velocity approaches the SW speed (Cargill 2004).

1.5.3.2 Observations

A strong development in CME observations started with the launch of dedicated spacecraft missions. The first undebated evidence of a CME was obtained in 1971 by coronagraph observations on board OSO-7 (Orbiting Solar Observatory) (Webb and Howard 2012). Many other missions like Skylab, P78-1, SMM (Solar Maximum Mission) followed with a continuous improvement of the space and time resolution of observations, (see Webb and Howard 2012, and references therein). In 1996 a new mission was launched, SOHO (Solar and Heliospheric Observatory) with the concentric LASCO (Large Angle and Spectrometric Coronagraphs) C1, C2 and C3 instruments (Brueckner et al. 1995). Since 1998 only the C2 and C3 coronagraphs have been operating and have covered the solar corona from 2.2 to 32 $R_\odot$. Another set of coronagraphs presently recording the solar corona in white-light are on board the STEREO (Solar Terrestrial Relations Observatory) spacecraft. The STEREO instrument suite comprises the concentric coronagraphs COR1 and COR2 and the off-axes heliospheric imagers HI1 and HI2 (Howard et al. 2008a). These four instruments cover a field of view from 1.4 to 330 $R_\odot$. Fig. 1.18 displays a se-

[5] The plane of sky (POS) is the plane perpendicular to the optical axis of a telescope as seen in a recorded image.

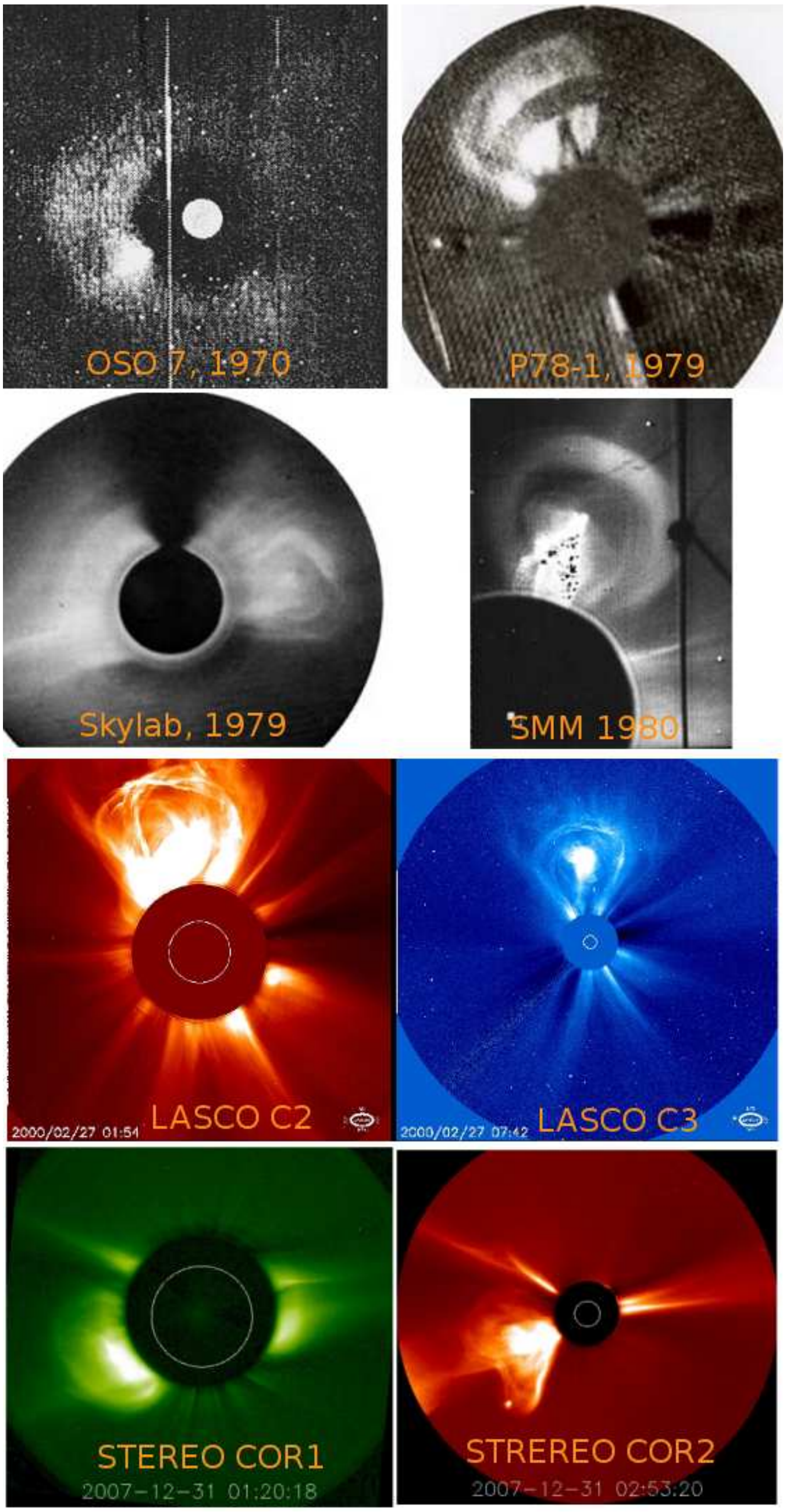

Figure 1.18: A series of historical CMEs observations recorded with different coronagraphs during recent decades illustrating the progress in coronagraph instrument taken from Schwenn et al. (2006).

ries of historical and recently observed images of solar coronal mass ejections. The series clearly demonstrates the progress made over the years in resolving the fine structure of CME clouds.

Data from ground-based coronagraphs can be used complementary to the space-based observations. For example, the coronagraph MK4 of Mauna Loa Solar Observatory (MLSO) takes polarized brightness images of the solar corona every 3 minutes but it can observe only during day time and with clear sky. The MLSO coronagraph has a field of view from 1.12 to 2.9 $R_{\odot}$. It is the only coronagraph which can observe the corona as close to the solar surface as 1.12 $R_{\odot}$.

Chen (2011) classifies the CMEs in two categories, “narrow” and “normal” and identifies for each of them a certain source mechanism. He define narrow CMEs as those with an angular width (AW) of 10 degrees and less and with an elongated jet-like shape. They are mostly observed to be launched in coronal holes where the magnetic field is open. He proposed that the CMEs are caused by reconnection of coronal loops which migrate or emerge into the coronal holes. In contrast, normal CMEs are considered to be produced by flux-rope eruptions which produce the common three part structure (see Fig. 1.16).

The CMEs which propagate along the Sun-observer line, either toward or away the observer are called halo CMEs. A halo CMEs may produce a geomagnetic storm if two conditions are fulfilled: the CME reaches Earth and its magnetic field has a southward component (Gopalswamy et al. 2007) facilitating in this way the reconnection [6] with the dawn side of the Earth’s magnetic field.

Another important parameter is the dawn to dusk electric field which depends on the solar wind velocity and the southward component of the CME magnetic field (Gonzalez et al. 1994). As a result of the reconnection, the CME particles enter into the magnetosphere and increase the total particle energy of the ring current [7]. The perturbations in the ring current which surrounds the Earth will lead to the geomagnetic storm perturbations on the Earth’s surface (Bothmer and Daglis 2007).

Besides coronagraphs, the recording of the solar radio emission is also used to detect CMEs. According to Gary and Keller (2004), the radio emission of CMEs is due to thermal free-free emission, plasma emission and gyro-emission. The observations of thermal free-free emission (bremsstrahlung induced by scattering of electrons at ions) in radio wavelengths gives information about the temperature and the electron density in the CME cloud. The imaging of CME radio emission at different wavelengths reveals the three part structure of a CME (leading edge, cavity and core) also seen in white light (Bastian and Gary 1997). The observations of CMEs in radio frequencies can be obtained from space-based and ground-based observatories. Radio observations have the advantage that a CME can be monitored right from the time it is launched on the solar disk while it is still hidden behind the occulter in white light observations (Bastian and Gary 1997). Other advantages according to Bastian and Gary (1997) are that radio observations are sensitive to a broad range of temperatures and are sensitive to emission from non-thermal electrons.

[6]Magnetic reconnection can be defined as change in the topology of the magnetic field lines (Schrijver and Siscoe 2009).

[7]The ring current is an electric current flow of a torus shape around Earth in the equatorial plane (Daglis 1999).

1.5.3.3 CME models

The huge plasma cloud of a CME, at some distance from the Sun may reach a size which even exceeds the Sun. The processes relevant for structuring a CME on much less visible scales of a few 1000 km are still the object of speculations. The number of source models has grown with the number and resolution of CME observations but also because a physical idea for the source process was required for the growing number of attempts to numerically simulate CME eruptions. The goals of these simulations was to identify a source mechanism from the acceleration or the shape of the post-eruption CME cloud.

- **Flux cancellation model**

  The concept of flux cancellation was initially introduced to explain the formation of a flux rope and of the prominences (Amari et al. 2010). Based on magnetograms and Hα observations, Martin et al. (1985) defined flux cancellation as the mutual disappearance of different polarity flux at the inversion line.
  As mentioned in Section 1.5.2.2, in numerical studies of a series of force-free equilibria, van Ballegooijen and Martens (1989) found that flux cancellation at the neutral line together with a strong shear of the coronal magnetic field above will give rise to the formation of a flux rope (FR). These FRs can support prominence material as a result of the helical configuration of their magnetic field. If magnetic flux is continuously convected to the neutral line and disappears (see Fig. 1.15) the prominences will rise when this configuration eventually loses equilibrium.
  Linker et al. (2003) have simulated an MHD model of the entire process from the initiation of a CME to its propagation through interplanetary space. They start with a spherically symmetric solar pre-eruption configuration consisting of a helmet streamer surrounded by a solar wind on open field lines (see Fig. 1.19a).

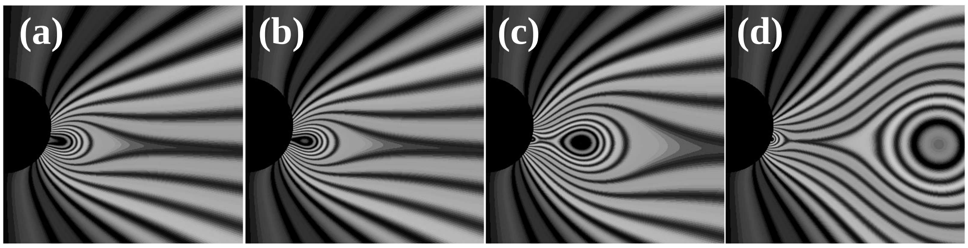

Figure 1.19: MHD simulation of a helmet streamer eruption triggered by flux cancellation taken from Linker et al. (2003). The stripes shows projected field lines at subsequent stages of the eruption simulation.

  In order to trigger a CME, they apply a shear flow at the surface along the inversion line which enhances the magnetic energy of the streamer. Just like in the van Ballegooijen and Martens (1989) model, Linker et al. (2003) applied a surface flow component toward the inversion line to mimic the flux cancellation. A flux rope builds up as a consequence of the continuous flux cancellation which enhance the magnetic pressure in its interior.
  During the erupting phase a current sheet was observed to form at coronal heights

below the flux rope (see Fig. 1.19c) and a certain percentage of the magnetic energy is transformed in kinetic energy allowing the plasma in the flux-rope to move outward into the SW as a CME. From the analysis of the time evolution of the system, Linker et al. (2003) could see how fast the streamer becomes unstable in dependence of the strength of the surface motion.
Linker et al. (2003) extended the calculations in order to investigate the subsequent propagation of the CME to 1 A.U.. They could reproduce the formation of a shock wave in front of the CME.

- **Breakout model**

  This model by Antiochos et al. (1999) assumes a preexisting axisymmetric quadrupolar potential field with three neutral lines in the photosphere. The configuration is shown in Fig. 1.20a.

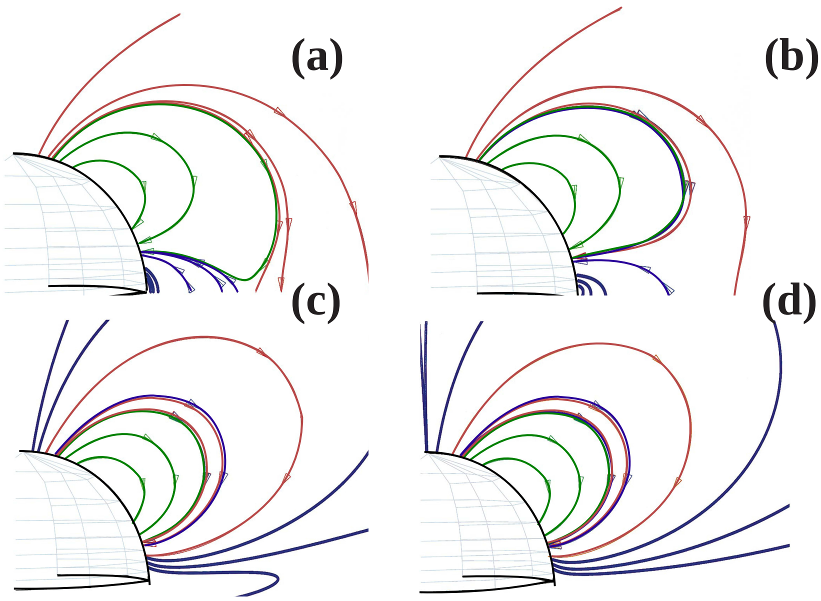

Figure 1.20: Field lines at different stages of the breakout model taken from Antiochos et al. (1999). The field is symmetric about the axis of rotation and the equator, so only one quadrant is shown. The photospheric boundary surface is indicated by the light gray grid. Magnetic field lines are colored (red, green, or blue) according to their flux topology. The two types of blue field lines indicate unsheared field (light blue) and low-lying (dark blue) field that is sheared later in the simulation. (a) Initial potential magnetic field. (b) Force-free field after a shear of n/8. The field lines shown correspond to those in (a) and are traced from the same footpoint position on the photosphere as in (a). (c) As above, but for a shear of $3\pi/8$. (d) As above, but for a shear of $\pi/2$. Figures adapted from Antiochos et al. (1999).

It has a central arcade (blue) at the equator and two more arcades at higher latitudes symmetrical to the equator (green field lines). There is also a bootstrapping polar flux overlying the entire three arcade structures (the red lines in Fig. 1.20) (Antiochos et al. 1999). In order to determine the energy of the system required to drive a CME, Antiochos et al. (1999) simulated the excitation process by two different methods. One is by calculating a sequence of force-free equilibria adapted to an increasing shear of the photosphere near the equator. The second method uses an ideal 2.5D MHD code with identical initial and boundary conditions as the first method.

The force-free field code calculates iteratively the minimum energy state for each given value of the surface shear. As the shear increases, the minimum energy field configurations shows an increasing amount of flux from the inner arcade to reconnect with the outer bootstrapping flux until the latter is entirely used up and allows the equatorial arcade flux to break through into the interplanetary space. In the

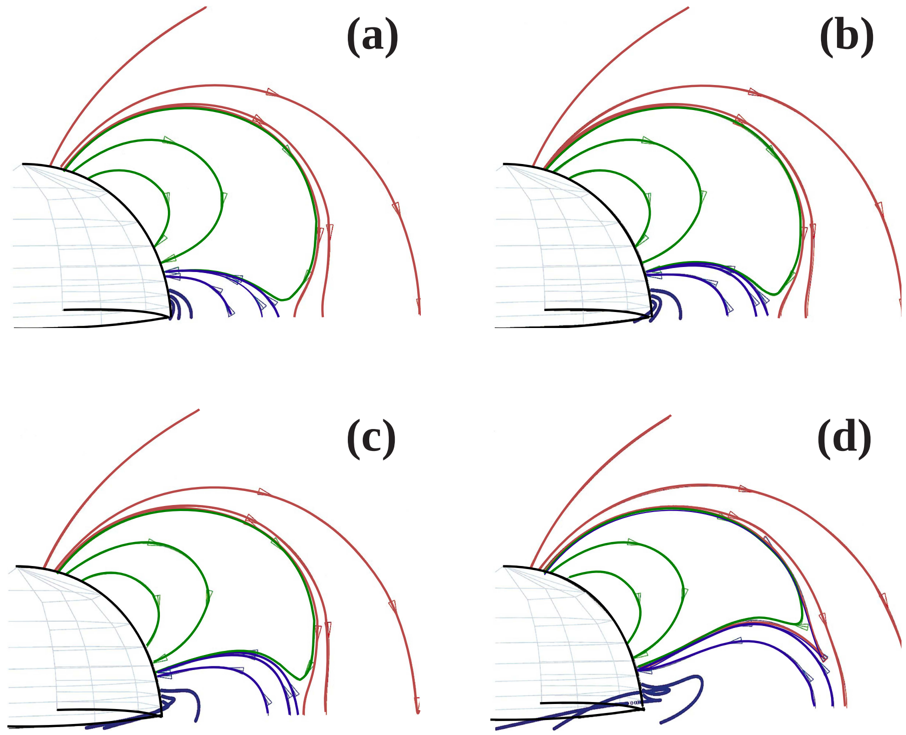

Figure 1.21: MHD solution after a shear of (a) $\pi/8$, (b) $\pi/4$, (c) $3\pi/8$, and (d) $\pi/2$. The field lines shown are the same as those in Fig. 1.20. Figures adapted from Antiochos et al. (1999).

ideal MHD calculations the plasma is kept in hydrostatic equilibrium with a given temperature and density. The values of plasma beta in their computational box are below unity near the bottom boundary, but much higher than unity near the null point at the top of the equatorial arcade. As photospheric boundary condition a slow continuous shear motion was applied with latitudinal profile as in the previous experiment. The MHD solution for each shear phase are shown in Fig. 1.21 a,b,c,d. Since in ideal MHD reconnection cannot occur, the shearing of the innermost ar-

cades just enhances their magnetic pressure and makes them grow in size pushing the bootstrapping field upwards. The interface between the opposing flux system evolves from a null point to a single extended current sheet.
According to observations, CMEs are more common at the site with multiple flux systems which supports the breakout model. Some CMEs triggered by prominence eruptions could be well explained by this model (see Forbes et al. 2006, and references therein). Lynch et al. (2005) performed a 3D MHD simulation of the breakout process. As initial magnetic field they consider an elongated bipolar active region embedded in a background dipole field (see Fig. 1.22 - upper left).

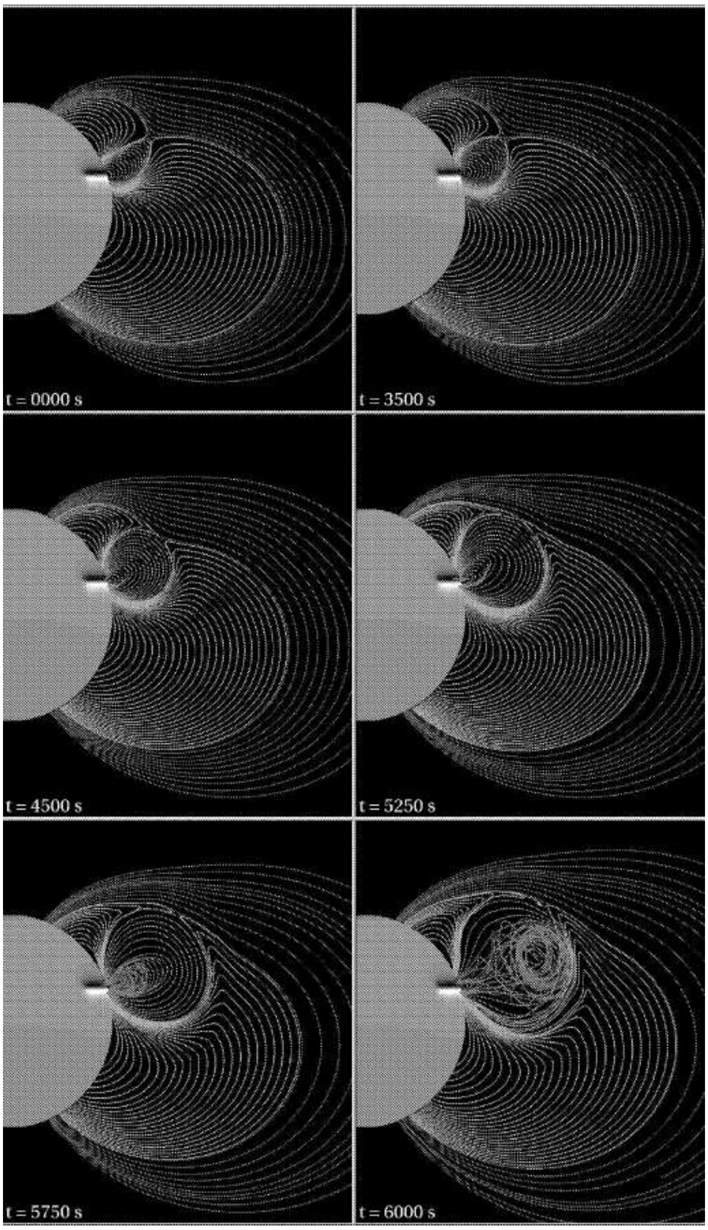

Figure 1.22: Time evolution of the breakout model with field lines from a meridional plane. Figure taken from Lynch et al. (2005).

Using resistive MHD, they allow the sheared inner flux and the overlying restraining flux to reconnect. The plasma parameters are considered spherically symmetric. The initial plasma beta is less than one in the entire computational domain. The shear motion applied has no horizontal divergence so that the normal component of the magnetic field at the surface remains constant during simulation (Lynch et al. 2005). As a result of the imposed shear, the magnetic pressure increases above the neutral line and pushes up the arcade field lines. Consequently, the null point is distorted into a thin current sheet (see Fig. 1.22 - middle right). The model allows magnetic reconnection at the moment when the null point current sheet is compressed to the scale of the numerical grid. As a result of reconnection, the expansion of the flux rope increases rapidly until the flux rope finally erupts.

- **Emerging flux model**

  From active region observations it was found that the emergence of new magnetic flux was well correlated with the occurrence of flares and CMEs (Mikić and Lee 2006).
  The emerging flux as a trigger mechanism for CMEs was proposed by Chen and Shibata (2000). The basic idea of this model is that the reconfiguration of the magnetic field topology as a consequence of the emerging flux may cause the initiation of a CME. The authors tested their model with a 2D resistive MHD simulation. The initial setup consist of a flux rope which supports the prominence material. The flux rope is embedded in a 2D arcade. The emerging flux has opposite polarity to the overlying arcade field and breaks through the photosphere either at the neutral line or asymmetrically in one of the two polarity regions. In the model, the contribution of gravity force is neglected, the temperature is considered uniform and the resistivity depends on the local current density. The configurations of the two cases are sketched in Fig. 1.23. If the flux emergence occurs symmetrically inside the

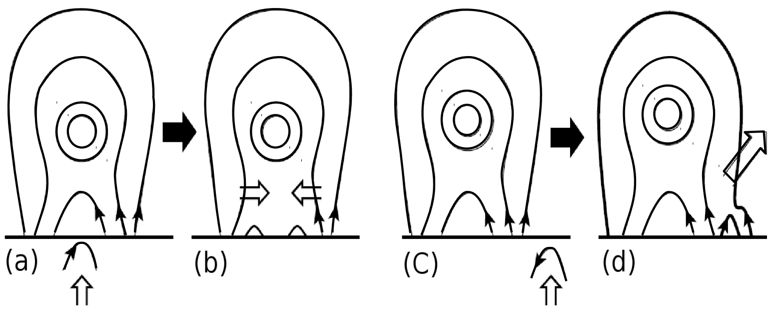

Figure 1.23: Diagram of two configurations of CME triggering by emerging flux adapted from Chen (2011). (a,b) Emerging flux inside the filament channel cancels the pre-existing loops, which results in the in situ decrease of the magnetic pressure. Lateral magnetized plasmas are driven convergent to form a current sheet; (c,d) Emerging flux outside the filament channel reconnects with the large coronal loop, which results in the expansion of the loop. The underlying flux rope then rises and a current sheet forms near the magnetic null point Chen (2011).

filament channel (see Fig. 1.23a) it reconnects with the arcade field below the flux rope as shown in Fig. 1.23a. The consequence of this small scale reconnection will be a diffusion zone of magnetic pressure below the flux rope along with the formation of a current sheet and inward motion of the plasma (arrows in Fig. 1.23b) into the diffusion zone. The flux rope eventually moves upward and finally produces the CME ejection. In a second setup, Chen (2011) consider the flux emerging asymmetrically on one side of the neutral line. It reconnects with the overlying field as shown in Fig. 1.23c. The reconnection now occurs at one flank of the arcade. The simulations show that this process sufficiently destabilizes the system so that again the flux rope is rapidly ejected.
Leake et al. (2014) developed an alternative 3D MHD model of a flux emergence event. In their model, a twisted flux rope rises from below the surface and encounters a dipole-arcade field above. In order to catch details of the emergence process properly, the model includes the convection zone, the photosphere/chromosphere and the corona as separately simulated layers. In three different simulations with the same initial field geometry they vary the strength of the coronal preexisting arcade field. Fig. 1.24 shows the evolution of the emerging flux rope towards eruption.

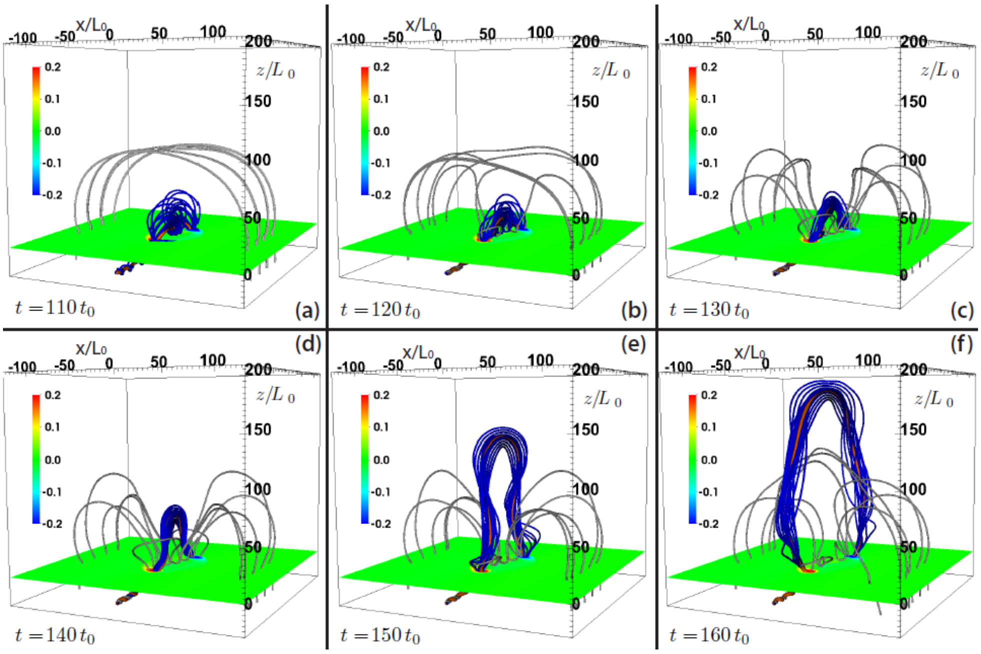

Figure 1.24: Simulation of an eruption of a coronal flux rope taken from Leake et al. (2014). The horizontal slice shows the vertical magnetic field at the surface. The gray lines originate on the bottom boundary and represent the field of the initial dipole configuration. The blue lines are part of the emerging flux rope (Leake et al. 2014).

The flux tube rises from the convection zone to the surface and partly reconnects with the overlying arcades. Initially, the reconnection does not influence the emergence of the flux tube. As the flux tube continues to emerge further into the corona, the flux of the overlying arcade is partially canceled by the continuous reconnection with the emerging field. As the reconnection between the bootstrap flux and the rising flux tube continues, the acceleration of the flux rope increases. The flux rope however in the simulation rises only until it reaches the upper boundary of the computational box (see Fig. 1.24) due to inadequate boundary conditions. Leake et al. (2014) assumes that in a more realistic scenario the flux rope will erupt and evolve into a CME.

2 3D reconstruction in the solar corona

In this Chapter, we will present and apply two main methods used for the 3D reconstruction of solar phenomena. One method is called Multi-view B-spline Stereoscopic Reconstruction (MBSR) which for the 3D reconstruction uses the principle of stereoscopy. This method was developed initially for two views by Bernd Inhester. We have extended and applied the method for three view reconstructions. Stereoscopy is a method based on geometry which uses images taken from different view directions. It is widely used for the reconstruction of coronal loops, prominences and different parts of coronal mass ejections. An application of the MBSR is presented in Chapter 4. The second method which can be used for the 3D reconstruction of coronal loops is the non-linear force-free field (NLFFF) extrapolation method. We have extended and tested this method in order to be able to find a good agreement between the modeled and observed magnetic field. The extended field extrapolation method is called S-NLFFF and is presented in Section 2.5. The tests of the new method are presented in Chapter 5.

2.1 Introduction

The measurement of magnetic field in the corona is not an easy task. We discuss here only two methods to indirectly determine the coronal magnetic field.

A method which yields a quantitative estimate of the coronal field is the extrapolation from solar surface field observations. It is based on the assumption of a force-free coronal field and requires a nonlinear boundary value problem to be solved.

The second method to constrain the coronal field is the stereoscopic reconstruction of EUV loops which are assumed to be aligned with the coronal field. The 3D reconstruction of these loops mainly constrains the geometry of the coronal field. The method is somewhat restricted to the vicinity of active regions where the EUV loops are mostly observed. Yet, this is valuable information because active regions supply most of the coronal magnetic flux through the solar surface.

Each of the two approaches have their limitations. EUV loop stereoscopy does not yield the magnetic field strength but only the shape of some, often few, individual field lines. However, it provides observational constraints for the magnetic field at altitudes well above the photospheric surface and therefore could well serve to stabilize the extrapolation at these altitudes. The three-dimensional stereoscopic reconstruction is prone to some typical errors, basically of geometrical origin when the view angle between the two stereo projections is small and where the loop tangent tends to become orthogonal to the epipolar plane normal. The epipolar planes define the local reconstruction geometry (Inhester 2006, Aschwanden 2011).

One of the shortcomings of the NLFFF method is the fact that the boundary conditions for the extrapolation are often incomplete and contaminated with errors (see Section 2.4). As a result, there is an obvious misalignment between the extrapolated and observed field lines. In a study which compared the results from extrapolation with observations, a typical discrepancy between the orientation of reconstructed flux tubes and extrapolated field lines was found to be about 20 degrees (De Rosa et al. 2009). Because of these discrepancies between models and observations, we propose and test a coronal field reconstruction method which combines the conventional NLFFF extrapolation with 3D data from individual loops as they can be obtained from stereoscopic reconstruction. In Section 2.5.1 of this chapter we describe our approach and in Chapter 5, the new method is tested using boundary values and simulated loops from a known force-free field.

2.2 Stereoscopy

2.2.1 Introduction

Stereoscopic reconstruction is used in many fields like engineering, medicine, cinematography, etc., and the level of difficulty can differ according to the object which has to be reconstructed. A stereoscopic reconstruction needs observations from at least two view directions. The reconstruction can be performed for point-like, curve-like and surface-like objects. The reconstruction of polygonal surfaces is typically reduced to the reconstruction of the edges and corners. This is not possible for curved surfaces. An example of difficult surfaces to be reconstructed are human faces where one needs more information from the images like texture, colors and the direction of light sources.

In solar physics if two simultaneous viewpoints are not available, one can make use of the solar rotation to perform stereoscopic reconstruction. The reconstruction can be achieved from a pair of images from the same view point but at different times ($t_1,\ t_2$). The separation in time has to be short enough so that intrinsic time variations of the reconstructed object can be neglected. This method is called rotation stereoscopy. Prominences being a rather stable structure which can sometimes last for months (Kuperus and Tandberg-Hanssen 1967) are a suitable phenomenon for rotational stereoscopy. This does not apply to its small scale structures. Coronal loops, on the other hand, have a much shorter life time, from hours to days (Lenz 1999), which restricts severely the time between the two images used for the reconstruction.

With the launch of the STEREO spacecraft, stereoscopic reconstruction started to be highly used for solar phenomena. Usually it was performed from the two view directions provided by the telescopes onboard STEREO. As the angle between the spacecraft increased, stereoscopic reconstructions could be performed from three view directions, where the third view was supplied by other spacecraft, e.g., SOHO or SDO.

In the ideal case, from a projected pair of curve-like objects from the Sun (e.g. coronal loops or the outer edge of prominences) we can obtain a unique 3D curve as a result of the intersection of their backward projection on the Sun (Inhester 2006). Two-view directions are sufficient for a 3D reconstruction from an ideal data set. The use of more than two views brings more accuracy to the reconstruction if the data are noisy.

The leading edge projection of a CME in the images is used for the reconstruction of the CME surface. Their reconstruction, however, yields a curve which is not necessarily located on the true 3D surface because in the images the projection of different locations of the 3D surface (Inhester 2006) is recorded (see detailed explanations in Chapter 4, Section 4.2.5). Here, if more views are available, the reconstruction lies closer to the real 3D object.

The three main steps for stereoscopic reconstruction are identification, matching and reconstruction. The basis for all stereoscopic reconstructions is the epipolar geometry (Inhester 2006).

2.2.2 The epipolar geometry

The epipolar geometry defines the geometry of stereoscopic reconstruction. It is independent of the object to be reconstructed, but depends on the intrinsic parameters of the recording instruments (Hartley and Zisserman 2003). Using the epipolar geometry, the reconstruction can be reduced from a 3D problem to a set of 2D problems. The elements which define the epipolar geometry are (see Fig. 2.1) (Inhester 2006):

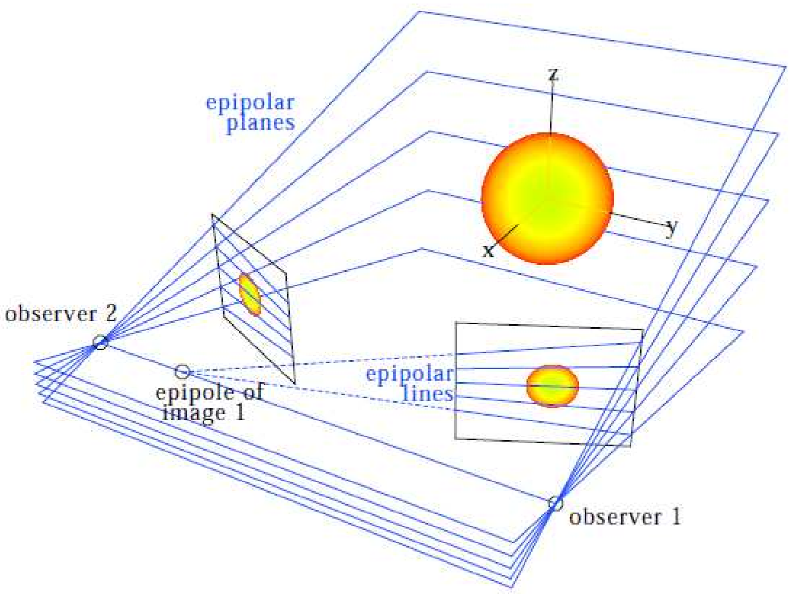

Figure 2.1: Orientation of epipolar planes in space and the respective epipolar lines in the images for two observers (e.g., space craft) looking at the Sun. Figure taken from Inhester (2006).

- **The stereo base line** is the line between the two observers
- **The stereo base angle** is the angle subtended by the two view directions
- **The stereo base plane** is the plane defined by the two observers and the Sun's center.

- **The epipolar plane** is the plane uniquely defined by a 3D object point to be reconstructed and the positions of the two observers. Different 3D object points to be reconstructed may lie on different epipolar planes but share the same stereo base line.

- **The epipolar lines** are the projections of the epipolar planes onto each of the observer images. For e.g., the ray $[O_1, M]$ through M_1 in image 1 lies on the epipolar plane described by $\pi = (O_1, O_2, M)$. Since ray $[O_2, M]$ lies on the plane π, the projection point M_2 in image 2 is found on the (*epi-line*[1] from *Im2* of Fig. 2.2) intersection line between the epipolar plane π and the plane of image 2 (Fig. 2.2).

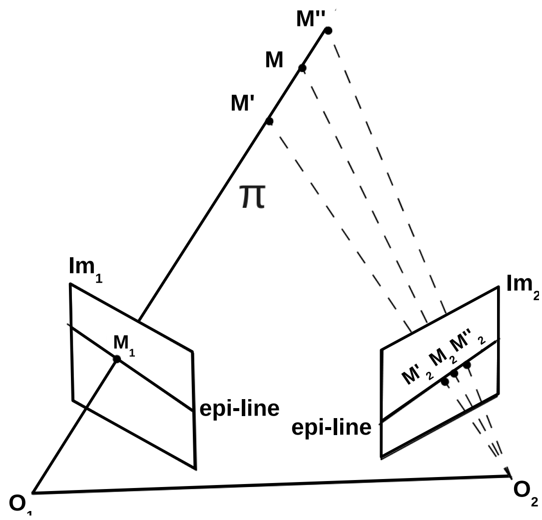

Figure 2.2: Sketch of the point correspondence on an epipolar line; A point M_1 from Im_1 back-projects to a ray in 3D space defined by the observer O_1 and M_1. This ray together with the line connecting observer O_1 with observer O_2 define the epipolar plane π. The projection of this epipolar plane on the image Im_2 will be imaged as a line (*epi-line*). The 3D point M which projects to M_1 must lie on this ray, so the image of M in the second view must lie on *epi-line* of Im_2.

The epipolar lines constrain the search of corresponding points in a stereo image pair to a search along a line and not on the entire image plane (Hartley and Zisserman 2003).

- **The epipole** of image 1, for e.g., is the intersection between the stereo base line and the prolongation of the epipolar lines from image 1.

The epipolar coordinate system is defined in the epipolar geometry in which all the transformations are performed in order to obtain the 3D location of the reconstructed object.

Identification and matching

After the object to be reconstructed was chosen, one has to correctly identify the projection of the 3D object in both images. For solar phenomena (loops, prominences,

[1]*epi-line* is the short-hand for epipolar line.

coronal mass ejections) which might be the object of a 3D reconstruction, one often has to process the images in order to find the correct correspondence. For example, a common image processing step is the background subtraction. Since we often observe optically thin lines in EUV and/or coronograph images, the image brightness measures the emissivity integrated along the line of sight. With the background subtraction, we remove some of the contributions from other sources than the one we want to reconstruct.

Two corresponding points from two images may not have exactly the same brightness. After the images were “cleaned” from background contributions and/or noise, an automatic way to find a match point in image 2 of a point from image 1, is to parse along the epipolar line in image 2 and to calculate the intensity difference between the point of image 1 and each point from the epipolar line of image 2. The corresponding point will be found when the intensity difference is a minimum. Another way to find a corresponding point is by visual inspection using the epipolar constraint. The process, in both cases, has to be reversible, i.e. it should be independent on weather we identify a point in image 1 first and search for it in image 2 or vice versa. The choice of the corresponding points from the images used for reconstruction is called tie-pointing.

2.2.3 Reconstruction

A 3D reconstruction requires a camera model which describes the camera optics. A simple camera model is sufficient for the long focal-lengths optics used in solar physics. In

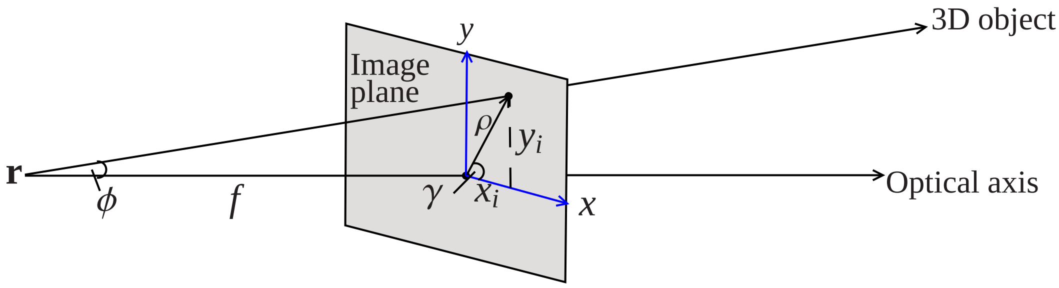

Figure 2.3: Sketch of a simple camera model.

Fig. 2.3 we present a simple camera model which relates the image coordinates $(x,\ y)$ of an object relative to the optical axis to angles ϕ and γ of the ray from the observer $\mathbf{r}$ to the object,

$$\tan\phi = \frac{\rho}{f} = \frac{\sqrt{x^2+y^2}}{f}\ , \tag{2.1}$$

$$\tan\gamma = \frac{y}{x}\ , \tag{2.2}$$

where f is the focal length of the instrument. Here, $x,\ y$ are expressed in the same units as the focal length. Hence a single image only gives us the direction angles $(\phi,\ \gamma)$, not the distance of the object. The distance ρ, the x coordinate and the y coordinate are dependent on the two orientation angles:

$$\rho = f \tan \phi \,, \tag{2.3}$$

$$x = \rho \cos \gamma \,, \tag{2.4}$$

$$y = \rho \sin \gamma \,. \tag{2.5}$$

We assume that the optical axis is directed to the Sun's center, the origin of our 3D coordinate system. The Sun's rotation axis $\hat{\mathbf{\Omega}}$ projects to the y axis of the image 2.4. This

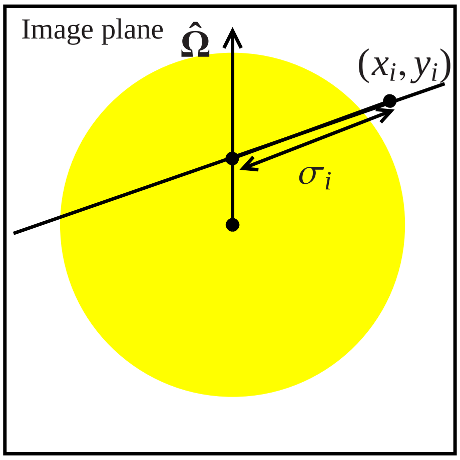

Figure 2.4: Sketch of the projection of the solar disk on the image plane, its rotation axis $\hat{\mathbf{\Omega}}$ and the epipolar plane. The distance σ_i is the distance of the object along the epipolar line (disparity).

orientation is chosen in most solar observations. We consider a 3D object point $\mathbf{\Delta r}$ which projects to the image coordinates (x, y). The unit vector to the observer is defined by

$$\hat{\mathbf{r}} = \frac{\mathbf{r}}{|\mathbf{r}|} \,. \tag{2.6}$$

The x axis on the image must be perpendicular to $\hat{\mathbf{\Omega}}$ and to $\mathbf{r}$

$$\hat{\mathbf{e}}_x = \frac{\hat{\mathbf{\Omega}} \times \mathbf{r}}{|\hat{\mathbf{\Omega}} \times \mathbf{r}|} \,. \tag{2.7}$$

The y axis on the image must be perpendicular to $\hat{\mathbf{e}}_x$ and $\mathbf{r}$

$$\hat{\mathbf{e}}_y = \hat{\mathbf{r}} \times \hat{\mathbf{e}}_x \,. \tag{2.8}$$

The angle ϕ between the optical axis and the ray to the object is

$$\tan \phi = \frac{|(1 - \hat{\mathbf{r}}\hat{\mathbf{r}}) \cdot \mathbf{\Delta r}|}{|\mathbf{r}| - \hat{\mathbf{r}} \cdot \mathbf{\Delta r}} = \frac{\sqrt{(\hat{\mathbf{e}}_x \mathbf{\Delta r})^2 + (\hat{\mathbf{e}}_y \mathbf{\Delta r})^2}}{|\mathbf{r}| - \hat{\mathbf{r}} \cdot \mathbf{\Delta r}} \tag{2.9}$$

and the angle γ,

$$\tan \gamma = \frac{\hat{\mathbf{e}}_\mathbf{y} \cdot \mathbf{\Delta r}}{\hat{\mathbf{e}}_\mathbf{x} \cdot \mathbf{\Delta r}} \,. \tag{2.10}$$

Here, all unit vectors $\hat{\mathbf{r}}$, $\hat{\mathbf{e}}_\mathbf{x}$, $\hat{\mathbf{e}}_\mathbf{y}$ are known from the telescope position. In order to simplify the problem, we can replace the projective geometry by the affine one. The affine geometry considers all the rays to be parallel and it can be used when the distances are very large compared to the focal length (like for the distance between the Sun and the STEREO telescopes). In Eq. (2.9) the denominator is then replaced by $|\mathbf{r}| - \hat{\mathbf{r}} \cdot \mathbf{\Delta r} \to |\mathbf{r}|$.

2.2.3.1 Stereo case

In general, for performing stereoscopic reconstructions from two vantage points the separation angle between the two view directions should deviate sufficiently from 0° or 180° so that the images contain independent information. Close to these limiting angles, it is often easy to identify corresponding features in both images. The more the viewing angle deviates from 0° or 180°, the identification of the same feature in both images starts to become more difficult. However, the geometrical errors of the reconstruction decrease and reaches a minimum when the stereo base angle approaches 90° (Inhester 2006).

Our task is to find $\mathbf{\Delta r}$ from the image coordinate pairs (x_1, y_1) and (x_2, y_2) of two images. The first step is to find the epipolar plane of the object. We label the planes by the distance z, which is the distance from the Sun's center to the intersection point between the epipolar plane and the solar rotational axis $\hat{\mathbf{\Omega}}$ (see Fig. 2.5).

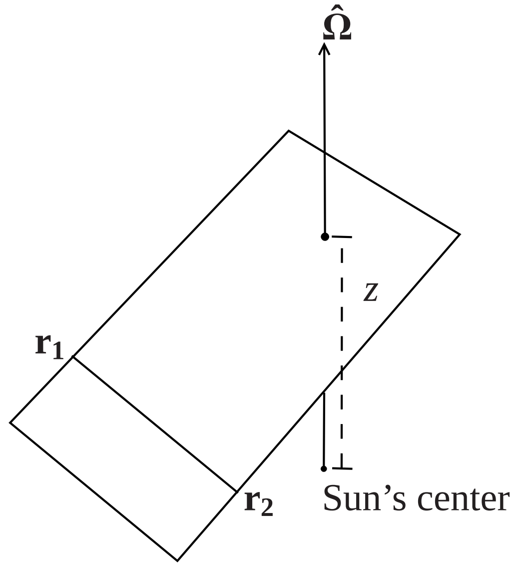

Figure 2.5: Sketch of the intersection between the epipolar plane and the solar rotation axis $\hat{\mathbf{\Omega}}$.

The epipolar plane (z) is defined by

$$(z) = \{\mathbf{x}|\mathbf{x} = z\hat{\mathbf{\Omega}} + \alpha_1(\mathbf{r}_1 - z\hat{\mathbf{\Omega}}) + \alpha_2(\mathbf{r}_2 - z\hat{\mathbf{\Omega}}); \alpha_1, \alpha_2 \in \mathbb{R}\} \; . \tag{2.11}$$

The normal vector to the epipolar plane is

$$\mathbf{n}(z) = (\mathbf{r}_1 - z\hat{\mathbf{\Omega}}) \times (\mathbf{r}_2 - z\hat{\mathbf{\Omega}}) \; . \tag{2.12}$$

Given the image coordinates (x_i, y_i) of an object in two images i=1, 2, we can find the label z of the respective epipolar plane by defining

$$\mathbf{d}_i \propto x_i \hat{\mathbf{e}}_{x_i} + y_i \hat{\mathbf{e}}_{y_i} - f \hat{\mathbf{r}}_i \tag{2.13}$$

as the ray of unknown length from the observer i to the object which has to lie in the epipolar plane.

$$
\begin{aligned}
0 &= \mathbf{d}_i \cdot \mathbf{n}(z) &(2.14)\\
&= \mathbf{d}_i \cdot (\mathbf{r}_1 - z\hat{\mathbf{\Omega}}) \times (\mathbf{r}_2 - z\hat{\mathbf{\Omega}})\\
&= \mathbf{d}_i \cdot [\mathbf{r}_1 \times \mathbf{r}_2 - z(\mathbf{r}_1 + \mathbf{r}_2) \times \hat{\mathbf{\Omega}}] \text{ or}\\
z &= \frac{\mathbf{d}_i \cdot \mathbf{r}_1 \times \mathbf{r}_2}{\mathbf{d}_i \cdot (\mathbf{r}_1 + \mathbf{r}_2) \times \hat{\mathbf{\Omega}}} &(2.15)
\end{aligned}
$$

Note that the length of $\mathbf{d}_i$ does not matter. If this formula does not give the same z for $\mathbf{d}_1$ and $\mathbf{d}_2$ then the image coordinates (x_1, y_1) and (x_2, y_2) do not correspond.

After we have determined the epipolar plane of the object at $\mathbf{\Delta r}$, the 3D reconstruction reduces to a 2D problem. The origin of our 2D coordinate system in the epipolar plane is at the intersection between the epipolar plane and the Sun's rotation axis, i.e. $z\hat{\mathbf{\Omega}}$. Rewriting Eq. (2.12) we get for $\mathbf{\Delta r}$ the following expression:

$$\mathbf{\Delta r} = \alpha_1 \tilde{\mathbf{r}}_1 + \alpha_2 \tilde{\mathbf{r}}_2 + z\hat{\mathbf{\Omega}} \,, \tag{2.16}$$

$$\tilde{\mathbf{r}}_i = \mathbf{r}_i - z\hat{\mathbf{\Omega}} \,, \tag{2.17}$$

where $\tilde{\mathbf{r}}_i$ is the observer's position in the epipolar plane.

From the decomposition of $\mathbf{\Delta r}$ (see Appendix for details) we obtain two equations for α_1 and α_2.

$$|\tilde{\mathbf{r}}_i| \frac{\sigma_i}{f'} = \left[\hat{\mathbf{e}}_\mathbf{i} + \frac{\sigma_i}{f'} \hat{\tilde{\mathbf{r}}}_\mathbf{i} (1 - \hat{\tilde{\mathbf{e}}}_\mathbf{i} \hat{\mathbf{e}}_\mathbf{i}) \right] (\alpha_1 \tilde{\mathbf{r}}_1 + \alpha_2 \tilde{\mathbf{r}}_2), \quad \text{i} = 1 \text{ and } 2 \tag{2.18}$$

which can be solved for α_1 and α_2. For positions close to the heliographic equator, $\tilde{\mathbf{r}}_\mathbf{i} \hat{\tilde{\mathbf{e}}}_\mathbf{i} \approx 0$ and the second and third term in the square brackets on the right hand side can be neglected if affine geometry is assumed. Then approximately

$$\alpha_i \sim \frac{|\tilde{\mathbf{r}}_\mathbf{i}|}{\tilde{\mathbf{r}}_\mathbf{i} \cdot \hat{\tilde{\mathbf{e}}}_\mathbf{i}} \frac{\sigma_i}{f'} \,. \tag{2.19}$$

2.2.3.2 Reconstruction errors

The instruments have finite resolution and therefore the image coordinates $(x,\ y)$ are also uncertain. This at first has an impact on the calculation of the epipolar plane parameter z in Eq. (2.15). For a typical arrangement of the STEREO spacecraft, both in the ecliptic plane at approximately the same distance r_{sc} from the Sun, we have:

$$\mathbf{r}_1 \times \mathbf{r}_2 \sim \hat{\mathbf{z}} r_{sc}^2 \sin\tilde{\delta} \,, \tag{2.20}$$

$$(\mathbf{r}_1 + \mathbf{r}_2) \times \hat{\mathbf{\Omega}} \sim 2 r_{sc} \cos(\tilde{\delta}/2) \hat{\mathbf{e}}_p \,, \tag{2.21}$$

where $\hat{\mathbf{e}}_p$ is normal to $(\mathbf{r}_1 + \mathbf{r}_2)$ and $\hat{\mathbf{z}}$ is the ecliptic normal direction. The spacecraft r_{sc} is positioned at approximately 1 A.U. from the Sun and $\tilde{\delta}$ is the angle between the spacecraft at the Sun center. Since $\hat{\mathbf{e}}_{\mathbf{y_i}} \sim \hat{\mathbf{z}} \parallel (\mathbf{r}_1 \times \mathbf{r}_2)$, we can simply derive the error in z from Eq. (2.15) assuming $d_i = -f\hat{\mathbf{r}}_i$ to lowest order, $\delta d \sim \delta x e_x + \delta y e_y$ is the error in d:

$$|\delta z| \simeq \left| \frac{\delta y_i \hat{\mathbf{z}} \cdot (\mathbf{r}_1 \times \mathbf{r}_2)}{f \hat{\mathbf{r}}_\mathbf{i} \cdot (\mathbf{r}_1 + \mathbf{r}_2) \times \hat{\mathbf{z}}} \right| \,. \tag{2.22}$$

The error for the reconstruction of $\mathbf{\Delta r}$ in the epipolar plane is best shown from the sketch 2.6.

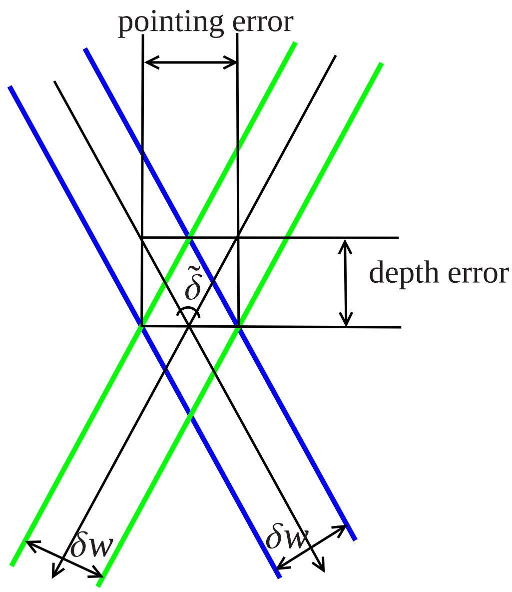

Figure 2.6: Sketch of the reconstruction errors in the epipolar plane.

If we consider an error δx_i expressed in the image coordinates,

$$depth\ error \simeq \frac{\delta w}{\sin(\tilde{\delta}/2)} = \frac{\delta x_i}{f}\frac{r_{sc}}{\sin(\tilde{\delta}/2)}\ , \tag{2.23}$$

$$pointing\ error \simeq \frac{\delta w}{\cos(\tilde{\delta}/2)} = \frac{\delta x_i}{f}\frac{r_{sc}}{\cos(\tilde{\delta}/2)}\ , \tag{2.24}$$

since $\delta w/r_{sc} = \delta x/f$ corresponds to the angular error. Note that the depth error dramatically increases if $\tilde{\delta}$ becomes small while the pointing error decreases if $\tilde{\delta} \rightarrow 180°$.

2.2.3.3 Reconstruction of loops

The reconstruction of loops differs from that of a single point because a loop typically intersects a range of epipolar planes (Fig. 2.7). Hence the agreement in the epipolar plane parameter z cannot be used to check the correspondence of the object in the two images. Rather we can use the range of the epipolar parameter z covered by a loop. This range should be identical from both images if a loop is identified correctly in the images. However, in practical measurements, the foot points often cannot be determined exactly because one of the foot points either lies behind the horizon from one view direction or is immersed in bright EUV moss structures on the solar surface. Still, the epipolar parameter z_{max} of the loop top can be used.

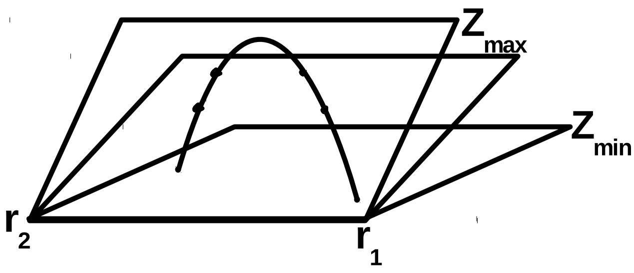

Figure 2.7: Sketch of epipolar planes intersected by a loop.

Another problem with loops which intersect some epipolar lines twice (typically E-W oriented loops) is that even if the loop itself is identified correctly in both images, its two legs may be mixed up. The back projection of a loop from its two images often gives two possible solutions from the intersection of the two projection surfaces (Fig. 2.8). One of the solutions is the correct one and the other solution is usually called a “ghost” loop.

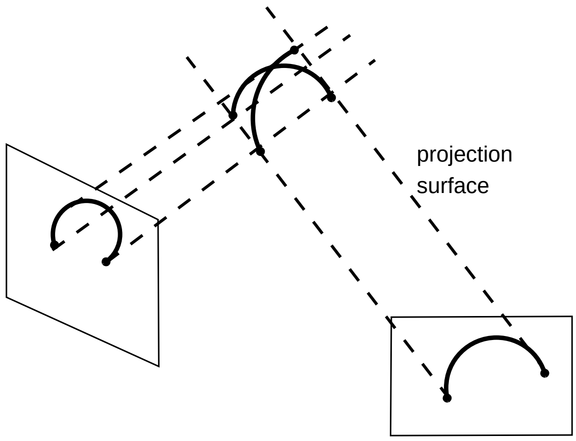

Figure 2.8: Sketch of the projection surfaces.

Error estimate of the reconstructed loop curve follow in essence the error estimates of a single point reconstruction, except that the error volume has to be projected tangentially to the loop. It turns out that the error often is largest at the loop top where the correct and the “ghost” solution come close, i.e. in the epipolar plane z_{max} (for downward bent loops) or z_{min} (for upward bent loops), respectively. Here, the loop projections are parallel to the epipolar line in the respective image and the disparity (i.e., the position along the epipolar line) is less well determined.

2.3 Multi-view B-spline Stereoscopic Reconstruction (MBSR)

Due to localization errors of the curve projection in the images, the stereoscopically reconstructed 3D curve often needs to be smoothed by fitting a 3D polynomial or spline curve. We have developed a method in which the B-spline (see Section 2.26) fit is embedded in the reconstruction. Instead of calculating pairwise reconstructions from multiple views which have to be somehow averaged finally, our method is able to reconstruct a loop curve from its tie-pointed image projections on two or more views directly. It is designed to yield a 3D B-spline as approximation to the reconstructed loop curve, the projections of which optimally matches all tie-points in the images. There is no need to arrange the tie-points from different images pairwise on identical epipolar lines along the loop which would be necessary for a point-by-point reconstruction of a curve. No association of tie points in different images is necessary. After the tie-pointing step, the reconstruction is performed using all tie-points from all images in one go. The local error depends only on how well the tie points are positioned and the 3D reconstruction result is approximated by the 3D spline curve which projects closest to the tie-points in the images.

2.3.1 B-spline curve

A B-spline (base-spline) curve $\mathbf{c}(s)$ is a piecewise polynomial curve constructed of base splines $B_{i,k}(s)$ (de Boor 1985). The final shape of the curve is determined by weights $\mathbf{q}_i$ to each $B_{i,k}$. These weights can geometrically be interpreted as control points $\mathbf{q}_i,\ i = N_{min}; N_{max}$. For a given polynomial order k, a B-spline curve $\mathbf{c}(s)$ is defined as a linear combination of control points $\mathbf{q}_i$ and B-spline (basis-spline) functions:

$$\mathbf{c}(s) = \sum_{i=N_{min}}^{N_{max}} B_{i,k}(s)\mathbf{q}_i\ . \tag{2.25}$$

Each base spline $B_{i,k}$ is made up of piecewise polynomial segments of degree k and has a limited support of $[s_i, s_{i+k+1}]$. They are constructed recursively as follows:

- For the case $k = 0$ we have

$$B_{i,0}(s) = \begin{cases} 1 & \text{if } s \in [s_i, s_{i+1}] \\ 0 & \text{otherwise} \end{cases}$$

- For $k > 0$ we recurse

$$B_{i,k}(s) = m_{i,k}(s)B_{i,k-1}(s) + (1 - m_{i+1,k}(s))B_{i+1,k-1}(s)\ , \tag{2.26}$$

$$m_{i,k}(s) = \frac{s - s_i}{s_{i+k} - s_i},\ s_i < s_{i+k}\ . \tag{2.27}$$

For an extended curve, the range of curve parameter s is divided into N intervals $s \in [s_i, s_{i+1}]$ where $i = 0, N$. Each interval $[s_i, s_{i+1}]$ is influenced by $k + 1$ base functions $B_{i,k},\ B_{i-1,k}, ..., B_{i-k,k}$ and is therefore influenced by $k + 1$ control points $\mathbf{q}_i,\ \mathbf{q}_{i+1}, ..., \mathbf{q}_{i-k}$.

In our model we use cubic B-splines with $k = 3$. The intervals have unit length. From the recursive formula (2.26) we can build the resulting polynomials inside each interval. For the fixed interval $[s_i, s_i + 1]$, the curve can explicitly be written as polynomial of $\sigma = s - s_i$

$$\mathbf{c}(s) = \frac{1}{6}\begin{pmatrix} 1 & \sigma_i & \sigma_i^2 & \sigma_i^3 \end{pmatrix} \begin{pmatrix} 1 & 4 & 1 & 0 \\ -3 & 0 & 3 & 0 \\ 3 & -6 & 3 & 0 \\ -1 & 3 & -3 & 1 \end{pmatrix} \begin{pmatrix} \mathbf{q}_{i+3} \\ \mathbf{q}_{i+2} \\ \mathbf{q}_{i+1} \\ \mathbf{q}_i \end{pmatrix}\ . \tag{2.28}$$

Cubic B-splines are continuous functions and have two continuous derivatives. The B-spline curve which fits the tie-points should also be sufficiently smooth. This requirement is also justified by the physics of loops. They represent magnetic field lines and the magnetic stresses will straighten field lines as much as possible. The spline curve has to satisfy therefore two constraints: a minimum distance to the data points and a sufficient smoothness. Our multi-view reconstruction is therefore based on a least-squares evaluation of the distances between tie-points $\mathbf{x}_{i,j}$ in image j and the projection $P_j \cdot \mathbf{c}(s_{i,j};\mathbf{q})$ of the reconstructed 3D curve $\mathbf{c}(s)$ onto image j on the one hand and the integrated second derivative of the curve representing its lack of smoothness on the other hand. The least-squares code minimizes

$$\sum_{\text{images } j} \sum_{\text{tie-point i}} |P_j \cdot \mathbf{c}(s_{i,j};\mathbf{q}) - \mathbf{x}_{i,j}|^2 + \mu \int_{s_{min}}^{s_{\max}} |\frac{d^2}{ds^2} \cdot \mathbf{c}(s;\mathbf{q})|^2 ds \tag{2.29}$$

with respect to the node points $\mathbf{q}_k$. The second term ensures a smooth regularized curve $\mathbf{c}(s)$ depending on the weight μ. The curve parameters $s_{i,j}$ in Eq. (2.29) are defined as the values of s for which the function $|P_j \cdot \mathbf{c}(s_{i,j};\mathbf{q}) - \mathbf{x_{i,j}}|$ reaches its minimum value

$$s_{i,j} = \operatorname*{argmin}_s |P_j \cdot \mathbf{c}(s;\mathbf{q}) - \mathbf{x}_{i,j}| \,. \tag{2.30}$$

Through this side-constraint, the problem to minimize Eq. (2.29) is nonlinear. The practical solution of Eq. (2.29) and Eq. (2.30) proceeds iteratively. In each iteration step we solve the linear least-squares problem Eq. (2.29) for $\mathbf{q}$ assuming $s_{i,j}$ given. Next, given the new spline curve defined by control points $\mathbf{q}$, we have to readjust the curve parameters $s_{i,j}$ of all tie-points in all images using Eq. (2.30).

Instead of calculating pairwise reconstructions from multiple views which have to somehow be averaged finally, our code is capable to reconstruct tie-pointed curves using two or more views directly. It is designed to yield the optimal match to all tie-points which an average of pairwise 3D reconstructions usually does not achieve. There is no need to arrange the tie-points from different images at pairwise equal position along the loop. No association of tie points in different images is necessary. The program has a widget which displays the images and helps to identify, match and tie-point the structures. After the tie-pointing step, the reconstruction is performed using all tie-points from all images in one go. This way we obtain a more direct, efficient and robust reconstruction which combines the calculations of a smoothing spline directly with the reconstruction.

2.4 3D modeling of the magnetic field through extrapolation

The modeling of the magnetic field in the solar corona is possible under certain assumptions. As mentioned in introductory chapter, plasma beta gives information about which force dominates in a certain part of the solar atmosphere. In the corona, $\beta \ll 1$ which means that the magnetic pressure dominates over the plasma pressure and also over gravity and the kinematic plasma flow pressure (Wiegelmann and Sakurai 2012). Under these assumptions, stationarity of the plasma requires to lowest order the vanishing of the Lorenz-force:

$$\mathbf{j} \times \mathbf{B} = 0 , \tag{2.31}$$

which implies that the current density $\mathbf{j}$ is parallel to the magnetic field $\mathbf{B}$.

Inserting Ampere's law (Eq. 1.1) in the expression of the Lorenz force (Eq 2.31) we obtain

$$(\nabla \times \mathbf{B}) \times \mathbf{B} = 0 . \tag{2.32}$$

The magnetic field which satisfies Eq. (2.32) together with the solenoidal condition ($\nabla \cdot \mathbf{B} = 0$) is termed the force-free field approximation. Eq. (2.32) is a non-linear equation (Wheatland et al. 2000). We can rewrite it by introducing the current-to-field ratio α as

$$\nabla \times \mathbf{B} = \alpha \mathbf{B} , \tag{2.33}$$

$$\mathbf{B} \nabla \alpha = 0 . \tag{2.34}$$

The divergence applied to Eq. (2.33) gives Eq. (2.34) which tells us that α is constant along any field line but can vary across the magnetic field.

The force-free parameter, α can be set in three different ways:

1. **Potential field model** The simplest approach is $\alpha = 0$. In this case, $\mathbf{B}$ is the potential field (Wiegelmann and Sakurai 2012). We can write the magnetic field as a function of the scalar potential ϕ,

   $$\mathbf{B} = -\nabla \phi . \tag{2.35}$$

   A potential magnetic field model for the coronal magnetic field can be derived from Gauss theorem, e.g., using the LOS photospheric magnetic field component as boundary condition (Wiegelmann and Sakurai 2012).

   Shortcoming of the model

   Potential field is the magnetic field with the lowest magnetic energy for given normal boundary conditions. It excludes any current. In an eruptive process, the corona requires free magnetic energy which a pre-eruptive potential field cannot supply (Wiegelmann and Neukirch 2003). The field lines of a potential magnetic field differ from the observed coronal loops especially near active regions (Wiegelmann and Sakurai 2012).

2. **Linear force-free field (LFFF) model**

   The second approach is to define the force-free parameter α in Eqs. (2.33) and (2.34) as a constant different from zero in the entire corona. The calculation of a LFFF magnetic field model requires the solution of a Helmholtz equation instead of a Laplace equation for the potential field. Again a scalar boundary condition, e.g measurements of the LOS photospheric magnetic field are sufficient. The force-free parameter α is a priori unknown but it can be tuned to fit best with observations (Wiegelmann and Sakurai 2012).

   Shortcoming of the model:

The assumption of constant α in the computational volume is not consistent with observations. Approximate values of α can be calculated from surface vector magnetograms by $\alpha \approx \nabla \times B_{horiz}/B_{vert}$. Changes of α were seen for example, in active regions. Wiegelmann and Neukirch (2003) tried to fit the optimal force-free parameter α by comparing individual LFFF model field lines with coronal plasma structures. They found that the optimal value of α varies from positive to negative values in the same active region.

3. **Nonlinear force-free field (NLFFF) model**

The nonlinear force-free field (NLFF) model is defined by Eqs. (2.33) and (2.34) with $\alpha = \alpha(\mathbf{r})$.
To model the coronal magnetic field using nonlinear force free field extrapolations, one needs as input data surface observations of all three components of the magnetic field. Since a couple of years, observations from various observatories and spacecraft provide photospheric magnetograms of the full magnetic field vector. These data can be extrapolated into the corona by solving a nonlinear boundary value problem based on the assumption of a force-free coronal field (NLFFF extrapolation). Different and competing numerical procedures are in use to tackle this boundary value problem (Schrijver et al. 2006, Inhester and Wiegelmann 2006).
The most commonly used methods to produce NLFFF field models for the corona are the Grad-Rubin method, the magnetofrictional method and the optimization method (Schrijver et al. 2006).

Shortcoming of the model:

Even though the comparison between potential field, LFFF and NLFFF models shows that the NLFFF model best fits with observations, some limitations still exist for this model. For the nonlinear force-free field (NLFFF) extrapolation to be applicable, we require a more or less stationary coronal magnetic field which needs some degree of local force balance. The low beta value in the corona distinguishes the Lorentz force as the dominant force and stationarity requires its absence. The vanishing of $\mathbf{B} \times (\nabla \times \mathbf{B})$ is a strong constraint for the coronal field but the extrapolation problem is still ill-posed and the resulting field $\mathbf{B}$ is more affected by errors in the boundary data, the higher the altitude above the surface. These errors have multiple causes ranging from mere measurement errors of the photospheric field to the ambiguous orientation of the observed transverse field component (180°-ambiguity, Metcalf et al. 2006) and the absence of the assumed low-β plasma in the small height range between the photosphere and the base of the corona.

2.4.1 NLFFF optimization method

The optimization method has originally been proposed by Wheatland et al. (2000) and extended by Wiegelmann (2004), Wiegelmann and Inhester (2010), Tadesse et al. (2011). The essential approach is to minimize a scalar cost function L_{tot} which consists of a number of terms L_n quantifying constraints the final solution should satisfy.

The first two terms from the functional L_{tot} are:

$$L_1 = \frac{1}{V}\int_V w_f \frac{|(\nabla \times \mathbf{B}) \times \mathbf{B}|^2}{B^2}\, d^3r\,, \tag{2.36}$$

$$L_2 = \frac{1}{V}\int_V w_f |\nabla \cdot \mathbf{B}|^2\, d^3r\,. \tag{2.37}$$

The force-free and divergence-free conditions are satisfied if the terms L_1 and L_2 are minimized to zero. w_f is a weighting function introduced in order to handle the unknown lateral and top boundary. The computational box has an inner physical domain and a boundary layer with a certain thickness. The weighting parameter w_f varies smoothly and monotonically from unity on the boundary of the inner physical domain to zero at the outer boundary of the domain (Wiegelmann 2004).

The next term from the functional L_{tot} is

$$L_3 = \frac{1}{S}\int_S (\mathbf{B} - \mathbf{B}_{\text{obs}}) \cdot \text{diag}(\sigma_{\text{q}}^{-2}) \cdot (\mathbf{B} - \mathbf{B}_{\text{obs}})\, d^2r\,, \tag{2.38}$$

where $\mathbf{B}_{\text{obs}}$ is the observed field on the photospheric boundary surface S and $\sigma_q(\mathbf{r})$ are estimated measurement errors for the three field components $q = x, y, z$ on S. The estimated error $\sigma_z(\mathbf{r})$ of the line-of-sight (LOS) component of the photospheric magnetic field $\mathbf{B}_{\text{LOS}}$ is set to unity since in our test calculations $\mathbf{B}_{\text{LOS}}$ is measured with high accuracy. For the the transverse field $\mathbf{B}_{\text{trans}}$, the estimated error is typically much higher and the ratio $\sigma_x/\sigma_z \simeq \sigma_x/\sigma_y = \mathbf{B}_{\text{trans}}/\max(\mathbf{B}_{\text{trans}})$. It even may be set to infinity if at the position $\mathbf{r}$ the transverse field has not been measured at all (Wiegelmann and Inhester 2010, Tadesse et al. 2011).

To this end, the functional to be minimized is

$$L_{\text{tot}} = \sum_{n=1}^{3} \xi_n L_n\,. \tag{2.39}$$

The regularization parameters ξ_n, are free parameters and control the relative influence of the terms L_n. These parameters could vary between zero and infinity. The Lagrangean multiplier ξ_3 allows to tune how closely the model field matches the boundary measurements. Since the measurements are often noisy and therefore inconsistent, a close agreement between $\mathbf{B}$ and $\mathbf{B}_{\text{obs}}$ at the photospheric boundary by a large value of ξ_3 is likely to prevent terms L_1 and L_2 to be iterated to small values. A study using observed vector magnetograms showed that the Lagrangean multiplier ξ_3 also influences the speed of the magnetic field relaxation during the iteration.

In our code the Eq. (2.39) is minimized by means of a Landweber iteration by taking the functional derivative of Eq. (2.39). Introducing the continuous iteration count t, we obtain an iteration equation for the magnetic field (Wiegelmann and Sakurai 2012):

$$\frac{\partial L_{\text{tot}}}{\partial t} = \xi_1 \int_V \frac{\partial \mathbf{B}}{\partial t} \cdot \mathbf{F}_1\, d^3r + \xi_2 \int_S \frac{\partial \mathbf{B}}{\partial t} \cdot \mathbf{F}_2\, d^3r + \xi_3 \int_S \frac{\partial \mathbf{B}}{\partial t} \cdot \mathbf{F}_3\, d^2r\,, \tag{2.40}$$

$$\text{where } \mathbf{F}_n = \frac{\partial L_n}{\partial \mathbf{B}}$$

is the variational derivative of $L(\mathbf{B})$

The Landweber iteration then reads

$$\mathbf{B} \leftarrow \mathbf{B} - \mu \sum_{n=1}^{3} \xi_n \mathbf{F}_n \,. \tag{2.41}$$

This iteration reduces L_{tot} at each iteration step when the step size μ is chosen small enough. The code automatically reduces the step size μ if this condition is not met. The iteration is stopped if μ reaches a lower threshold value, here set to 10^{-7}.

2.5 3D reconstruction of coronal loops

Two major approaches have been employed to derive the 3D shape of coronal loops. The stereoscopic approach is geometric as described in Section 2.2 and makes use of at least two different views of the same coronal loop. Since the launch of the STEREO spacecraft a number of authors developed methods to perform the 3D reconstruction of coronal loops. The first reconstruction of the 3D shape of coronal loops from an active region using stereoscopy was achieved by Feng et al. (2007). As we have already said in a previous section, one of the steps in stereoscopic reconstruction is the visual identification of the same loops in both images. In EUV images often we see the emission from a bundle of loops which makes this step quite difficult and from a visual inspection often multiple correspondences of the same loop seem possible. The images provided by existing instruments do not have sufficient accuracy to identify a single loop uniquely. This was the reason why Feng et al. (2007) used linear force-free field extrapolations to help with the identification in this reconstruction step. Calculating LFFF magnetic field models for different values of α for the active region studied, they used the proximity to any of the model loops to determine a correspondence. The loop pairs found to be closest to a projected model field line were chosen for the stereoscopic reconstruction. In another study by Aschwanden et al. (2008) the 3D geometry of 30 loop structures were derived. The authors could identify and select seven complete loops and 23 segments of loops. They derived the maximum and minimum height of the loops, the inclination angle of the loop plane of each complete loop and circularity and coplanarity of loops. The results from the 3D stereoscopic reconstruction together with DEM estimates from the loop brightness at different EUV wavelengths were used by Aschwanden et al. (2008) to derive the electron temperatures and densities for these coronal loops.

Another method which was used to derive the 3D shape of coronal loops makes use of Doppler shift measurements. Syntelis et al. (2012) used EUV images in different Fe wavelengths from the Hinode spacecraft to trace the loops of interest. Using a geometrical model, they calculate the 3D structure of the coronal loops from observations from a single view direction by including Dopplershifts observed along the loop. In their model they assume that the loops are stationary, each of them lies in a fixed plane and they carry a divergence-free, field-aligned plasma flow along them. With these assumptions, the 2D loop trace from EUV images and the Doppler shifts along the loop, they could derive the inclination angle between the loop plane and the local solar vertical. They also made a comparison between their result and a field line from a linear force-free field extrapolation. The mean inclination difference between the direction of the reconstructed loops and the linear force-free model field lines was around $14.5^\circ \pm 4.5^\circ$.

Another way to get the 3D shape of coronal loops is based on the extrapolation of the magnetic field. As we have already mentioned in Section 2.4, the potential and LFF field extrapolations often disagree with the observations, like in the study of Wiegelmann et al. (2005) or Syntelis et al. (2012). A better though not perfect fit between the model field and the observations is achieved for nonlinear force-free field (NLFFF) extrapolation. In a study by De Rosa et al. (2009) field line solutions of various NLFFF extrapolation methods (see Section 2.4) have been compared with 3D loops reconstructed by stereoscopy. In Fig. 2.9 we show a comparison of the 3D loops reconstructed from STEREO with selected field lines from an NLFFF extrapolation.

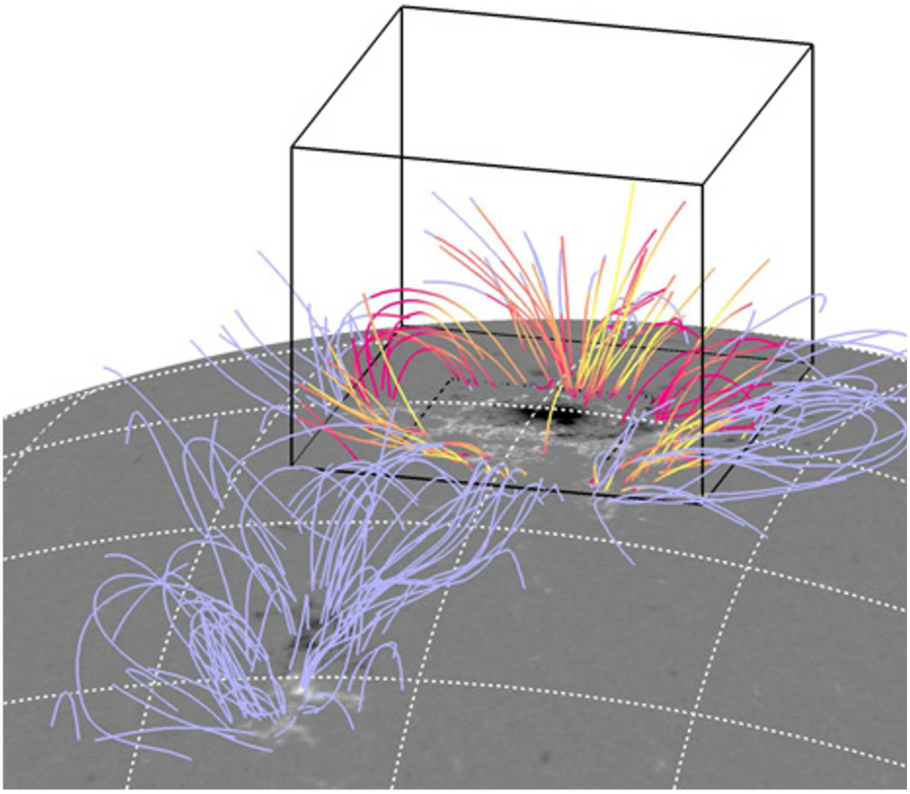

Figure 2.9: Comparison between coronal loops and NLFFF extrapolation; Figure reproduced from De Rosa et al. (2009). The surface colour shows the field normal component from MDI/SOHO.

The box represents the computational domain for NLFFF methods. Inside the box, the colored lines from yellow to red correspond to field lines reconstructed with the best NLFFF extrapolation solution identified by the analysis and the loop color code depends on the local misalignment angle between the NLFFF extrapolation solution and the observations. Yellow stands for a misalignment angle of less than 5 degrees and red for more than 45 degrees. All field models obtained complied with the boundary data within reasonable error but only few model field lines reproduced the loops reconstructed from stereoscopy. Even though the study suffered from the fact that the loops from stereoscopy were not well located above the magnetogram area which supplied the boundary condition for the extrapolation, the study shed some light on the ill-posed nature of the extrapolation problem: measurement errors as they are probably unavoidable in state-of-the-art magnetograms can easily degrade the quality of the extrapolation result, especially at higher altitudes above the solar surface.

2.5.1 S-NLFFF: A method which combines MBSR and NLFFF

In this section, we present the extension of the NLFFF variational method such that besides the boundary data, additional loop data, e.g. obtained from a three-dimensional stereoscopic reconstruction, is also taken care of. We call this new method S-NLFFF where the S stands for stereoscopy. We add a new term to the NLFFF optimization terms which constrains the magnetic field to be aligned to these loops obtained. The loops are represented by 3D functions $\mathbf{c}_i(s)$ where the loop parameter s is scaled to the geometrical length along the loop and index i identifies different loops. The new term has the form

$$L_4 = \sum_i \frac{1}{\int_{\mathbf{c}_i} ds} \int_{\mathbf{c}_i} \frac{|\mathbf{B} \times \mathbf{t}_i|^2}{\sigma_{c_i}^2}\, ds\,, \qquad (2.42)$$

$$\text{where} \quad \mathbf{t}_i = \frac{d\mathbf{c}_i}{ds}\,.$$

Here, $\mathbf{t}_i(s)$ is the tangent vector along the ith loop and has unit length due to the scaling of the loop parameter s. The magnetic field $\mathbf{B}$ in Eq. (2.42) is the field at the loop point $\mathbf{c}(s)$ and by means of the cross product with $\mathbf{t}(s)$ the term L_4 vanishes if the field is tangential to the loop along its entire length.

Just as the boundary data above, the loop reconstruction may also include errors. These depend on the stereoscopic view geometry and may well vary along the loop. In order to take account of these errors, we include a function $\sigma_{\mathbf{c}_i}(s)$ which is a relative measure of the estimated error of the tangent direction $\mathbf{t}_i(s)$ along the loop i.

With the new term L_4 added, the functional L_{tot} becomes:

$$\begin{aligned} L_{\mathrm{tot}} &= \xi_1 \frac{1}{V} \int_V w_f \frac{|(\nabla \times \mathbf{B}) \times \mathbf{B}|^2}{B^2}\, d^3r + \xi_2 \frac{1}{V} \int_V w_f |\nabla \cdot \mathbf{B}|^2\, d^3r \\ &+ \xi_3 \frac{1}{S} \int_S (\mathbf{B} - \mathbf{B}_{\mathrm{obs}}) \cdot \mathrm{diag}(\sigma_{\mathrm{q}}^{-2}) \cdot (\mathbf{B} - \mathbf{B}_{\mathrm{obs}})\, d^2r + \xi_4 \sum_i \frac{1}{\int_{\mathbf{c}_i} ds} \int_{\mathbf{c}_i} \frac{|\mathbf{B} \times \mathbf{t}_i|^2}{\sigma_{c_i}^2}\, ds\,. \end{aligned} \qquad (2.43)$$

For practical calculations, the magnetic field, its boundary data and the loop data are given on discrete grids. The respective discretized cost function contributions will be named Ł$_i$. For the magnetic field and photospheric boundary data we use a straight forward regular, equidistant Cartesian grid with nodes $\mathbf{r}_\mathbf{k} = (k_x dh, k_y dh, k_z dh)$ and grid size dh. Here, $\mathbf{k} = (k_x, k_y, k_z)$ is short-hand for a 3D multi-index of the grid indices along the three axes (see Fig. 2.10). A complication with the new term Ł$_4$ arises because it does not share the common Cartesian grid of the field and boundary data. If we discretized the

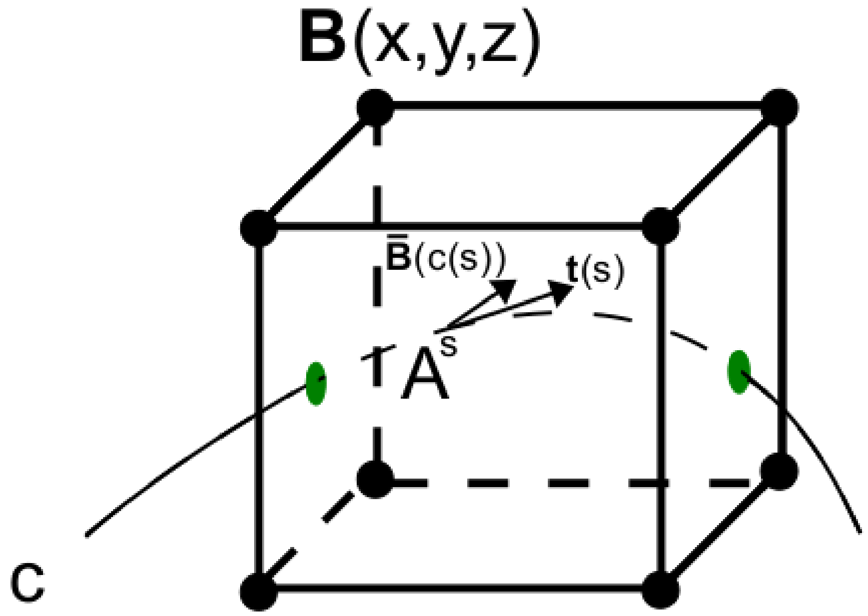

Figure 2.10: Sketch of a box defined by 8 neighboring grid points $\mathbf{r_k}$ (black dots). A segment of the curve $\mathbf{c}$ (dash dotted curve) cross this box; $\overline{\mathbf{B}}(\mathbf{r})$ is the interpolated field and $\mathbf{t}(s)$ is the tangent in the point A.

loop parameter s equidistantly by $s \rightarrow s_j = j\Delta s$ the new variational term becomes

$$Ł_4 = \sum_i \frac{1}{\sum_j \Delta s} \sum_j \frac{|\overline{\mathbf{B}}(\mathbf{c}_i(s_j)) \times \mathbf{t}_i(s_j)|^2}{\sigma^2_{\mathbf{c}_i}(s_j)} \Delta s \,, \tag{2.44}$$

where $\overline{\mathbf{B}}(\mathbf{r})$ is the field interpolated from neighboring grid points $\mathbf{r_k}$ onto a position $\mathbf{r}$ and $\sigma^2_{\mathbf{c}}(s_j)$ is the variance of the tangent vector $\mathbf{t}(s_j)$ (we temporarily drop the loop counting index i).

We use the straight forward trilinear interpolation which is a weighted average of the values $\mathbf{B}(\mathbf{r_k})$ at the cell nodes of the cell which includes $\mathbf{c}(s)$. The weight for each node is a product of $x,\ y,\ z$ weights each of which is proportional to one minus the distance $\mathbf{c}(s) - \mathbf{r_k}$ along the respective axis.

In order to perform the minimization of Eq. (2.43), we need the functional derivatives of the discretized $Ł_i$ with respect to the field components $\mathbf{B}(\mathbf{r_k})$. For the conventional terms, $Ł_n$, $n = 1, 2, 3$ these derivatives have been calculated in Wiegelmann (2004), Wiegelmann and Inhester (2010). For the new term we find

$$\begin{aligned} F_{4,\mathbf{q}}(\mathbf{r_k}) &= \frac{\partial Ł_4}{\partial \mathbf{B_q}(\mathbf{r_k})} \\ &= \sum_i \frac{2}{\sum_j \Delta s} \sum_j \frac{d\mathbf{F}_{\mathbf{c}_i}(s)}{\sigma^2_{\mathbf{c}_i}(s_j)} \cdot \frac{\partial \overline{\mathbf{B}}(\mathbf{c}_i(s_j))}{\partial \mathbf{B_q}(\mathbf{r_k})} \Delta s \,, \end{aligned} \tag{2.45}$$

$$\text{where} \quad d\mathbf{F}_{\mathbf{c}_i}(s) = \overline{\mathbf{B}}(\mathbf{c}_i(s)) - (\overline{\mathbf{B}}(\mathbf{c}_i(s)) \cdot \mathbf{t}_i(s))\mathbf{t}_i(s) \,.$$

for all three spatial components $\mathbf{q}$ and all grid points $\mathbf{k}$. Note that $d\mathbf{F}_{\mathbf{c}_i}$ is the projection of the local $\overline{\mathbf{B}}$ normal to the loop tangent. For a linear interpolation in the regular Cartesian grid which we use here, $\partial\overline{\mathbf{B}}/\partial\mathbf{B}_\mathbf{q}(\mathbf{r}_\mathbf{k})$ is just the interpolation weight of field component $\mathbf{B}_\mathbf{q}(\mathbf{r}_\mathbf{k})$ in $\overline{\mathbf{B}}(\mathbf{c}_i(s_j))$. This weight is nonzero only if the loop point $\mathbf{c}_i(s_j)$ is located in a grid box for which $\mathbf{r}_\mathbf{k}$ is one of its corners.

The minimization of $Ł_{\mathrm{tot}}$ is then again performed by a Landweber iteration

$$\mathbf{B} \leftarrow \mathbf{B} - \mu \sum_{n=1}^{4} \xi_n \mathbf{F}_n \,. \tag{2.46}$$

We will call $Ł_{\mathrm{tot}}^{\infty}$ and $Ł_i^{\infty}$ the residual values of the cost function and its decomposition at the end of the iteration.

With $Ł_i^{\infty} > 0$, the weights ξ_i in $Ł_{\mathrm{tot}}$ play an important role because they determine how the residual value of $Ł_{\mathrm{tot}}^{\infty}$ is distributed among the individual terms $Ł_i^{\infty}$. In general, the residual value of a single $Ł_i^{\infty}$ can be reduced to very smaller values if ξ_i is enhanced with respect the other ξ_j, $j \neq i$. However, the other terms $Ł_j^{\infty}$ will then increase depending on how much the constraints represented by the discretized terms $Ł_i$ and $Ł_j$ are in conflict. This way, each of the $Ł_i^{\infty}$ obtained at the end of the minimization can be considered a function of the whole set of weights $\{\xi_1, \ldots, \xi_4\}$. The goal, of course, is to choose these weights such that all $Ł_i^{\infty}$ are reduced to their lowest possible value.

Typically, a term $Ł_i^{\infty}$ which depends on observed data like $Ł_3$ and $Ł_4$ cannot be decreased to zero but is bounded below by a “discretization-noise ” or “data-noise“ level. In a $\log Ł_i^{\infty}$ vs $\log Ł_j^{\infty}$ representation, the solutions for different ξ_i and ξ_j are then located on a L-shaped curve with the two legs defining the two noise levels. The optimum solution is then located in the corner of the L-curve (Hansen 2010) where $\log Ł_i^{\infty} + \log Ł_j^{\infty}$ is minimized. Generalized to several regularization terms, the best choice of $\xi_1, \ldots, \xi_4$ is obtained if $\sum_i \log Ł_i^{\infty}(\xi_1, \ldots, \xi_4)$ is minimal.

There are, however, additional considerations. For example, if σ_q and σ_c introduced in Eqs. (2.38) and (2.42) represent realistic error estimates, we might want to tune the residual value of these terms to about unity. At these values, the extrapolated field complies with the observations to the order of the observational errors. With any further reduction of $Ł_3$ and $Ł_4$, we would try to adjust the field $\mathbf{B}(\mathbf{r}_\mathbf{k})$ to the data noise at the expense of minimizing its divergence and Lorentz force.

3 Instrumentation

In this chapter the used missions and their instruments are described. For the eruptive prominences described and analyzed in Chapter 4, we used data from the STEREO (Solar Terrestrial Relation Observatory) and SDO (Solar Dynamic Observatory) missions. From the two STEREO spacecraft, we used images from the extreme ultraviolet imager (EUVI) at the wavelength of $\lambda = 304$ Å. From the SDO mission, EUV images were provided by the Atmospheric Imager Assembly (AIA) in several wavelengths. We used only the images in the wavelength of $\lambda = 304$ Å. The white-light coronagraph data was taken by the SECCHI (Sun-Earth-Connection Coronal and Heliospheric Investigation) telescopes package onboard STEREO.

3.1 Solar Terrestrial Relation Observatory (STEREO) mission

The STEREO mission is composed of two spacecraft, named STEREO A (Ahead) and STEREO B (Behind) (Kaiser et al. 2007). Their orbits are heliocentric with a period close to an Earth year. Each year, the angle between them increases by approximately 44° to 45°. The spacecraft began to observe at the end of 2006. Fig. 3.1 shows the position of the spacecraft A and B at three different times from their launch till present. The red and blue dots represent the spacecraft STEREO A and B respectively. The yellow and green dots are the position of the Sun and Earth, respectively. The x and y axes are drawn in the heliocentric Earth ecliptic (HEE) coordinate system (Thompson 2006).

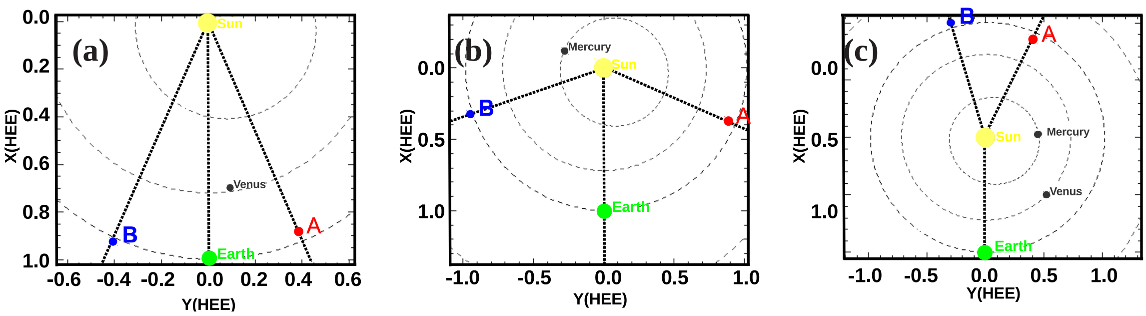

Figure 3.1: STEREO A and B position in a) 2008, b) 2010 and c) 2014 (adapted from http://stereo-ssc.nascom.nasa.gov/where.shtml).

The Sun-Earth-Connection Coronal and Heliospheric Investigation (SECCHI) package of optical telescopes is mounted onboard each of the two STEREO spacecraft. The SECCHI package incorporates five different instruments, which cover a field of view from the solar surface to almost 1 A.U. in the plane of the sky. The five instruments are divided in three categories. The first category consist of the extreme ultraviolet imager (EUVI) which observes the chromosphere and the low corona. In the second category of instruments are the concentric, Sun-centered coronagraphs (COR1, COR2) which record images from the inner and outer corona. Their field of view ranges from 1.4 to 15 $R_\odot$. The third category consist of two heliospheric imagers (HI1, HI2) which are off-axis white-light coronagraphs. They take images of the interplanetary space from 15 to 215 $R_\odot$ on the respective Earthward side of Sun (Howard et al. 2008b). A composite image from data of all instruments is presented in Fig. 3.2.

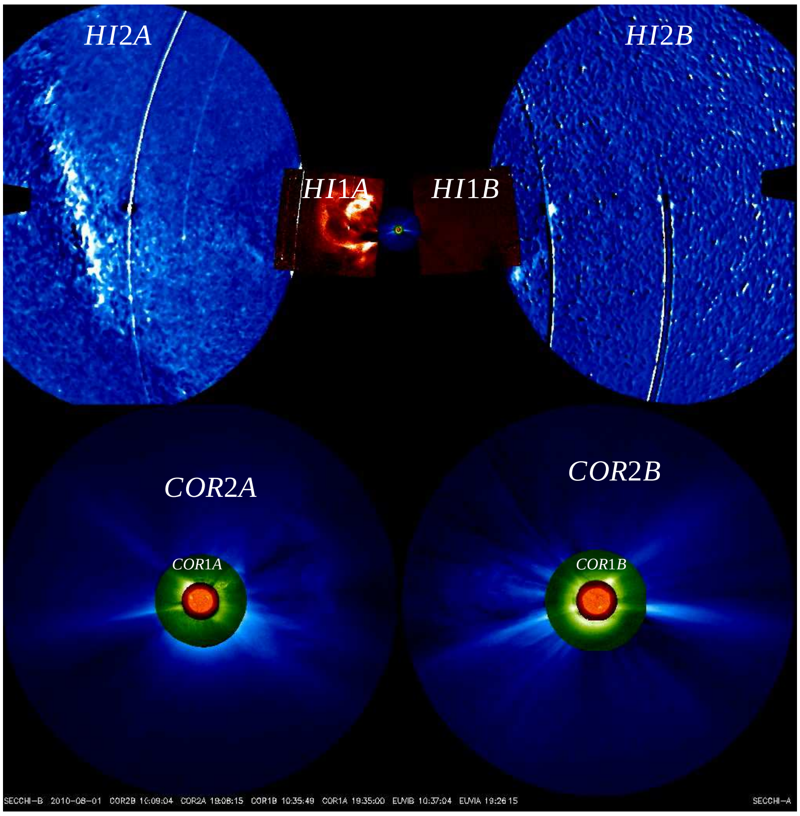

Figure 3.2: A composite image (upper part) of all SECCHI instruments recording a CME on 1 August 2010. In the lower part of the images we can see a magnification of the central part of the upper half of the image. The images from the instruments are color coded: the Sun in EUVI 304 Å waveband is displayed in orange in the middle of the upper and lower part of the image; the next outer layer colored in green shows the imaging with COR1 followed by the blue layer, which shows the outer corona recorded with COR2. The image colored in red in the upper part of the image shows the recording from heliospheric imager (HI) I instrument and the outer blue shows the heliospheric imager (HI) II (http://secchi.nrl.navy.mil).

The objectives of the STEREO mission are to understand the initiation mechanism of the CMEs, their geometry, magnetic topology and propagation into the interplanetary

space (Kaiser et al. 2007).
Previous coronagraph instruments were limited for the investigation of Earth-directed CMEs, because in the first phases of the eruption these CMEs were hidden by the occulting coronagraph disk. This fact made it difficult to measure their true velocity and size (Thompson et al. 2010). The two view directions provided by the two STEREO spacecraft opened the possibility for a 3D reconstruction of objects and for tracking them in the inner heliosphere till Earth.

3.1.1 Extreme Ultraviolet Imaging (EUVI) telescope

The EUVI telescope onboard STEREO A and B spacecraft images the Sun out to 1.7 $R_\odot$. It observes the chromosphere in the emission of ionized helium at a wavelength λ = 304 Å and the low corona in the emission of ionized iron at three different wavelengths $\lambda = 171, 195, 284$ Å (Howard et al. 2008b).

The EUVI instrument is a normal-incident Ritchey-Chrétien telescope (see Fig. 3.3).

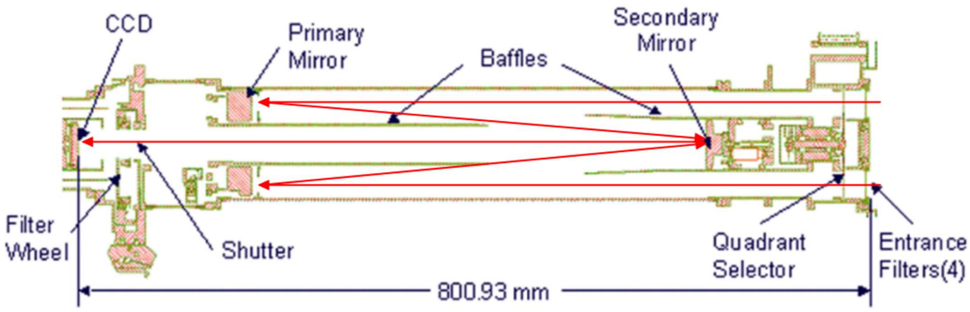

Figure 3.3: The cross-section of the EUVI Ritchey-Chrétien telescope with the light path (red arrows), adapted from Howard et al. (2008b).

The mirrors are divided in four quadrants and each quadrant is optimized for one of the four EUV emissions wavelengths. The telescope pupil is positioned right in front of the primary mirror and is defined by an aperture mask which has a circular cut hole like the one from the entrance filter (Howard et al. 2008b). The spatial sampling of the instrument is 1.6 arcsec/pixel (Wuelser et al. 2004).

The radiation enters the telescope through an Aluminium filter which blocks most of the UV, visible and IR and which keeps the solar heat out of the telescope. The transmitted radiation continues through an aperture selector to one of the four quadrants of the optics, encounters the primary and secondary mirrors which are designed with a narrow-band coating for one of four EUV lines. The radiation will pass through another Aluminium filter which will remove the remaining visible and IR radiation (Wuelser et al. 2004). The exposure time is determined by a rotating blade and the image sensor is a CCD (charge-coupled device) in the focal plane (Howard et al. 2008b).

3.1.2 Inner and outer coronagraph

The second type of instruments of the SECCHI package are the coronagraphs. In order to better suppress the scattered light, there are two coronagraphs. The inner coronagraph

(COR1) observes the inner corona between 1.4 and 4 $R_\odot$ (Thompson et al. 2010) and the outer coronagraph (COR2) observes the corona between 2.5 and 15 $R_\odot$ (Howard et al. 2008b). The inner coronagraph (COR1) is a Lyot internally occulting refractive corona-

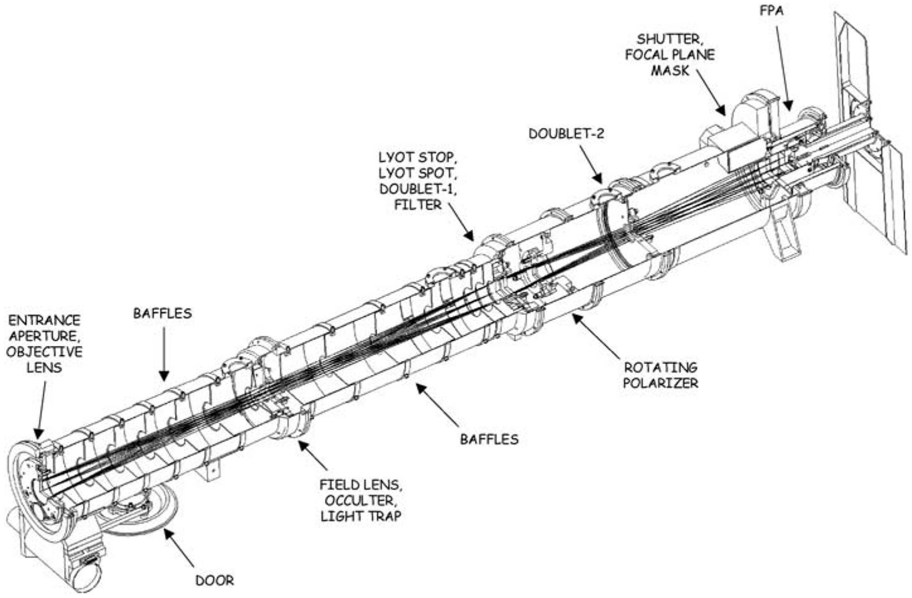

Figure 3.4: Optomechanical drawing of the inner coronagraph COR1 onboard the STEREO spacecraft. Image taken from Howard et al. (2008b).

graph (Thompson et al. 2010). Fig. 3.4 shows the design of this instrument. After the photospheric light enters through the front aperture (Howard et al. 2008b), the objective lens focuses the solar image onto the occulter (Thompson et al. 2010). In order to eliminate the largest source of stray light in the system, the light diffracted by the front aperture is focused onto a Lyot stop and removed. The light which passes the Lyot stop encounters a linear polarizer which extracts the polarized brightness signal at three polarization angles 0, 120 and 240 degrees. Another purpose of the polarizer is to suppress the remnant scattered light (Thompson et al. 2010). A series of lenses refocus the coronal light, which is filtered in the white light spectrum with a 22.5 nm wide bandwidth centered at the H_α wavelength of 656 nm (Howard et al. 2008b).
The COR1 instrument takes images with a pixel size of 2048x2048 with 3.75 arcsec pixel^{-1} resolution. For this practical purpose the data is mostly binned to either 1024x1024 or 512x512 with a corresponding spatial scale of 7.5 or 15 arcsec pixel^{-1} (Thompson et al. 2010).

The outer coronagraph (COR2) is an externally occulted Lyot coronagraph. Just like the inner coronagraph, COR2 provides polarized brightness images at the three polarization angles, 0, 120 and 240 degrees, with a spectral filter which transmits from 650 nm to 750 nm (Howard et al. 2008b). At full resolution, the outer coronagraph provides images of 1024x1024 pixels with a resolution of 14.7 arsec pixel^{-1}.

3.2 Solar Dynamic Observatory (SDO)

The SDO (Solar Dynamic Observatory) spacecraft was launched in February 2010 and takes high cadence and high resolution images of the entire Sun from an inclined geosynchronous orbit (Lemen et al. 2012). The main objective of the mission is to determine the solar variability, how the Sun drives global change and how it influence the Earth (Lemen et al. 2012). The SDO spacecraft carries onboard three types of instruments: the Atmospheric Image Assembly (AIA) which observes the solar atmosphere in various wavelengths representative of temperatures in the range of 6 000 and 10^7 K (Pesnell et al. 2012); the Heliospheric Magnetic Imager (HMI), which is designed to measure solar oscillations and the three components of the photospheric magnetic field vector (Couvidat et al. 2012); Extreme Ultraviolet Variability Experiment (EVE) instrument is designed to measure the solar extreme ultraviolet (EUV) irradiance (Woods et al. 2012).

3.2.1 Atmospheric Imaging Assembly (AIA)

In this thesis we will employ data from AIA and therefore we describe this instrument in more detail.

The Atmospheric Imaging Assembly (AIA) is an array of four telescopes which observes the solar atmosphere in ten different wavelengths (seven in EUV, two in UV and one in visible light) (Pesnell et al. 2012). The lower corona is imaged in five ionized iron wavelengths and one emitted by He II. Each of the four telescopes has a spatial resolution of 0.6 arcsec pixel^{-1}, a field of view 1.5 $R_\odot$ and a CCD record camera of 4096x4096 pixels (Lemen et al. 2012).

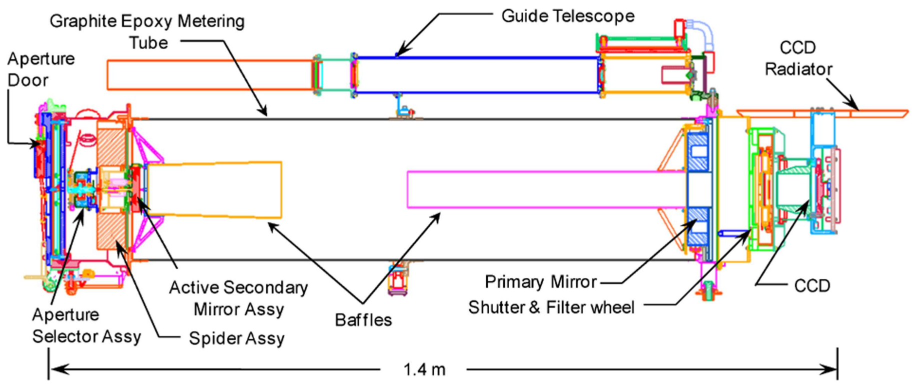

Figure 3.5: A cross sectional view of one of the AIA telescopes taken from Lemen et al. (2012).

The four AIA instruments are Casegrain telescopes adapted to observe narrow band passes in the EUV. A cross sectional view of one of the four AIA telescopes is presented in Fig. 3.5. The four telescopes are not all identical. Three of the telescopes mirrors have two different EUV band passes while the fourth one has a 171 Å band pass on one half and a broad-band UV coating on the other half. Also, each instrument has its own guide telescope, which helps to stabilize the image on the CCD (Lemen et al. 2012).

4 Application of the Multi-view B-spline Stereoscopic Reconstruction method for the analysis of two erupting prominences

In this Chapter we present the application of one of the methods described in Chapter 2, namely MBSR (Multi-view B-spline Stereoscopic Reconstruction). We have applied this method to two different events. The analysis and the results were published in two papers: “Low polarized emission from the core of coronal mass ejections” where I am a second author and “4D reconstruction of an eruptive prominence using three simultaneous view directions” where I am the first author.

For the first event which we will describe in Section 4.3, my contribution was to reconstruct the 3D coordinates of a region from the core of a CME. Initially, the polarization ratio method (see Section 4.2.4) was applied for the 3D reconstruction of the CME event. This method failed to reconstruct the CME core. Therefore the MBSR method was applied. The reconstruction was performed from two view directions. For the second event we have applied the MBSR method and we reconstruct for a given time the entire top edge of a prominence as a 3D curve. Moreover, we try to analyze in more detail the evolution of the prominence and the associated CME. In this case, we have used simultaneous data from three satellites (STEREO A, B, SDO) to perform the reconstruction.

Before presenting the applications of MBSR method, we make an overview with the previous work on 3D reconstruction of prominences and CMEs.

4.1 Previous work on 3D reconstruction of prominences

As we have already mentioned in a previous Chapter, before so-called “STEREO era” , scientists developed methods like rotation stereoscopy (Bemporad et al. 2011) from images of the same spacecraft but taken 10-20 hours apart for reconstructing the 3D shape of loops and prominences.

After STEREO was launched it become possible to use classical stereoscopy to derive the 3D structure of some parts of the entire prominence arch using data from two view directions. A method to visualize the stereo information was developed by Artzner et al. (2010). They used data from STEREO A and B in EUVI 304 Å and rotate STEREO-B images so as it would be seen from the STEREO A view direction. They then subtract one image from the other. While the surface background cancels prominences and loops will remain visible as elevated structures.

The technique developed by Gosain and Schmieder (2010) makes use of the approximation that a filament is a 2D planar plasma sheet anchored to the Sun. From the two STEREO views, they determine the prominence width and inclination with respect to the solar surface. They compared the inclination angle with previous results obtained by tie-pointing applied to the same prominence by Gosain et al. (2009). The angle difference between the two methods amounted to around 10 degrees.

4.2 Previous work on the 3D reconstruction of CMEs

It is important to understand the 3D morphology of a CME because on one hand this can be the starting point for the development of physical CME models and on the other hand knowing the morphology allows to derive the propagation direction, velocity and expansion. One reason for which it is important to determine very precisely the 3D CME shape is because CMEs can have a strong damaging effect on the spacecrafts or on the astronauts or it can produces a geomagnetic storm (see Chapter 1, Section 1.5.3) at the Earth and it can affect radio transmissions or it can damages the pipe lines.

The first attempt of a 3D reconstruction is due to Crifo et al. (1983) using the polarization ratio approach (will be presented below 4.2.4). But it turned out to be impossible to derive the precise 3D shape and propagation direction from single coronagraph images. A rough guess of the propagation direction could be obtained from the projected shape of the CME cloud (e.g halo and limb events) and from the location of the eruption site on the solar surface if this could be detected. To improve the observational constraints was one of the goals of the STEREO mission launched in 2006.

The 3D reconstruction techniques still have limitations due to the final signal to noise ratio, the limited spatial and temporal resolution and the limited number of simultaneous views (Thernisien 2011). Therefore a number of alternative methods have been developed for the three-dimensional reconstruction of coronal mass ejections based on geometric properties like forward modeling (Thernisien 2011), geometric localization (Pizzo and Biesecker 2004), mask fitting (Feng et al. 2012) or based on physical properties like polarization ratio method (Moran and Davila 2004). Stereoscopy techniques can be used to reconstruct different parts of the CME like its core or the leading edge. Some hybrid models were developed and combine two different reconstruction techniques: center of mass determination combined with tie pointing or inverse reconstruction in combination with forward modeling.

In the following, I will present some of the most common 3D reconstruction techniques for CMEs.

4.2.1 Forward Modeling

Some studies show (see e.g. Chen and Shibata (2000)) that a “croissant” - type of magnetic flux rope describes very well some observations of the three part structure of CME. Motivated by Cremades and Bothmer (2004), Thernisien et al. (2006) developed a for-

Table 4.1: Parameters of the GCS forward modelling

Name of the parameter	Description
Angular width 2 α	The opening angle between the two "legs" of the model
h	Height of the "legs "
Aspect ration k	The ratio between the minor torus radius a (Fig. 4.1) and the distance from the center of the Sun to the center of the minor torus
N_e	Electron density
ϕ, θ	Longitude and latitude of the SR
γ	Tilt angle of the SR neutral line

ward modeling technique for such flux-rope like CMEs. With their parameterized model, called the Graduated Cylindrical Shell (GCS) model, they tried to reproduce the general morphology and the electron density distribution of the leading edge of these flux-rope like CMEs. The GCS model consists of a tube-shaped body with two cones attached corresponding to the "legs" which connect the CME to the solar surface (Fig. 4.1). The

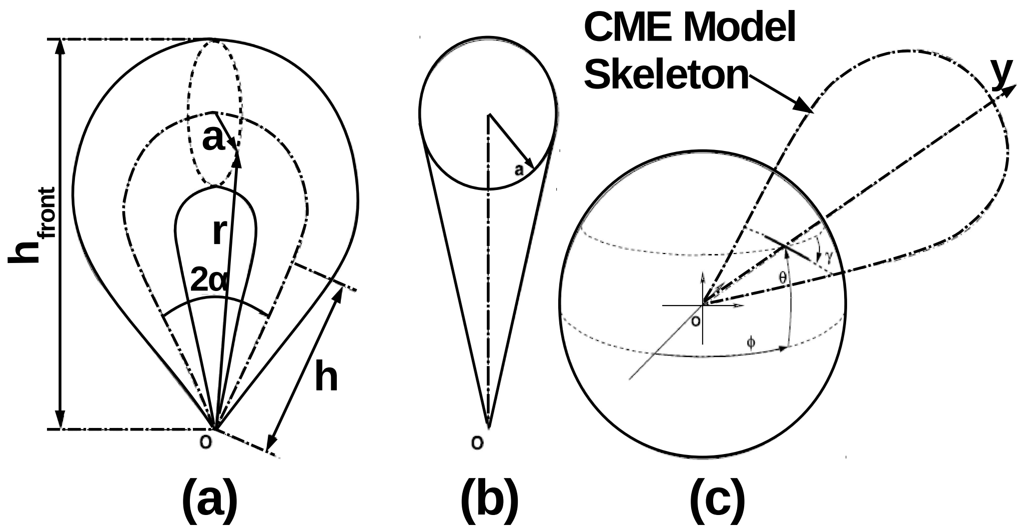

Figure 4.1: The graduated cylindrical shell model-from Thernisien (2011); The heavy line on the solar surface represents the orientation of the magnetic neutral line at the site of the CME eruption. Figure adapted from Thernisien (2011).

model has a set of parameters which can be fitted to the observed CME shape (see Table 4.1) as seen in one or more coronagraph images and to the localization and orientation of the CME source region identified in EUV images and surface magnetograms.

In order to use the parameters (see Table 4.1) which describe the GCS model the following assumptions are made: the expansion of the CME is considered to be radially along the symmetry axis of the model, the orientation of the GCS model is defined by the source tilt angle γ (see Table 4.1) and does not change during the expansion of the CME, the angular width (α) (see the Table 4.1) is assumed to depend on the length of the source region neutral line (the relation between α and neutral line is taken from a statistical study by Cremades and Bothmer (2004)).

The GCS model also predicts the electron density distribution and generates the synthetic images from a line-of-sight (LOS) integration of the Thomson scatter at the assumed density distribution. This model density distribution analytically depends on the distance from the surface of the GCS model. By comparison between real and synthetic images the model parameters can be manually adjusted in order to find the best match. Thernisien et al. (2009) extended the technique in order to allow for an automated parameter fitting if images from two view directions were used. The GCS model was applied by many authors to determine either the kinematics and expansion speed of CMEs, their flux-rope orientation and rotation either to study the 3D evolution and expansion of the CME cavity (Thernisien 2011). However, not all CMEs exhibit the symmetric flux rope shape assumed by the GCS model.

4.2.2 Geometric localization

This method was proposed by Pizzo and Biesecker (2004). For the CME reconstruction method they use two or more coronagraph images and apply geometric triangulation. Along each epipolar line in an image pair intersecting the CME they tie-point the leading and trailing edge of the CME cloud. If these four points are projected into the epipolar plane, they define a 3D quadrilateral which bounds the CME structure in the given epipolar plane. This process can be repeated for a set of epipolar planes and different image pairs. The resulting stacked 3D slices compose the bounding volume of the entire 3D CME structure (see Fig. 4.2).

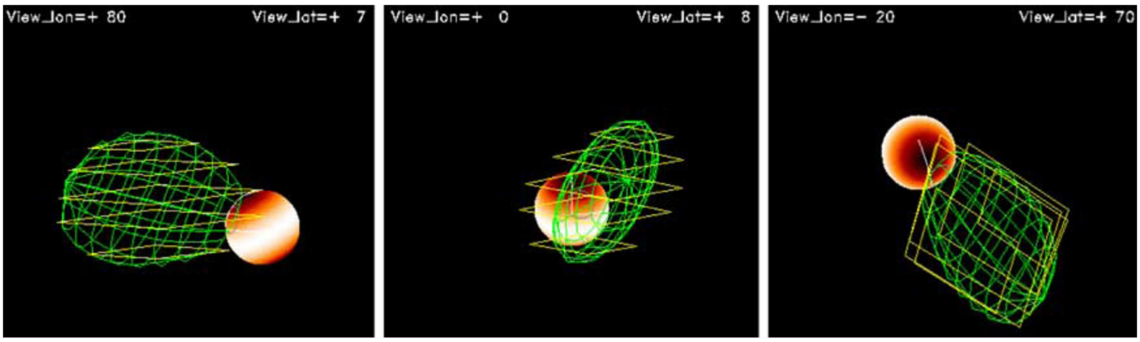

Figure 4.2: The 3D reconstructed CME with geometric localization method; Fig. reproduced from Pizzo and Biesecker (2004).

4.2.3 Mask fitting

The mask fitting method developed by Feng et al. (2012) is similar to the geometric localization technique but without the need to use epipolar planes explicitly. The 3D bounding volume of multiple slices is constructed in a reverse way. As a first step, the boundaries of the CME are defined in each image used for the reconstruction (masks). In the next step, a dense, rectangular grid is defined in the corona around the Sun. Each 3D grid point of this mesh is projected onto the images. If the projection hits the mask in all of the images the grid point may lie inside the CME and is marked. If it fails to hit only one image mask, it is definitively outside of the CME cloud. This way the marked grid points create a 3D convex polygonal volume which contains the CME (see Fig. 4.3). In a final step, the edges and corners of the 3D polygon are smoothed. The method can be easily extended to multiple view directions.

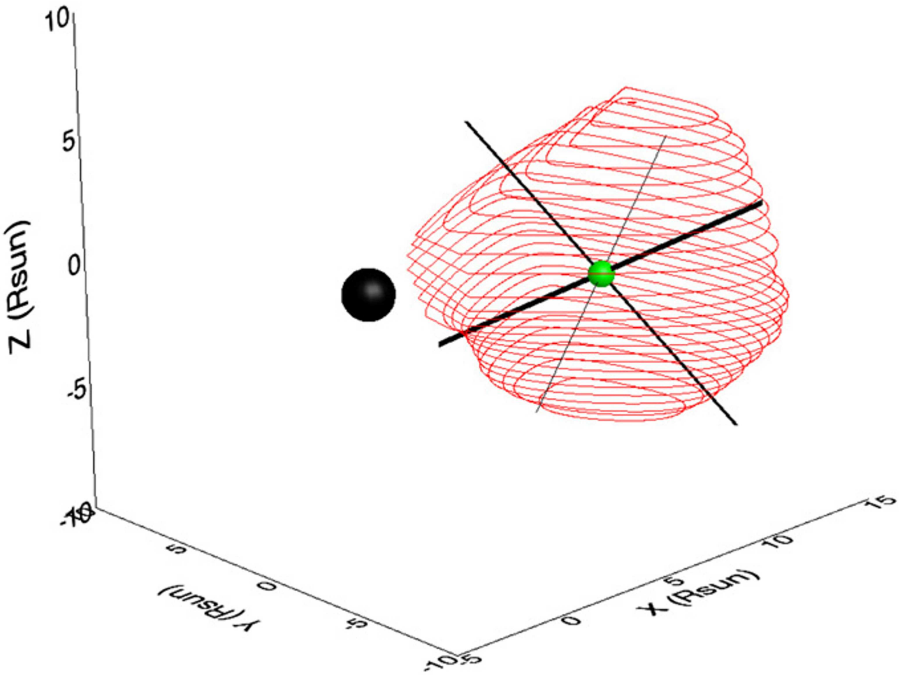

Figure 4.3: The 3D reconstructed CME with mask fitting method; Fig. reproduced from Feng et al. (2012).

4.2.4 Polarization ratio

This method is based on the polarization properties of Thomson scattering (Crifo et al. 1983, Moran and Davila 2004). It makes use of the fact that the polarization of light scattered at a free electron depends on the scattering angle χ. A sketch with the geometry of the scattering process is presented in Fig. 4.4.

For coronal observations the polarized intensity is usually separated into the tangential (I_t, i.e., parallel to the limb) and the radial (I_r, from Sun center) components. According to the Billings (1966) formula these two components can be written in terms of the local electron density N_e and the incident light intensity I_0 from the Sun as:

$$I_t = I_0 \frac{N_e \pi \sigma}{2} [(1-u)C + uD] , \tag{4.1}$$

$$I_t - I_r = I_0 \frac{N_e \pi \sigma}{2} sin^2\chi [(1-u)A + uB] , \tag{4.2}$$

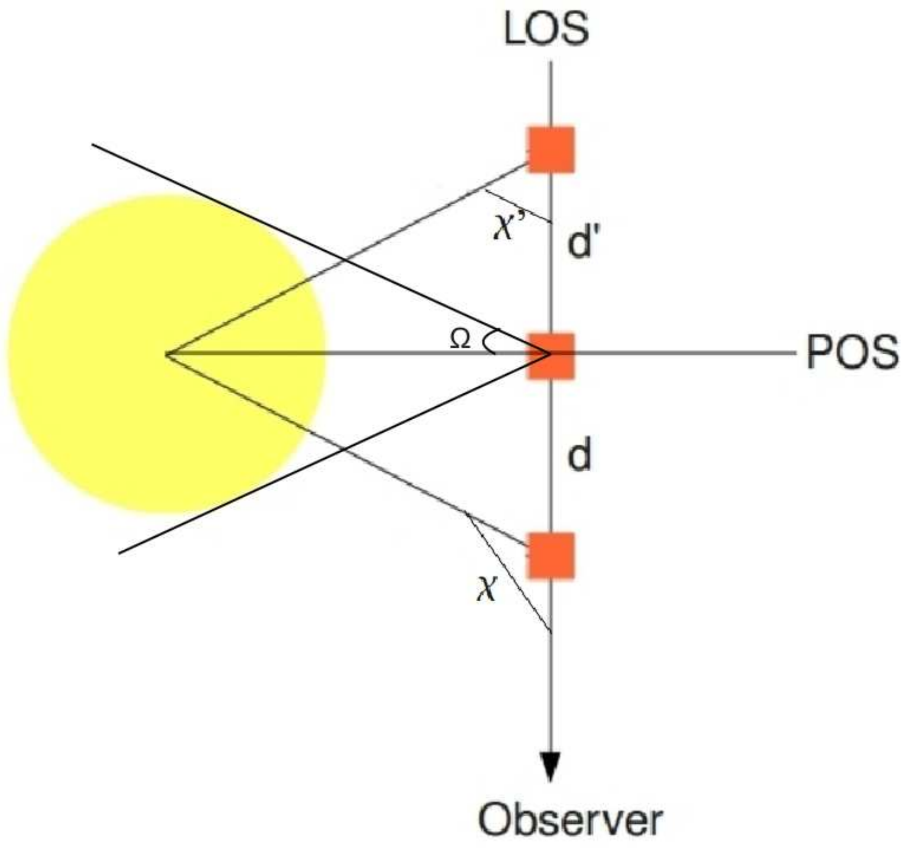

Figure 4.4: A sketch with the Thomson scattering geometry.

where σ is the Thomson scattering cross section, u is the limb darkening coefficient and $A,\ B,\ C,\ D$ are functions of the local geometry depending on the angle Ω (see Fig. 4.4):

$$A = \cos\Omega\sin^2\Omega\,, \tag{4.3}$$

$$B = -\frac{1}{8}\left[1 - 3\sin^2\Omega - \frac{\cos^2\Omega}{\sin\Omega}(1 + 3\sin^2\Omega)\ln\frac{1+\sin\Omega}{\cos\Omega}\right]\,, \tag{4.4}$$

$$C = \frac{4}{3} - \cos\Omega - \frac{\cos^3\Omega}{3}\,, \tag{4.5}$$

$$D = \frac{1}{8}\left[5 + \sin^2\Omega - \frac{\cos^2\Omega}{\sin\Omega}(5 - \sin^2\Omega)\ln\frac{1+\sin\Omega}{\cos\Omega}\right]\,. \tag{4.6}$$

From the two scattered intensity components I_t and I_r, we define the polarized brightness $I_p = I_t - I_r$, total brightness $I_T = I_t + I_r$ and unpolarized brightness $I_u = I_T - I_p$. Since the radial and tangential directions depend on the position in the coronagraph image, a coronagraph typically measures three polarized images at three different angles, respectively $-60°$, $0°$ and $60°$. From this set of 2D images, after appropriate background subtraction, one can compute total brightness, polarized and unpolarized brightness images from:

$$I_p = \frac{4}{3}\sqrt{[(I_0 + I_{60} + I_{-60})^2 - 3(I_0 I_{60} + I_0 I_{-60} + I_{60} I_{-60})]}\,,$$

$$I_T = \frac{2}{3}(I_0 + I_{60} + I_{-60}) \; .$$

Through their dependence on I_t and I_r, the polarized and total brightness and their ratio $r = I_p/I_T$ depend on the scattering angle. If the observed radiation was scattered from a single volume element, the ratio of polarized to unpolarized brightness $r_m = I_p/I_u$ would uniquely yield the magnitude of the angle χ and therefore the depth d from the plane of sky (POS) of the scattering element. But because the dependence of I_p with $\sin\chi$ is quadratic, the method cannot decide whether the scattering element is in the front or behind the POS. In real observations, I_t and I_r result from scattering along LOS instead from a single volume element. We therefore have to replace, e.g., in Eq. (4.1)

$$N_e \sin^2\chi[(1-u)A + uB] \rightarrow \int_{LOS} N_e(l)\sin^2\chi(l)[(1-u)A(l) + uB(l)]dl \qquad (4.7)$$
$$\approx \int N_e(l)dl \sin^2 <\chi> [(1-u) <A> +u <B>] \; ,$$

where $\int N_e(l)dl$ is the column density and $<\chi>$, $<A>$, $<B>$ suitable averages over the LOS. Since for a given distance of the LOS from the Sun, A and B depend through Ω also on χ, the factor of the column density could be expressed entirely as a function of $<\chi>$.

For each pixel from the 2D images, we can calculate the measured ratio r_m. This measured ratio is independent of the column density but only depends monotonically on $<|\chi|>$. The original method by Moran and Davila (2004) requires only one image, however, we are left with the ambiguity of the sign of $<|\chi|>$, i.e., of d. This can be constrained if two images are used. Still, since the method returns only a single depth estimate per pixel, it does not really return the 3D CME cloud, but rather yields a CME plane more or less close to the central longitude of the CME cloud.

4.2.5 Stereoscopy

The most common parts of the coronal mass ejections used for stereoscopic reconstruction are the leading edge (Liewer et al. 2011) or just its point of largest distance from the solar center, bright parts of the core (see e.g. Joshi and Srivastava (2011a)) or the cloud's center of mass. Howard and Tappin (2008) used this method to obtain the 3D position of a central, north and south flank of the leading edge. The reconstructed leading edge of the CME outer surface strongly depends on the view geometry and most often does not even lie on the CME surface. The visible leading edge is the projection of the outer surface forming the CME hull. For two viewpoints, the curve resulting from a stereoscopic reconstruction of the two visible leading edges approximates the intersection of the CME hull with a plane normal to the mission plane of the two observing space craft (see Fig. 4.5). Liewer et al. (2011) analyzed the position of the tie-point reconstruction relative to the CME surface. Because the two spacecraft involved in the reconstruction see different parts as the leading edge the tie-point reconstruction yields a curve somewhere above the CME surface. Depending on the curvature of the CME surface, the reconstructed leading edge lies about $R\left[1/\cos\left(\frac{\pi-\gamma}{2}\right)\right]$ of the real surface where R is the local curvature radius of the CME surface in the mission plane of the observing space craft.

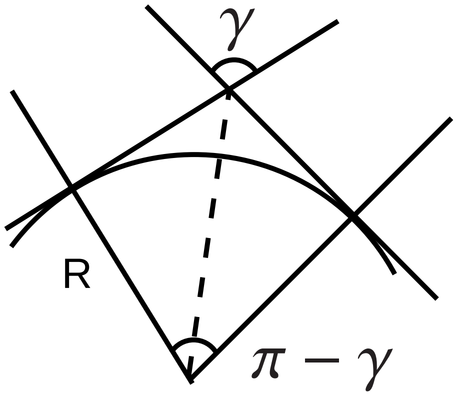

Figure 4.5: A sketch with the geometry of the intersection point between the two visible leading edges of the two view points.

Moreover, if the CME surface changes its shape and curvature with time, each edge curve of a time sequence of such leading edge reconstructions may well represent different parts of the CME surface (Chifu et al. 2012).

4.2.6 Local correlation tracking plus tie-pointing

For an automatic determination of correspondences between two images, Mierla et al. (2009) used a correlation-based approach. The normalized correlation between the intensity variation from two subimages, one from each image, is calculated for various positions of the sub-images along the same epipolar line. When the correlation coefficient assumes a maximum at a certain pair of positions above a predefined threshold, the two image positions are used to determine an equivalent 3D scattering center. Processing the entire CME region of both images this way, a cloud of scattering centers results which are assumed to outline the CME interior area. The method has been reported to work well if the angle between the view directions is small and local correlations can be expected to be large. In this case, local 3D density variations in the CME cloud may lead to large normalized correlation coefficients for subimages centered on the correct positions. The performance was found to be reduced as the angle between the view directions increased. The normalized correlation coefficient is defined as

$$\sigma_{AB}(x, x', y) = \frac{\int_W I_A(x+\xi, y+\zeta) I_B(x'+\xi, y+\zeta) d\xi d\zeta}{\sqrt{\int_W I_A^2(x+\xi, y+\zeta) d\xi d\zeta \int_W I_B^2(x'+\xi, y+\zeta) d\xi d\zeta}}, \tag{4.8}$$

where $\sigma_{AB}(x, x', y)$ varies between the limits [-1,1]; $I_A(x, y)$, $I_B(x', y)$ are the total brightness intensities of the two images; at image positions, x, y and x', y', respectively, in the epipolar coordinate frame, i.e., y is the common epipolar coordinate and x, x' are positions along the epipolar line y. The integral $\int_W$ is executed only over a small subimage W.

4.2.7 Hybrid methods

Constraint on the mass calculation and tie-pointing

To find a fast estimate of the 3D CME propagation direction and velocity, one can determine the center of mass of the CME cloud. Since in coronagraph white-light images, the brightness is more or less proportional to the column density along the LOS (the differential Thomson scattering cross section varies only little with scattering angle), the projection of the center of mass is just the barycenter of the image brightness. From these projections, the approximate 3D center is easily determined via stereoscopy. Mierla et al. (2009) and Mierla et al. (2010) have calculated the center of mass of seven CMEs and derived their latitude, longitude and distance from Sun. Under these assumptions, the total mass of the CME as calculated from Billing's equations (see Eqs. (4.1) - (4.6)) should be the same except for contributions close to the occulter which could not be equally visible from both view directions. Colaninno and Vourlidas (2009) obtained different values for the mass of the same CME from the two views of the STEREO spacecraft. They explained the discrepancy by the small but not negligible scattering angle dependence of the Thomson scattering.

Inverse reconstruction plus forward modelling

Using a hybrid model, Antunes et al. (2009) reconstruct the bulk of the CME excluding the leading edge and shock analyzing running difference images. For their hybrid model data from at least two view directions of the CME are required. Within this method the authors tried to obtain the geometric shape and also the density of the CME. As a first step in their reconstruction, they use the forward modeling technique to roughly fit the CME shape. The fitted shape is used as an envelope of the CME for the second part of the reconstruction in which they try to fit the density variation to match the image brightness only inside the CME envelope. It should be noted that for two images, the 3D density distribution obtained is not unique.

4.3 3D reconstruction of a CME core

4.3.1 Introduction

As mentioned in Chapter 1, the coronal mass ejections are often observed to have a three parts structure: a leading outer edge followed by a dark cavity and a bright core. Even though a one to one correlation does not exist, the observations have shown that in many cases prominence eruptions are the source of coronal mass ejections. In these cases, the cold ($T \sim 10^4$ K) and dense ($N_e \simeq 10^{10}$ cm^{-3}) material of the erupted prominence is associated with the core of the CME. Poland and Munro (1976) observed Hα emission in the core of a CME cloud which had a prominence eruption as its source. They have shown that the Hα emission is much less polarized than the emission from the surrounding material which is due to Thomson scattering at the free coronal electrons. They used ground based observations in Hα and He II for the prominence analysis and coronagraph data on board the Skylab spacecraft for the white light observations of the outer corona. Because the polarization in the core of the CME had a value two times smaller than expected they concluded that the emission was not entirely produced by Thomson scattering and that Hα scattering made some contribution to the scattered light.

We have studied a CME event on 31 August 2007 which shows a bright patch of low polarized radiation in its core which was presumably caused by a Hα resonant scattering.

Hα emission occurs when the hydrogen electron relaxes from the third (n = 3) to the second (n = 2) energy level. The wavelength of the Hα radiation is 656.28 nm. The probability of the electron to decay from the energy level n=3 to n=2 and to excite Hα emission is higher after ionization of the hydrogen followed by a recombination rather than by a direct excitation to level n=3. The ionization energy from the ground level is 13.6 eV and the energy which an electron needs to be excited from the ground level to the third atomic level is 12.1 eV. The ionization state of a plasma in thermodynamic equilibrium is dependent on the density and temperature and it can be obtained from the Saha equation

$$\frac{N_{j+1}}{N_j} = \frac{2Z_{j+1}}{n_e Z_j}\left(\frac{2\pi m_e K_B T}{h^2}\right)^{3/2} e^{-\chi_j/K_B T} , \tag{4.9}$$

where N_{j+1}, N_j are the number density of the ions, Z is the atomic number, m_e is the electron mass, h is the Planck constant, K_B is Boltzmann's constant, T is the temperature of the plasma, χ_j is the ionization energy.

If we consider $x = N_{H_{II}}/N_H$ the ratio of the number of ionized hydrogen ($N_{H_{II}}$) to total number density of hydrogen atoms ($N_H = N_{H_I} + N_{H_{II}}$) and we know that for hydrogen $n_e = N_{H_{II}}$, the Saha equation becomes

$$\frac{x^2}{1-x} = \frac{2}{N_H}\left(\frac{2\pi m_e K_B T}{h^2}\right)^{3/2} e^{-13.6/K_B T} . \tag{4.10}$$

For a temperature of $T = 10000$ K almost the entire hydrogen is ionized. At equilibrium, the radiative recombination rate of hydrogen per unit volume is given by (Hasted 1964):

$$r_r = n_e \cdot n_p \cdot \alpha_A(T) \simeq n_e^2 \cdot \alpha_A(T) , \tag{4.11}$$

where n_e, n_p are the number density of electrons, respectively protons and $\alpha_A = 4.2 \cdot 10^{-13}$ cm^3 s^{-1} is the radiative recombination coefficient for a temperature $T = 10000$ K. For a number density of the order of 10^8 cm^{-3}, the recombination rate is $r_r = 4.2 \cdot 10^3$cm^{-3} s^{-1}. After recombination, the captured electron may occupy any energy level and by means of a further relaxation process, Hα radiation can be produced.

4.3.2 Observations

On 31 August 2007, the STEREO telescopes observed the eruption of a prominence which triggered a CME with an interior void and a bright concentrated core. The separation angle at 31 August 2007 between the two spacecraft, STEREO A and B, was 28 degrees (see Fig. 4.6).

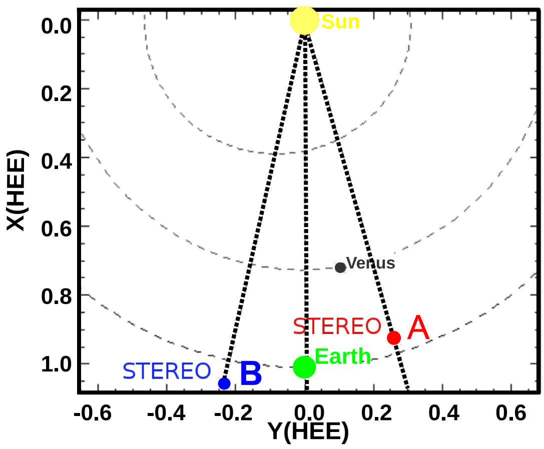

Figure 4.6: The position of the two STEREO spacecraft A and B on 31 August 2007 (adapted from http://stereo-ssc.nascom.nasa.gov/where.shtml).

For the analysis of the polarization degree from the CME plasma, we used observations from the COR1 telescope. The coronagraph COR1 observes the solar corona in white light in a 22.5 nm wide wavelength band centered at the Hα line at 656 nm (Thompson et al. 2010). It also has a linear polarizer which records images at three different polarization angles: 0, 120, 240 degrees (see Chapter 3). As explained in Section 4.2.4, from these 2D data one can obtain the polarized brightness (pB), total brightness (tB) and unpolarized brightness (uB) for each pixel. For three parts structured CMEs, as observed on 31 August 2007, the core material can sometimes be traced back to a pre-eruption prominence CME. For the CME from 31 August 2007, we can clearly identify the source prominence in the EUV images. Therefore, we can trace the prominence eruption with the help of EUVI instrument on board STEREO from its earliest stages on. The He II line at 304 Å provides a good visualization of the prominence and we have used the according image data for the identification of the prominence source. At later stages of the eruption, the dense prominence material evolved into the CME core material. The observations in EUVI 304 Å show the prominence from 31 August 2007 starting to rise at around 19:00 UT, the associated CME enters the COR1 field of view at 21:00 UT. The simultaneous observations from the EUVI and the COR1 instrument (see Fig. 4.7) show that the prominence is co-spatial with the CME core.

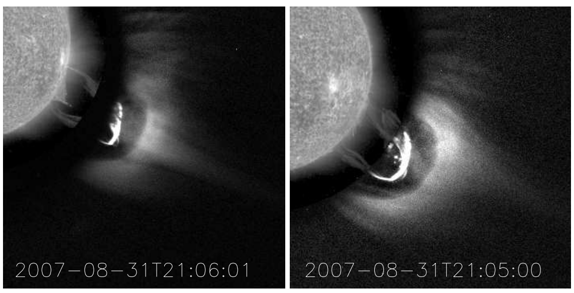

Figure 4.7: Composite images on 31 August 2007, 21:05 UT from EUVI 304 Å and COR1 onboard STEREO A (right image) and STERO B (left image) taken from Mierla et al. (2011)

This indicates that the prominence material is the source of the CME core (see Fig. 4.7).

4.3.3 Data analysis

The separation angle between the two STEREO spacecraft allows us to perform a 3D stereoscopic reconstruction with the MBSR method. For the analysis of the low polarization patch observed on 31 August 2007 in the core of the CME we used data from COR1 at 21:30 UT. In a first step the data was processed with secchi_prep.pro, an IDL (Interactive Data Language) program provided by the solarsoft package, which calibrates the raw images (divides by exposure duration, subtracts the CCD bias, converts the image intensities from the recorded digital units to fractions of the mean solar brightness and applies a flat-field correction). In order to remove the coronal streamers from the image, we subtract a background image from each of the total and polarized brightness images. The background images were obtained by extracting for each pixel the minimum intensity from all images over a 12 hours interval, centered at the time of the eruption. In addition, a median filter was applied to the resulting background image in order to reduce the noise. Fig. 4.8 shows on a logarithmic scale the total brightness COR1 images from STEREO A and B after the background was subtracted. This procedure was applied to all three polar-

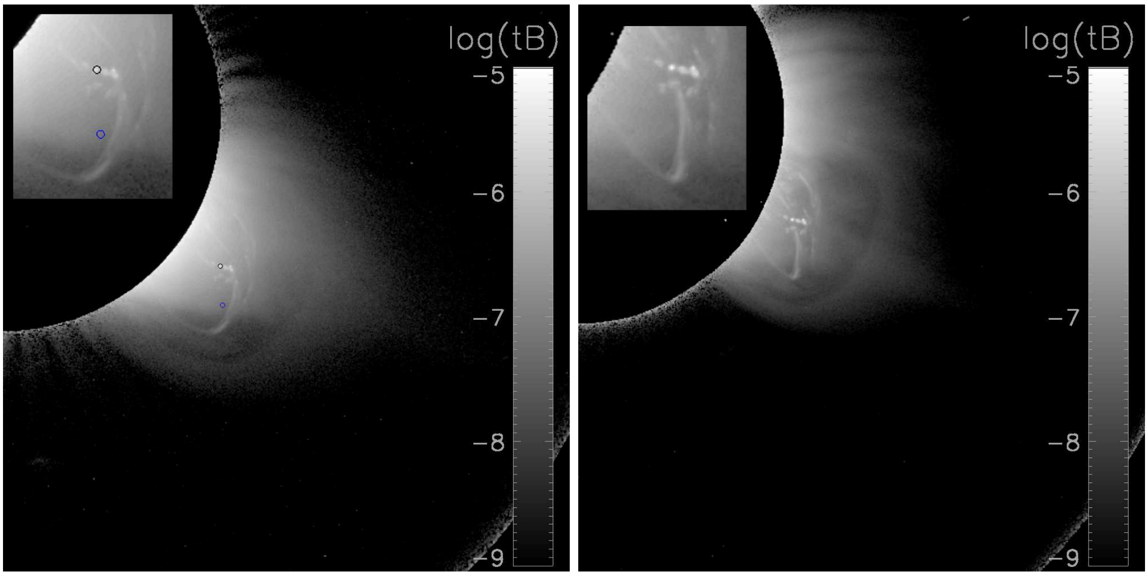

Figure 4.8: The total brightness images expressed in mean solar brightness from COR1 of STEREO spacecraft A (left panel) and B (right panel) at 21:30 UT. The upper left inserts are zooms of the CME core region from the same perspective.

ization orientations so that polarized and unpolarized brightness could be computed. Fig. 4.9 shows the ratio of the polarized to unpolarized brightness obtained from the STEREO A and B images. The ratio images are color coded and we can see the low polarization patches (red) at about 1.5 $R_\odot$ distance from the Sun center inside the highly polarized CME emission (gray) bulb. In the upper left corner we show a magnification of the region with the low polarization patch.

One method proposed to derive the 3D CME shape is the polarization ratio method (see

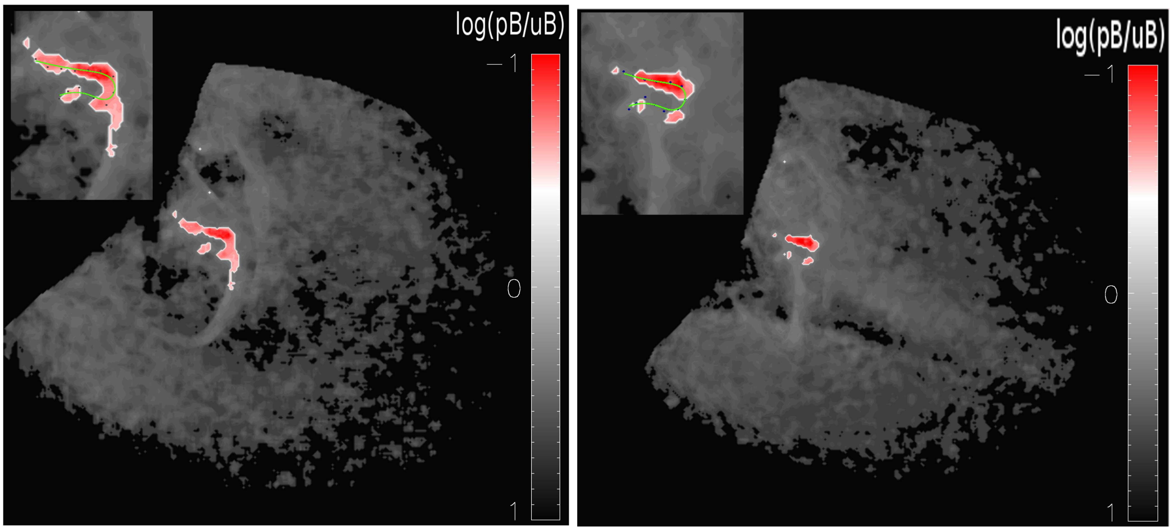

Figure 4.9: The ratio pB/uB of polarized to unpolarized light from COR1 of STEREO spacecraft A (left panel) and B (right panel). The upper left inserts are zooms of this region from the same perspective. The green line represents the projection of the 3D curve fit to the patches location obtained from stereoscopic triangulation.

Chapter 4.2.4 for the description of the method). To recall, for Thomson scattering, the ratio pB/uB is a function of the scattering angle between the incident light and the direction towards the observer (see Fig. 4.4). With this information, we can estimate the distance of the scatterer from the plane of the sky. From a single ratio observation alone, we can however not decide whether the scatterer is in front or behind the POS. This ambiguity can be resolved with observations from two view directions as they are provided by STEREO A and B. For each pixel in an image from STEREO A and B, respectively, we obtain an estimate for the distance of the scatterer from the respective plane-of-sky (POS). From the two positions on other side of the POS we choose the one which yields a scattering center close to the scatterers derived from the other view direction.

The resulting 3D distribution of scattering centers is displayed in Fig. 4.10. In the image, the view direction is from above the Sun's north pole onto the STEREO mission plane. The green dots represent the 3D position estimates derived from the pixels of the COR1/STEREO A image, the blue dots are the equivalent from COR1/STEREO B. The best agreement between the point-clouds from STEREO A and B was achieved if the CME scattering center was assumed in front of the POS for STEREO A and behind the POS for STEREO B. Since the derived scattering centre positions represent some weighted mean along the respective line-of-sight, the azimuthal extent of the cloud of scattering centres in Fig. 4.10 probably represents a lower bound of the true azimuthal extent of the CME cloud. Ideally, the scattering centers are all close to the meridional barycentre plane of the CME cloud.
The features which do not match in this picture are the elongated structures which we will term the “horns ”. They have their origin in the low polarized patches observed in the COR1 A and B images (see Fig. 4.9). For a Thomson scattering volume element, a low polarized scattering polarization implies a location far away from the POS of the observer. Since the horns can obviously not be matched by whatever choice for the po-

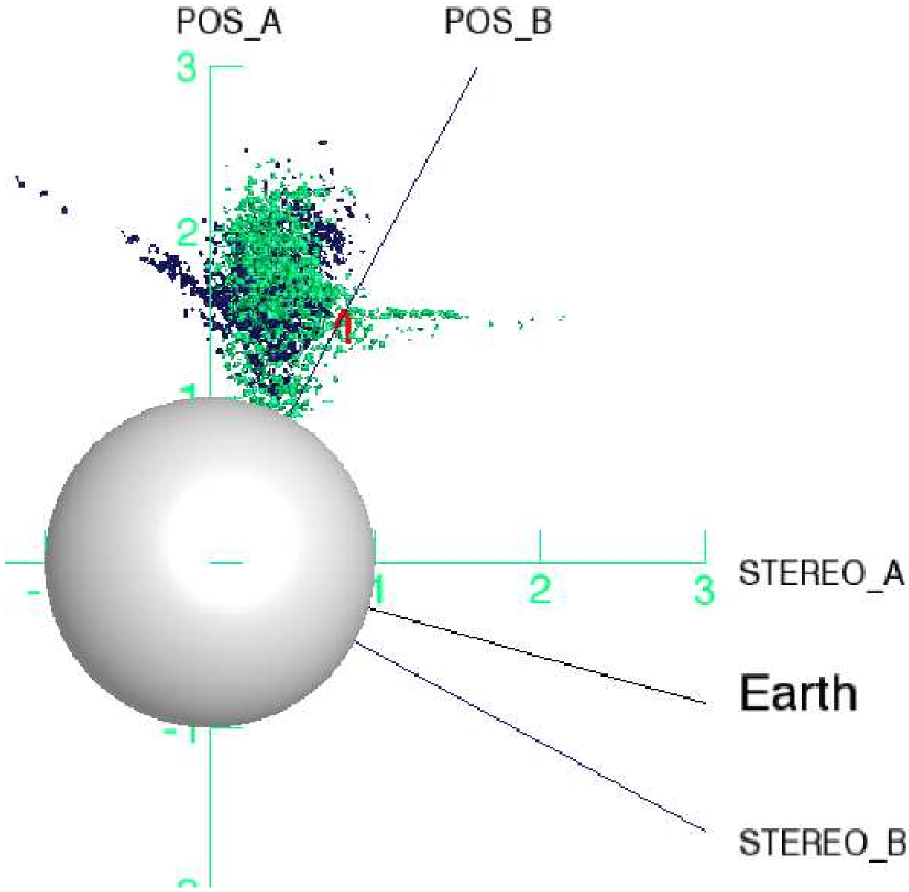

Figure 4.10: PR reconstruction of the barycenter plane of the CME on 31 August 2007, 21:30 UT. The green/blue points are the reconstructed Thomson scattering positions from COR1/STEREO A and B, respectively. The short red curve inside the cloud represents the reconstruction by triangulation of the region where low polarization patches are observed. The view is from above the STEREO mission plane (STPLN). The axes in the STPLN are the directions to the spacecraft (labeled STEREO A and B) and their respective plane of the sky (POS A and B). The black line is the projected direction to Earth. Image taken from Mierla et al. (2011).

larization ratio method ambiguity, we conclude that the respective image signals were not produced by Thomson scattering.

Since the polarization ratio method obviously fails to determine the position of the bright core patch, we used the stereoscopic reconstruction method (MBSR) to find its position. A detailed description of the method is presented in Chapter 2, Section 2.3. The separation angle between the spacecraft A and B of 28 degrees allows to easily identify and tie-point corresponding features in both images. However, the geometrical errors are considerable for such a small separation angle. The COR1 total brightness images allow us to identify and reconstruct a 3D curve on an approximately principal axis along which the core material is distributed. The reconstructed 3D curve and the respective reconstruction errors are displayed in the Fig. 4.11. The projection of this curve on the spacecraft view direction curve is overplotted in green on the polarization ratio images of COR1 A and B

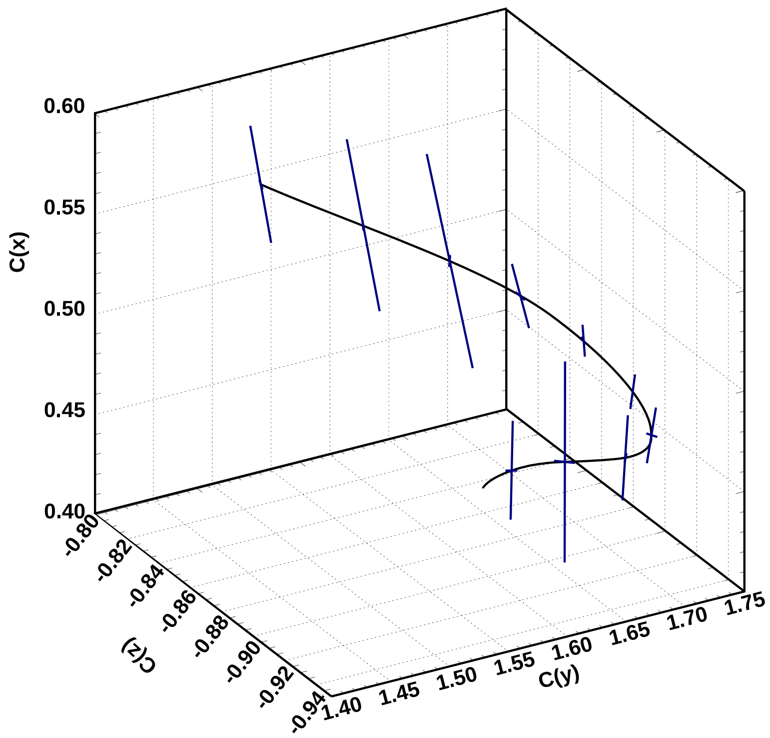

Figure 4.11: Stereoscopically reconstructed curve with the vertical errors.

in Fig. 4.9. The blue dots represent the tie-points used for the 3D reconstruction. In Fig. 4.10 the curve is overplotted in red onto the scattering centres from the polarization ratio method. From the Fig. 4.10 we can observe that the 3D patch is positioned close to the barycenter plane of the CME. In Fig. 4.11 we show the reconstructed 3D curve enlarged. The material of the bright core patch should be distributed more or less along this curve with the error range indicated by the blue bars attached to the curve.

4.3.4 Discussion

Low polarization of the sun light scattered in the corona can be due to a number of reasons. For example, by scattering at coronal dust particles which results in the so-called F-corona (Morgan and Habbal 2007). With the exception of the dust tails of the Sun-gazing comets, this F-corona scattering changes only very slowly in time, typically by months. In our analysis, therefore the contribution from the F-corona has largely been removed by the background subtraction of the primary image data. Another reason for a low polarization signal can be a position of a Thomson scatterer far away from the POS. This assumption, however, is in disagreement with the 3D stereoscopic reconstruction of the low polarized patch. The most probable explanation is that the emission from the core of the CME is due to Hα resonant scattering (Poland and Munro 1976). In the case of CMEs produced by prominence eruptions, the core material of the CME is usually associated with the prominence material which is cooler and denser than the coronal plasma.

In presence of a core patch each pixel of a 2D coronagraph image records the LOS integration of the totally scattered emission; the contributions from Thomson scattering and Hα resonance scattering are superposed. Fig. 4.12 sketches how different scattering sources may integrate up in different areas of a coronagraph image. Along a view direction

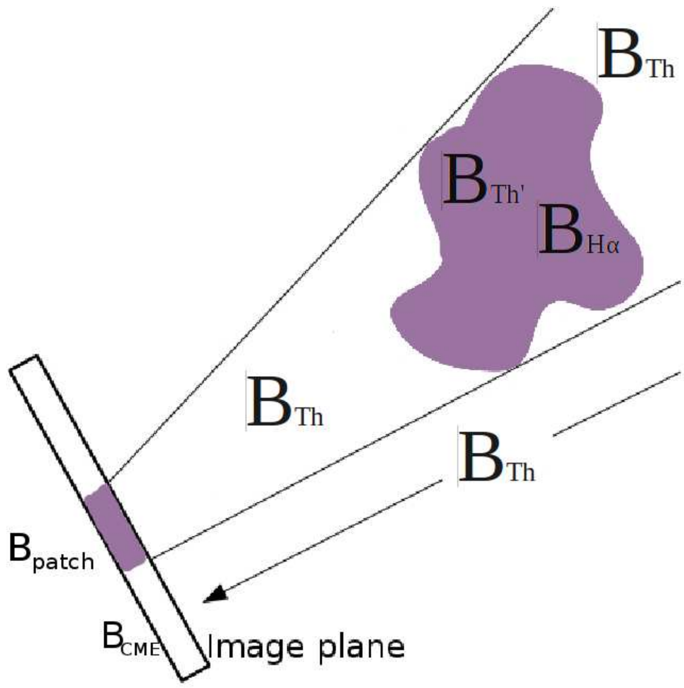

Figure 4.12: Sketch with the contribution of the radiation recorded by a coronagraph on the image plane

which does not intersect the patch, we only have Thomson scatter contributions which integrate to a brightness B_{CME} of the CME cloud. In contrast, the observed brightness B_{patch} in projection of the patch is a superposition of three contributions from along the LOS: the resonance scattering $B_{H\alpha}$ plus the Thomson scatter $B_{Th'}$ from inside the patch and the Thomson scatter from B_{Th} outside the patch. Note that scatter contribution $B_{Th'}$ may differ from B_{Th} because the plasma density inside the patch is strongly enhanced compared to the average CME cloud density. On the other hand, the contribution of B_{Th} to B_{patch} is approximately the same as to B_{CME}. We therefore observe the following brightness in the coronagraph inside the projection of the core patch:

$$tB_{\mathrm{patch}} = tB_{\mathrm{H}\alpha} + tB_{\mathrm{Th'}} + tB_{\mathrm{Th}} \,, \tag{4.12}$$

$$pB_{\mathrm{patch}} = pB_{\mathrm{H}\alpha} + pB_{\mathrm{Th'}} + pB_{\mathrm{Th}} \,. \tag{4.13}$$

From the total brightness data, we have found that the value of the total brightness of the Hα patch is about 10 times higher than that of the surrounding Thomson scattering cloud, $tB_{\mathrm{patch}} \simeq 10\ tB_{CME} = 10\ tB_{Th}$ (in the Fig. 4.8, inside the black circle $log(tB_{patch}) = -6.93$ and inside the blue circle $log(tB_{CME}) = -7.90$). From the observations of tB_{CME} and using Billings (Billings 1966) formulas we are able to estimate the electron density in the CME. For an assumed depth along the LOS of 1 $R_\odot$ we derive a density n_e of $2.6 \cdot 10^6$ cm^{-3}. From the computed polarization ratio we find a ratio of the polarized to the total brightness:

$$r = \frac{pB}{tB} = \frac{\frac{pB}{uB}}{1 + \frac{pB}{uB}} \simeq \begin{cases} 0.5 & = r_{\mathrm{Th}} \text{ for a typical LOS through the CME} \\ 0.1 & = r_{\mathrm{patch}} \text{ for a LOS through the bright core patch} \end{cases}$$

The two values approximately reflect the contrast in the polarization ratio in Fig. 4.9.

For Thomson scattering, $r_{\mathrm{Th}} = pB_{Th}/uB_{Th}$ should depend only on the distance from the solar surface, hence we can assume $r_{\mathrm{Th}} \simeq r_{\mathrm{Th'}} = pB_{Th'}/uB_{Th'}$, i.e. the same polarization ratio inside and outside the patch. Obviously, $tB_{\mathrm{H}\alpha}$ must be significant in Eq. (4.12) over the Thompson scatter contribution since r_{patch} differs considerably from r_{Th}. Inserting the observed total brightness and polarization ratios into Eqs. (4.12) and (4.13) and eliminating tB_{Th}, we obtain the following relation:

$$\frac{tB_{\mathrm{H}\alpha}}{tB_{\mathrm{Th'}}} = \frac{8}{1 - 18\, r_{\mathrm{H}\alpha}} \, .$$

Hence from the brightness and polarization ratios, $r_{\mathrm{H}\alpha}$ cannot be larger than 1/18. This low value of the intrinsic Hα polarization ratio agrees with low values obtained for chromospheric measurements (**?**Wiehr and Bianda 2003). Moreover, the ratio $tB_{\mathrm{H}\alpha}/tB_{Th'}$ cannot be smaller than 8. Hence a large fraction of the radiation from the core patch should be Hα emission (Mierla et al. 2011).

Jejčič and Heinzel (2009) used 1D isothermal-isobaric models to derive an electron density diagnostic for quiescent prominences. They have considered different temperatures, pressures and geometrical thicknesses for each model. In the white light emission, they assumed a waveband of 10 nm and a geometrical dilution factor of $W = 0.416$ which corresponds to an altitude of 10000 km. The geometrical dilution factor has a dependence of height z above the solar surface as :

$$W(z) = 1 - \sqrt{1 - \frac{R_\odot^2}{(R_\odot + z)^2}} \, . \tag{4.14}$$

For the time when we have applied the polarization ratio method, the core of the CME was at an altitude of 1.68 $R_\odot$. At this hight we obtain a dilution factor $W(z) = 0.35$.

Jejčič and Heinzel (2009) derived an equilibrium relation between the electron density n_e and the ratio between Hα resonant scattering and Thomson scattering. For typical prominence temperatures in the interval from 4300 K to 15000 K this ratio has a weak dependence with the temperature:

$$\frac{E_{H\alpha}}{E_{WL}} = 1.64 b_3 W 10^{-4} T^{-3/2} e^{17534\mathrm{K}/T} \frac{n_e}{\mathrm{cm}^{-3}} \, . \tag{4.15}$$

Here T is the temperature and b_3 is the LTE departure coefficient of the $n = 3$ level of a hydrogen atom which is defined as the ratio of the actual population in the j level to the theoretically expected population in LTE ($b_j = (n_j/n_\infty)/(n_j/n_\infty)_{LTE}$) (Gouttebroze et al. 1993).

From our observations, $tB_{\mathrm{H}\alpha}/tB_{\mathrm{Th}} \approx 9.33$. If we consider a temperature of 10000 K for the patch material, a geometrical dilution of 0.35 and the departure factor $b_3 = 2.97$, we obtain an electron density in the H_α patch $n_e = 8 \cdot 10^8$ cm^{-3}. This is nearly three orders of magnitude of what we have estimated for the CME cloud outside of the patch (Mierla et al. 2011).

4.4 4D reconstruction of a prominence-CME from two and three views

4.4.1 Introduction

On 1 August 2010 three solar eruptions (prominences and flares) were observed at closely located source regions and expelled within hours. A detailed list of events from that day is discussed in Schrijver and Title (2011). The chain of events was called “sympathetic” eruptions by Török et al. (2011) because in observations, one can see how the eruption of one prominence destabilized the magnetic configuration of its neighboring prominence and caused it to erupt. The prominences covered the entire northern hemisphere of the Sun (Fig. 4.13) which made them a global phenomenon according to the definition of Zhukov and Veselovsky (2007).

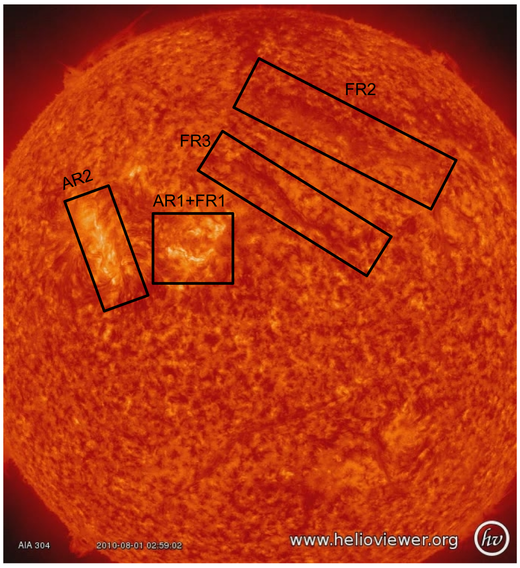

Figure 4.13: Image showing the regions where erupting events occur during 1 August 2010. AR1+FR1 represent the region where first eruption flare and filament eruption occur; FR2 stands for second prominence eruption; AR2 stands for active region where the second flare occurs; FR3 stands for the third flux rope eruption. The image was recorded in HeII 304 Å by the AIA instrument onboard SDO (www.helioviewer.org).

Fig. 4.13 was recorded in He II wavelength and shows the regions where the events occurred. Around 2:59 UT a flare followed by an active region filament eruption occurred in the area marked with AR+FR1 in Fig. 4.13. At 5:26 UT the prominence in region FR2 erupted accompanied by a flare in region AR2 (Fig. 4.13). The last erupting prominence

of this sequence started at 22:06 UT in region FR3. From this chain of three prominence eruptions we have focused on the second eruption from region FR2, which was a high latitude prominence spanning over about 55° in longitude (see Fig. 4.14). The aim was to reconstruct its kinematic evolution as closely as possible. The reconstruction errors depend on the image resolution and on the angle between the space craft.
The CME was observed as a three-part structure in white-light images. The bright core corresponds to the prominence material observed prior to the eruption in extreme ultraviolet (EUV) images.

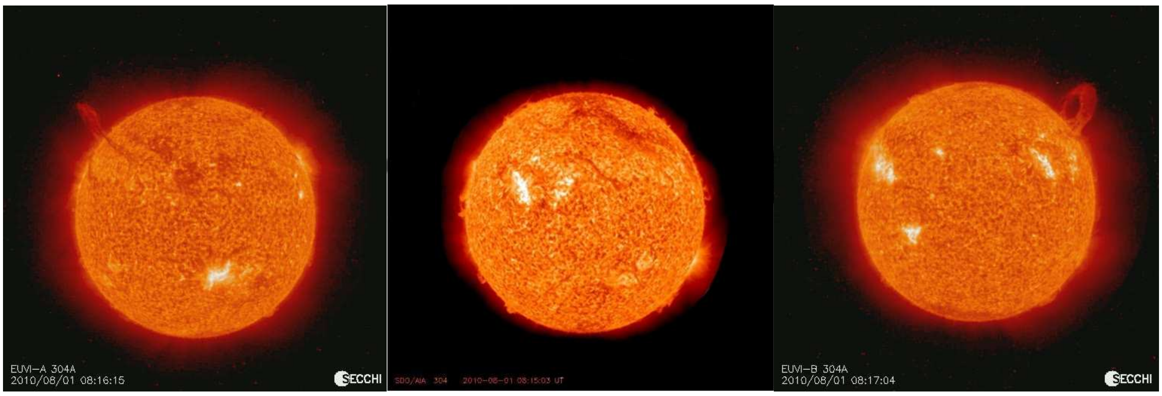

Figure 4.14: Images of the eruptive prominence taken from three different views at 8:16 UT in 304 Å wavelength; left image - STEREO B; middle image - SDO; right image - STEREO A.

This sequence of eruptions formed a spectacular event which was previously studied by Joshi and Srivastava (2011b,a), Li et al. (2011), Török et al. (2011). Using STEREO/EUVI data, Joshi and Srivastava (2011b) analyzed the position, height and acceleration of the reconstructed parts of the eruptive prominence from region FR2. From the evolution of the prominence kinematics they concluded that there were two phases of the prominence eruption. From the variations in latitude and longitude of the reconstructed features they concluded that the prominence rotates during the rising phase slightly around its propagation direction. Joshi and Srivastava (2011a) analyzed the velocity of the top point of the CME core patch and of the leading edge of the CME. They found maximum velocities of around 200 km s^{-1} for the top part of the CME core and 567 km s^{-1} for the leading edge of the CME. Li et al. (2011) reconstructed the top point of the prominence from region FR2. For the reconstruction they used data from one of the STEREO satellites and SDO satellite. The authors used the 3D reconstructions to determine the position of different parts of the prominence and derived the height, velocity and acceleration for highest part of the prominence and the projected speed of the CME front.
In terms of reconstruction, what is new in our approach is the use of data from three satellites (STEREO A, B, SDO) simultaneously. With our MBSR method explained in Chapter 2 we reconstruct for a given time the entire top edge of the prominence as a curve which can give more information about the kinematics of the prominence. Moreover, we try to analyze in more detail the evolution of the prominence and the associated CME.

4.4.2 Observational data and the 3D reconstruction

In general, 3D stereoscopy requires images of the object to be reconstructed from at least two different view directions. In this study we use three view directions employing EUV observations from STEREO and SDO and coronagraph observations from STEREO.
For the prominence studied, the reconstruction was performed from the moment of the eruption at 5:26 UT until the subsequent CME escaped the field of view of the STEREO COR1 coronagraph at 10:35 UT. We could not perform the reconstruction after 10:39 UT because the CME left the COR2 field of view of STEREO B so that only images from STEREO A remained available.
For the 3D reconstruction of the rising prominence we used the 304 Å images obtained by EUV telescopes of STEREO A, B and SDO. The EUVI field of view is limited to 1.7 $R_\odot$ (Wuelser et al. 2004) for STEREO and to 1.5 $R_\odot$ for SDO/AIA (Lemen et al. 2012). The STEREO observations are well synchronized taking into account also the travel time of light from Sun to the respective spacecraft. The SDO data corresponding to a give STEREO image pair was chosen as close in time as possible with a maximum time discrepancy of 1 minute and 12 seconds. The data sequence was selected with a 10 minutes cadence for all three spacecrafts until the prominence left the field of view of the STEREO A EUVI telescope at 9:26 UT.
After 9:26 UT, the prominence could only be traced in COR1 (inner coronagraph) and COR2 (outer coronagraph) of STEREO. We used images from COR 1 A and B with a

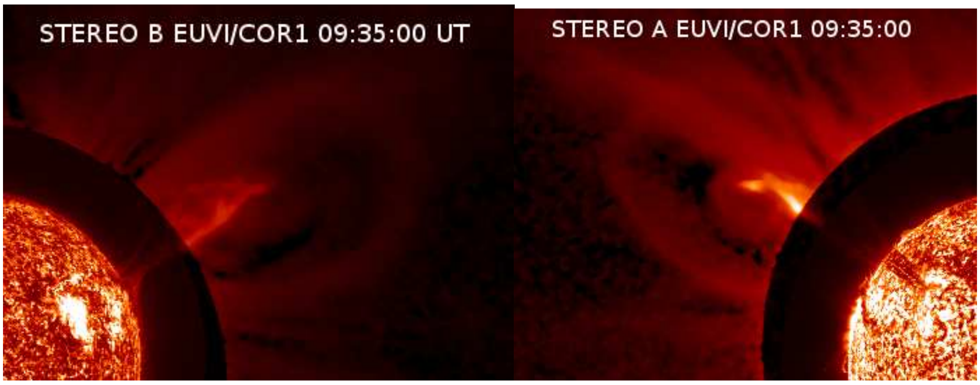

Figure 4.15: Images of the eruptive prominence taken from STEREO B (left side) and STEREO A (right side) at 9:35 UT.

5 minutes cadence to determine the 3D position of the core and the leading edge of the CME produced by the prominence. A composite image of the rising prominence and of the CME is presented in Fig. 4.15. On the 1 August 2010, the separation angle between the two STEREO spacecrafts was 149.55°; between STEREO A and SDO, the separation angle was 78.39° and between STEREO B and SDO, 71.16°. This means that SDO was located approximately in the center between the STEREO spacecraft and limb events on STEREO were seen close to the disk center in SDO. At these separation angles we perform the reconstruction from two views and also from three views simultaneously.
The 3D reconstructions for the prominence and the associated CME were performed using MBSR (Multi-view B-spline Stereoscopic Reconstruction) described in Chapter 2. For all structures investigated, we always tie-point their visible upper edge. We choose

not to follow very small scale structures of the filament of the size of a few pixels because they are highly variable and difficult to trace in time. Both the prominence and the CME core material are sufficiently concentrated along a 1D axis so that the position of their top rim is well discernible in the images for most of the time and it is well approximated by the reconstructed curve. Note that the time series of these curves can only reflect the motion normal to the curves. The physical motion of the plasma may include an additional component along the reconstructed curve which we cannot resolve.
In Fig. 4.16 we overplotted examples of the projection of the 3D reconstructed curve and the tie-points onto the images from STEREO A, B and SDO. A measure of the reconstruction error is the distance between the tie points and the reconstructed curve.

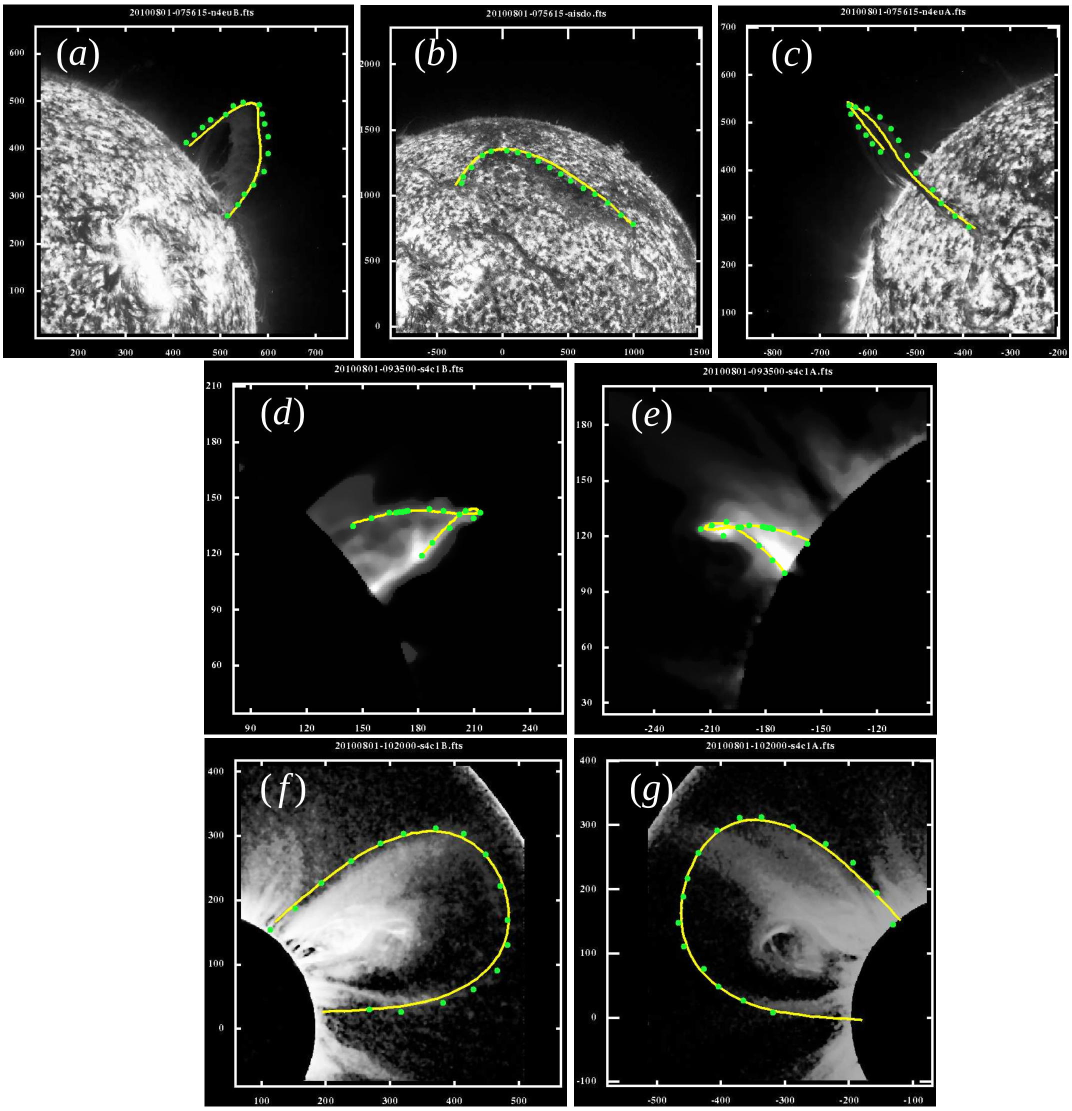

Figure 4.16: Overplot of the projection of the 3D curve (yellow) and the tie-points (green) onto the EUVI images from a) STEREO B, b) SDO, c) STEREO A and onto the COR1 images for the CME core in d) STEREO B and e) STEREO A and for the CME leading edge in f) STEREO B, g) STEREO A.

.

Using EUV 304 Å image data from STEREO B and SDO we first reconstruct the prominence from 5:26 UT till 7:36 UT. For this period we used only two views because in the images from STEREO A the prominence is seen edge on so that the front leg of the prominence covers exactly the rear leg. For this reason, we could not clearly discriminate the legs in the images from STEREO A. For the period 7:46 UT to 8:56 UT we used simultaneous data from all three spacecrafts. After 9:06 UT, the prominence could no more be properly identified in the AIA/SDO data because the projection of its upper edge in the image was very close to the solar limb. Therefore, we used again only two views, STEREO A and B, from 9:06 UT to 9:26 UT. After 9:26 UT, the top part of the prominence had left the field of view of EUVI. The reconstructions are drawn in red in Figure 4.17 until 09:26 UT.

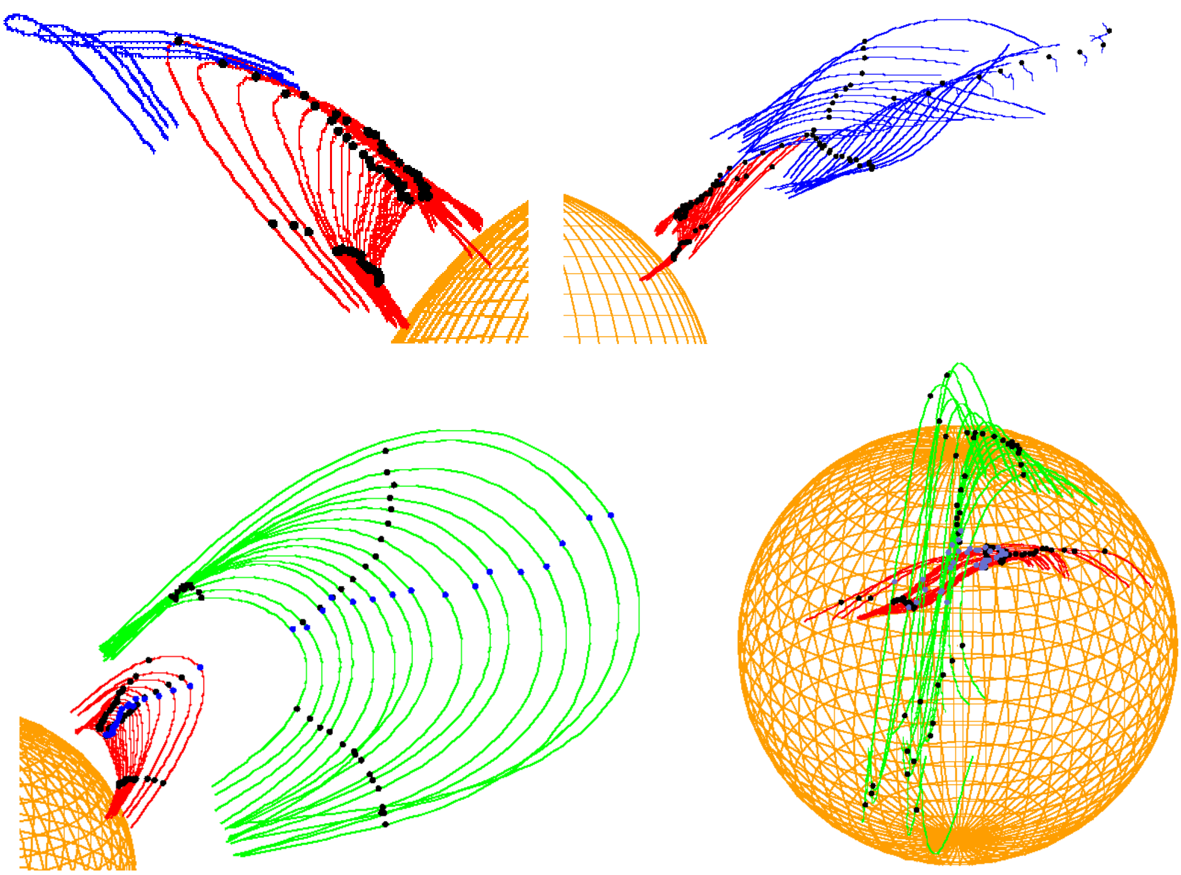

Figure 4.17: The 3D reconstruction of the prominence from EUVI images (red), the reconstruction of CME core using COR1 images (blue) and the CME leading edge (green). The reconstructed curves of the prominence and the CME core (times interval: 9:30 UT - 9:45 UT) (top left panel); the reconstructed curves of the prominence and core of the CME for all times (top right panel) and of the prominence and LE of the CME from two different view directions (bottom panel).

For the determination of the spatial position of the core and the leading edge of the CME, we used data from COR1/STEREO. Since there were no coronagraph data available from LASCO C2/SOHO, we could only use images from two space craft for their reconstruction. For the first frames from 9:30 to 9:45 UT we used data from COR1, the entire visible core structure (blue curves in Fig. 4.17 top left panel) could be reconstructed.

After 9:45 UT, we had to split the reconstruction of the CME core into three parts, namely the west and east extremities and the top because the signal of the core material became rather faint and the connection between these three parts could not be reliably determined any more. In the top right panel of Fig. 4.17, the blue curves represent the 3D reconstructions of the core of the CME at all available times. The last time when we could discern the core signal was at 10:35 UT.

Since the distribution of the core material spread out with time, we found it worthwhile to present our reconstructions at different scales for different times in order to display more details. Thus the left panel shows the reconstruction only until 9:45 UT while the right panel shows it on a different scale until 10:35 UT.

For the visible leading edge of the CME cloud the relationship between the reconstructed curve and the object to be reconstructed is less clear. The visible edge is probably the projection of an extended 2D surface forming the CME hull. For two viewpoints, the curve resulting from a stereoscopic reconstruction approximates the intersection of the CME hull approximately in a plane normal to the mission plane of the two observing space craft. Liewer et al. (2011) analyzed the position of the tie-point reconstruction relative to the CME surface. Because the two spacecraft involved in the reconstruction see different parts as the leading edge the tie-point reconstruction yields a curve somewhere above the CME surface (see Fig. 4.18). Another limitation of the LE reconstruction is that we may reconstruct a different part of the CME surface at different times. Therefore the apparent motion of the reconstructed curve only indirectly reflects the physical motion of the surface. Being ahead of the core material, the leading edge left the field of view

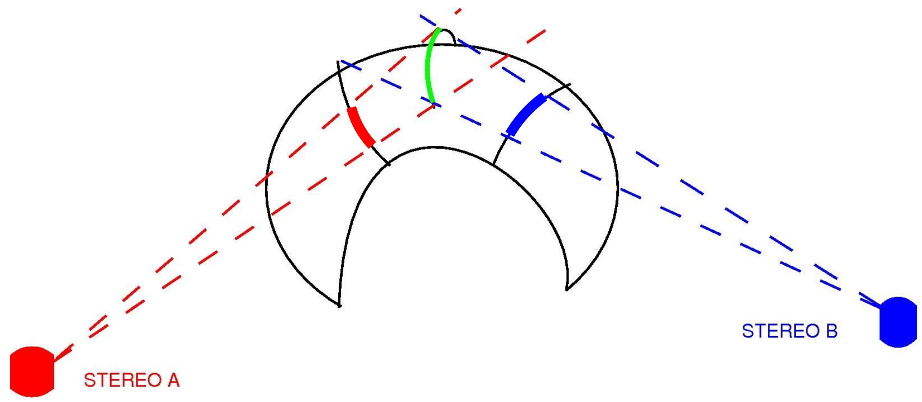

Figure 4.18: Sketch representing effect of different apparent leading edges. The black croissant shape is representing the CME hull. STEREO A/B spacecraft position is represented in red/blue, the dashed rays show lines of sight from the spacecraft seeing the extremes of the CME's hull and the red/blue curves are the actual leading edge observed in the images from STEREO A/B. The green curve which lies at the intersection between the two view directions is the reconstructed leading edge curve.

earlier than the core and we could reconstruct the LE only until 10:25 UT. Two different perspectives of the 3D reconstruction of the prominence from EUV images (red curves) and of the LE (green curves) of the CME are shown in the bottom panel of Fig. 4.17. The image on the left shows how the top and the trace (see Section 4.4.3.1 for a detailed description of the term trace) of the structures evolve and the image on the right shows more clearly how the structures are positioned with respect to each other. The green LE curves shown in Fig. 4.17 are just an approximation to the more extended CME surface. As mentioned above, the reconstructed LE curve lies approximately in a meridional plane somewhat above the intersection of the CME surface with a plane normal to the mission plane of the two observing space craft. The CME surface attached to it may well have a substantial elongation in east-west direction.

4.4.3 Data analysis and results

In general, prominences are dynamic structures and they can contain considerable horizontal motion along the prominence axis with speeds of several tens of km s^{-1} (Martin 1998) even before their eruptive phase. It is difficult therefore to track individual features of the prominence with time. From our reconstruction, we reduce the distributed prominence to a single 3D curve which represents the top rim of the prominence. The kinematics we are going to determine is based on the evolution of this curve which does not resolve the plasma motion along the prominence.

4.4.3.1 Height-time evolution

To characterize the kinematics of the prominence, the CME core and the CME leading edge, we determined the point $\mathbf{C_{top}}$ of the respective reconstructed curve at the largest altitude above the surface for each time t. These points are represented as blue dots in the 3D reconstructions in Fig. 4.17, bottom-left panel. The time evolution of the radial distance of $\mathbf{C_{top}}$ of the prominence (black points) and core of CME (red points) from the Sun center is plotted in Fig. 4.19.

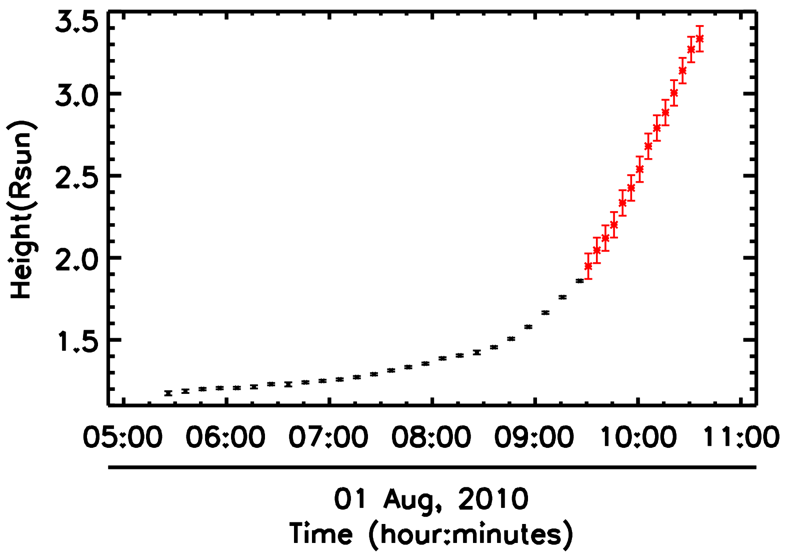

Figure 4.19: Height-time evolution of $\mathbf{C_{top}}$ of the prominence (black points) observed in EUVI and CME core (red points) observed in COR1.

The continuity of the respective curves in Fig. 4.17 and the $\mathbf{C_{top}}$-heights in Fig. 4.19 suggests that the prominence and the CME core material were collocated. The prominence rises slowly at the beginning of its evolution and is strongly accelerated only after approximately 09:00 UT (see the Fig. 4.23). By this time, the top of the prominence had already reached an altitude of 1.5 $R_\odot$. Joshi and Srivastava (2011a) analyzed the evolution of the same prominence. They also observed the two distinct phases of the prominence eruption, but missed to mention that the transition to the intensified acceleration phase occurred rather late, only when the prominence had already reached an appreciable altitude of $\geq$ 1.5 $R_\odot$. The prominence mass is therefore not accelerated by a local explosive-like event close to the surface but receives its main acceleration high above the surface of the Sun. The continuous acceleration at altitudes beyond 1.5 $R_\odot$ is evidence of the magnetic nature of the accelerating force. The height-time curve for $\mathbf{C_{top}}$ of the leading edge is displayed in Fig. 4.20.

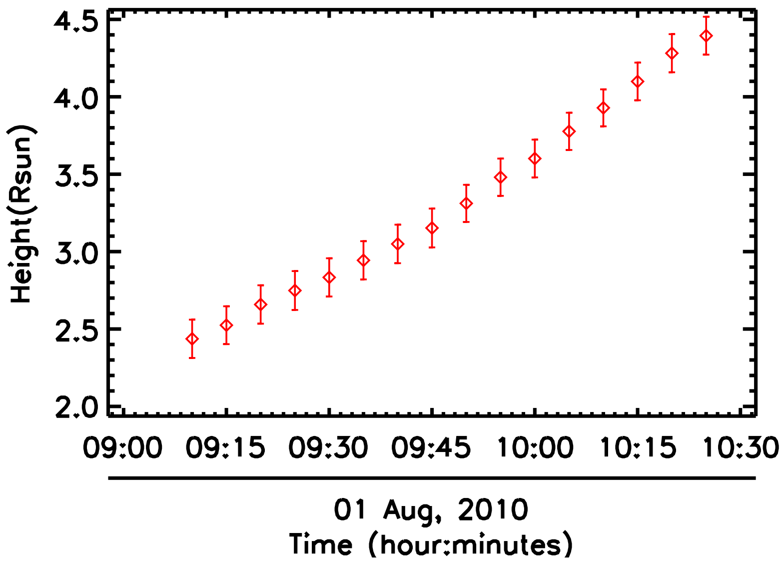

Figure 4.20: Height-time evolution of $\mathbf{C_{top}}$ of the CME leading edge.

We could see the leading edge only in the coronagraph images where it appeared at 09:10 UT for the first time at a heliocentric distance of 2.4 $R_\odot$. Until about 10 UT it rises with an almost constant velocity of 1.5-1.8 $R_\odot$ hr^{-1}.

It is desirable to extend the kinematic description of the curve to more points than just its top point. However, since we cannot easily identify points along the prominence, the CME core or the leading edge at successive times, we can only determine the component of the expansion velocity normal to the curve tangent from the reconstructed curves.

For this purpose, we determine local distances between the curves at successive times to describe the kinematics of the prominence and the CME core. We calculate these distances as follows: Given a point $\mathbf{c}_i(s_j)$ on the curve $\mathbf{c}_i$ at time t_i at a curve parameter s_j, we determine two parameters s_1^* and s_2^* on the curve $\mathbf{c}_{i+1}$ at time t_{i+1} such that $\mathbf{c}_{i+1}(s_1^*)$ is the closest point on $\mathbf{c}_{i+1}$ to $\mathbf{c}_i(s_j)$ and $\mathbf{c}_i(s_j)$ is the closest point on $\mathbf{c}_i$ to $\mathbf{c}_{i+1}(s_2^*)$ (see the sketch from Fig. 4.21). The final curve parameter s'_j on curve $\mathbf{c}_{i+1}$ which we associate with $\mathbf{c}_i(s_j)$ is iterated between $min(s_1^*, s_2^*)$ and $max(s_1^*, s_2^*)$ such that the line $[\mathbf{c}_{i+1}(s'_j), \mathbf{c}_i(s_j)]$

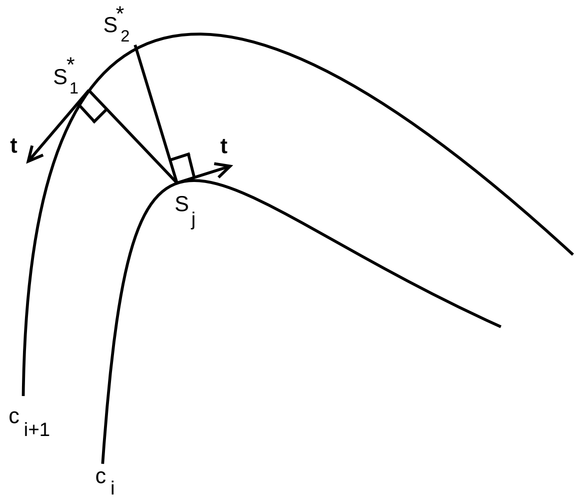

Figure 4.21: Sketch showing a phase from the calculation of the distances between two consecutive curves, c_i and c_{i+1}. The point s_j from the curve c_i is the point which we want to trace on the curve c_{j+1}; the segment $s_j s^*_1$ is perpendicular on the tangent t at the curve C_i; the segment $s_j s^*_1$ is perpendicular on the tangent t at the curve c_{i+1}.

makes the same angle with the tangents $\frac{d}{ds}\mathbf{c}_i(s_j)$ and $\frac{d}{ds}\mathbf{c}_{i+1}(s'_j)$ along the respective curve. Note that, our construction could be reversed, i.e. using the same algorithm, we re-obtain $\mathbf{c}_i(s_j)$ starting from $\mathbf{c}_{i+1}(s_j)$.

This way, we traced three points j along the reconstructed curves of the prominence and the CME core. One of these points initially agreed with $\mathbf{C_{top}}$ and two are initially located equidistantly towards either side of $\mathbf{C_{top}}$ along the curve. The traces are represented in Fig. 4.17 as black dots and termed in the following $\mathbf{C_{top\_prom}}$, $\mathbf{C_{west\_prom}}$, $\mathbf{C_{east\_prom}}$ and $\mathbf{C_{top\_core}}$, $\mathbf{C_{west\_core}}$, $\mathbf{C_{east\_core}}$, respectively.

The height-time diagrams of the trace points are displayed in Fig. 4.22.

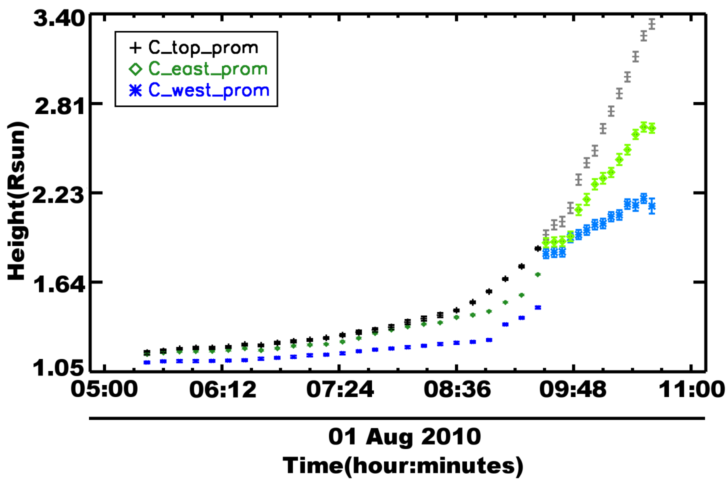

Figure 4.22: Height-time evolution of trace of the parts of the prominence (dark colors) and CME core (light colors).

We can see that there is no significant difference in the rise $\mathbf{C_{top}}$ (Fig. 4.19) and $\mathbf{C_{top\_prom}}$ (Fig. 4.22, black symbols). This can be also observed in the positioning of the points $\mathbf{C_{top}}$ and $\mathbf{C_{top\_prom}}$ in Fig. 4.17. As expected, the trace points $\mathbf{C_{east}}$ and $\mathbf{C_{west}}$ on the flanks of the prominence and CME core curves rise more slowly than the central section of the respective curves, because their traces bend away from the radial propagation direction. However, their speeds differ considerably, with the western branch (green symbols in Fig. 4.22) being significantly faster than the eastern branch (blue symbols).

The discontinuity of the eastern and western trace points in Fig. 4.22 between the prominence and CME core traces is artificial and due to the fact that the trace points had to be repositioned for the CME core traces.

4.4.3.2 Velocities of the prominence and the CME

The evolution of the velocities of $\mathbf{C_{top}}$ and of the trace points $\mathbf{C_{top\_prom}}$, $\mathbf{C_{west\_prom}}$ and $\mathbf{C_{east\_prom}}$ are plotted in Fig. 4.23, respectively Fig. 4.24. The velocity of $\mathbf{C_{top}}$ is obtained

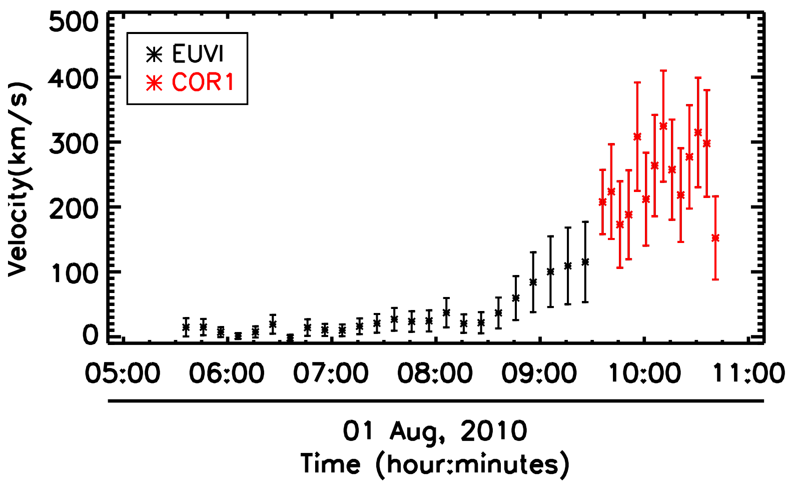

Figure 4.23: Velocity of $\mathbf{C_{top}}$ of the prominence (black points) and the CME core (red points).

by numerical differentiation from the height-time plot (Fig. 4.19) without smoothing. The enhanced noise for the coronagraph data (red dots) is a result of the coronagraph's reduced spatial resolution. The velocities of $\mathbf{C_{top\_prom}}$, $\mathbf{C_{west\_prom}}$ and $\mathbf{C_{east\_prom}}$ were derived from the trace point distances and therefore reflect an absolute velocity including an azimuthal component and not just the radial component as for the $\mathbf{C_{top}}$.

From both diagrams it is apparent that the transition from slow to an accelerated rise of the prominence/core material occurs close to 8:30 UT. After this time, the radial velocity of $\mathbf{C_{top}}$ displayed in Fig. 4.23 increases almost linearly with approximately 150 km s^{-1} per hour until the end of our observations. The velocity of the trace points $\mathbf{C_{prom}}$ in Fig. 4.24 shows more scatter. Within the scatter, the measured velocities of the prominence trace points are almost as high as the velocity of $\mathbf{C_{top}}$. However, as Fig. 4.17 reveals, the trace points bend away from the radial direction and the velocity of the eastern and western trace points obtain a considerable azimuthal component. Hence the prominence material appears to spread out from a virtual center at about a distance of 1.5 $R_\odot$ from the Sun's center.

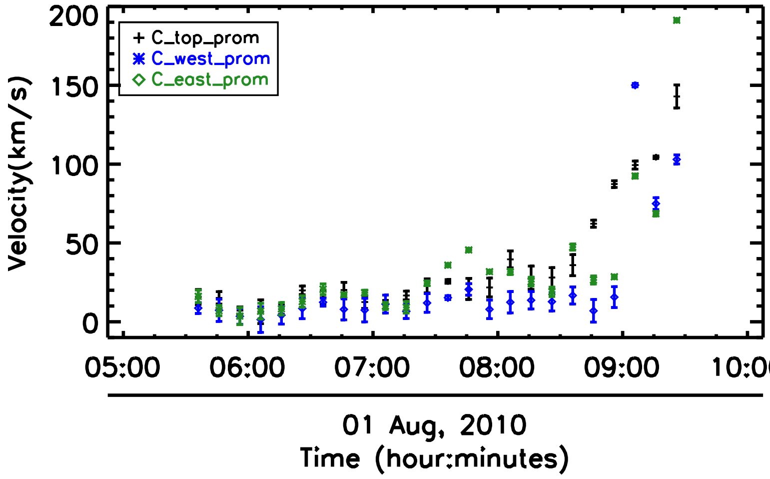

Figure 4.24: Velocity of the trace points of the prominence.

4.4.3.3 Propagation direction

We have defined earlier $\mathbf{C_{top}}$ as the highest point of the structure. Its instantaneous direction from the Sun's center changes in time.

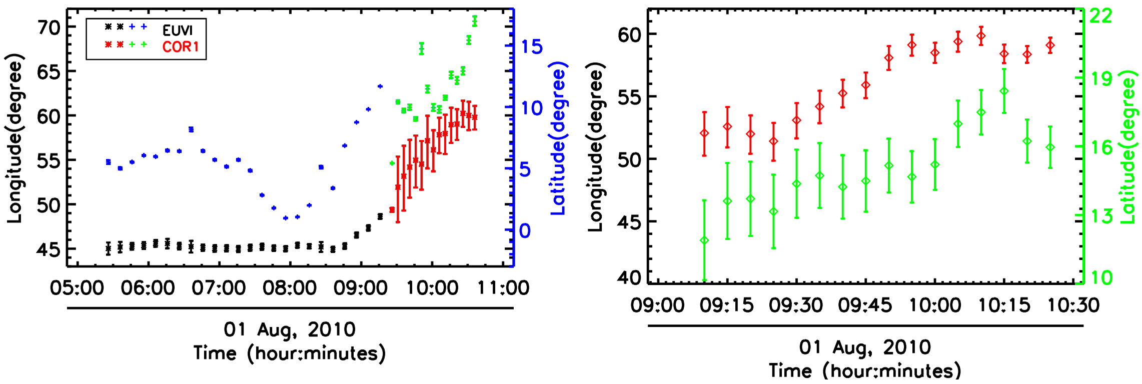

Figure 4.25: left panel: variation of latitude (blue and green dots) and longitude (black and red dots) of the prominence $\mathbf{C_{top}}$ derived from EUVI images (black and blue points) and from coronagraph images (red and green dots); right panel: variation of latitude (green points) and longitude (red points) with time for the $\mathbf{C_{top}}$ of the CME leading edge derived from coronagraph images.

The heliographic angles of this direction of $\mathbf{C_{top}}(t)$ are presented in Fig. 4.25. For the first three hours, till 8:56 UT, the prominence $\mathbf{C_{top}}$ maintains its initial direction except for a slight deflection towards the equator by about 5 degrees. After 8:56 UT, the direction of $\mathbf{C_{top}}$ starts to be continuously bend away from the equator by about 10 degrees/hour and is also changing its latitudinal direction. Recall that prior to 9:30 UT, $\mathbf{C_{top}}$ was derived from the prominence material detected in EUV Helium II line. After 9:30, we trace $\mathbf{C_{top}}(t)$ from the CME core material observed in the white light coronagraphs (red symbols for longitude, green symbols for latitude in Fig. 4.25, left panel) instead. In this respect propagation of the CME core material appears as a seamless continuation of the propagation direction of the prominence material.

For the $\mathbf{C_{top}}$ of the CME leading edge we see the same deflection away from the equator and towards larger longitudes in the evolution of $\mathbf{C_{top}}(t)$ as for the core material after about 9:15 UT (see Fig. 4.25).

4.4.3.4 Angular width

In order to characterize the angular span of the structures, we define an opening angle of the prominence and the leading edge curves at given heliocentric distances to the distance of $\mathbf{C_{top}}$. These distances r_i are chosen to $r_i = 19/20\ |C_{top}|, 18/20\ |C_{top}|, 17/20\ |C_{top}|$ and $16/20\ |C_{top}|$ for the prominence and the CME core curve. The angular widths AW_i are defined by the heliocentric angle between the two intersections $\mathbf{x}$ of the reconstructed curve with the plane $\mathbf{C_{top}} \cdot \mathbf{x} = \mathbf{r_i}$ (points A and B in Fig. 4.26).

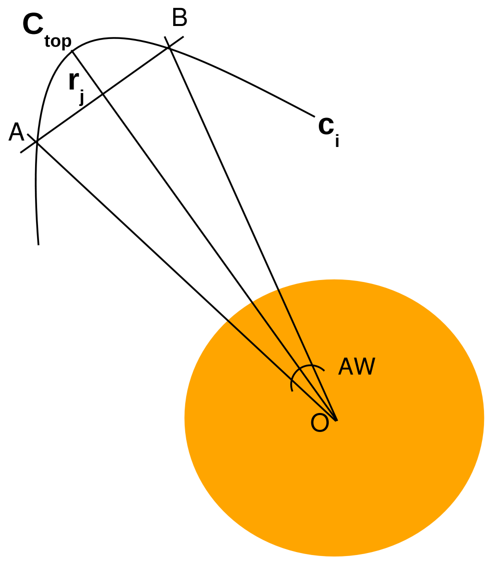

Figure 4.26: Sketch showing the selection of the angular width (AW). The orange circle represent the solar disk and the black curve ($\mathbf{c}_i$) is the reconstructed curve at a certain time. $\mathbf{C_{top}}$ from the curve $\mathbf{c}_i$ is the highest point above the solar surface from the center of the Sun. r_j, $j = 1..4$ is the selected point at different distances from the $\mathbf{C_{top}}$. The perpendicular line at the segment $[C_{top}O]$ passing through r_j intersect the curve $\mathbf{c}_i$ in the points A and B. The angle AOB represent the angular width of the reconstructed curve.

Even though we had to split the CME core reconstruction for some instances into three parts, the opening angles could be calculated for these structures because we could always find a unique pair of intersections for the selected r_i.
The evolution of these opening angles are plotted in Fig. 4.27 for the prominence (observed in He II until 09:35 UT) and the CME core (observed in white light after 09:35 UT). During the rise of the prominence, the opening angle widens by $\approx 8\,^{\circ}$. This tendency of the opening angles can be also noticed in the 3D reconstruction of the curves (Fig. 4.17 - red curves).

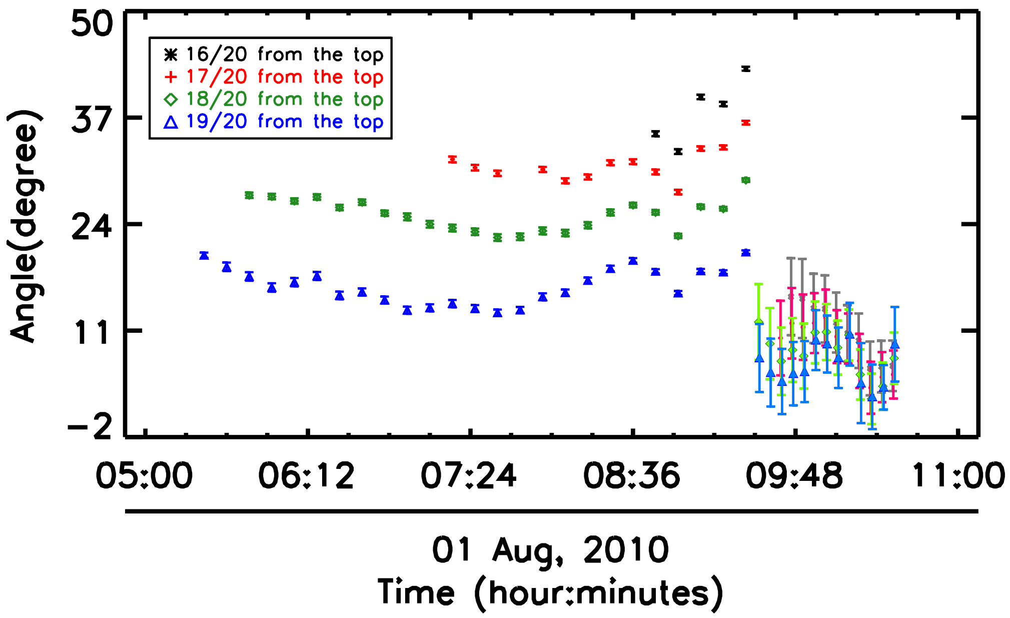

Figure 4.27: Variation of the opening angles of the reconstructed prominence and CME core structure at different distances from the solar center as given in the legend.

In contrast, the CME core material visible after 9:35 UT seems to be much more concentrated in angular extent with opening angles only about half as large as those observed for the prominence. It might be that the bright CME core is made visible in the coronagraph mainly by resonance scattering at neutral hydrogen (Mierla et al. 2011). This discrepancy in angular width could then be explained by a varying concentration of the neutral hydrogen along the rising prominence, such that the concentration drops below visibility towards the ends of the structure. For a similar reason, the coronagraph signal might have faded away on some sections along the prominence axis after 9:45 UT. Since the Thomson scattering signal is proportional to the local plasma density, the Thomson scattering signal should be much more persistent in time.

4.4.3.5 Rotation

Bemporad et al. (2011) analyzed the rotation of an erupting prominence arc observed in STEREO EUVI and COR about its direction of propagation. The angle of rotation was defined as the angle between the meridian plane through the center of the filament between the two filament foot points and the plane spanning the two foot points of the filament and the Sun center (see Fig. 4.28). The initial angle of rotation therefore characterizes the orientation of the prominence in H_α images before the eruption.

Let θ_i and ϕ_i denote the latitude and longitude of the prominence foot points $i = 1, 2$. The segment s defines the length between the prominence foot points and the segment l defines the projection of this length onto the meridian plane. They are given by:

$$s = R_{\odot}[(\cos\theta_2 \sin\phi_2 - \cos\theta_1 \sin\phi_1)^2 + (\cos\theta_2 \cos\phi_2 - \cos\theta_1 \cos\phi_1)^2 + (\sin\theta_2 - \sin\theta_1)^2]^{1/2} , \tag{4.16}$$

$$l = R_{\odot}[(\cos\theta_2 \sin\phi_1 - \cos\theta_1 \sin\phi_1)^2 + (\cos\theta_2 \cos\phi_1 - \cos\theta_1 \cos\phi_1)^2 + (\sin\theta_2 - \sin\theta_1)^2]^{1/2} . \tag{4.17}$$

The rotation angle is obtained from $\alpha = arccos(l/s)$.

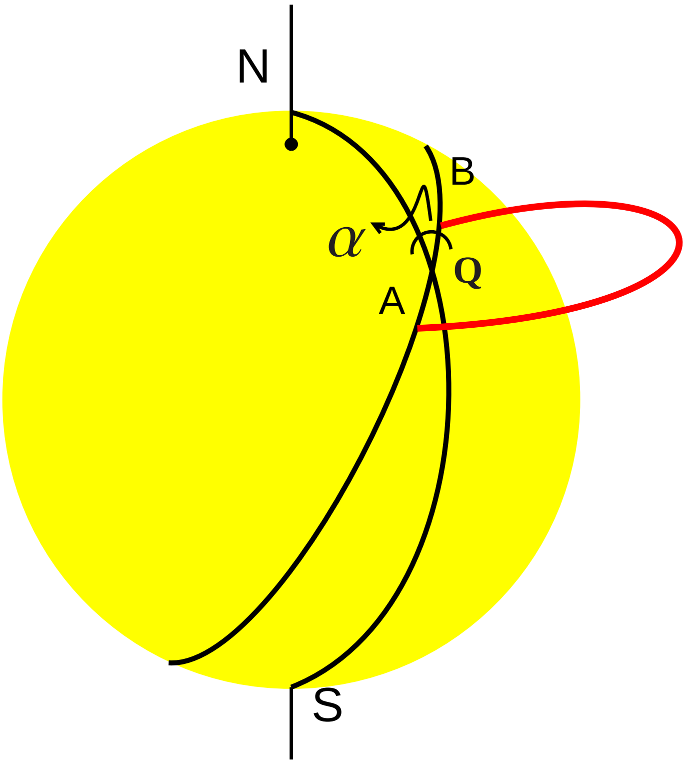

Figure 4.28: Cartoon presenting the Solar disk as black circle; [NS] define the meridian plane and [AB] the plane defined by the foot points of the reconstructed curve c_i which intersects the meridional plane in Q. The angle between the two planes define the rotation angle (θ) of the reconstructed curve.

After the filament eruption, the orientation angles of the filament for various solar radii r_i can be calculated in the same manner if the filament foot points are replaced by two intersection points of the reconstructed filament curve with the heliospheric of radius r_i. We have adopted the method of Bemporad et al. (2011) for the derivation of the rotation angles of our prominence/core reconstruction. The calculated rotation angles are plotted in Fig. 4.29. For various heights h we chose the same radii as for the determination of the opening angles.

In the first part of the eruption until around 9:20 UT, the prominence undergoes a slow counterclockwise rotation. The angles at all four heights evolve similarly, so that the prominence rotates almost rigidly. Around 9:25 UT, the prominence leaves the field of view of EUVI but the CME core structure becomes visible in COR1. At this time, the prominence and the core material have the same angular orientation about 70 degrees with respect to the central meridian plane. However, the core structure seems to reverse the sense of its rotation compared to prominence and increases its rotation speed dramatically until the core material is almost located in the meridional plane. From the COR images one can clearly see the rotation of the core structure (see Fig. 4.16). The reconstruction of the twisted core material is shown in Fig. 4.17 (blue curves from bottom left part). Joshi and Srivastava (2011b) and Li et al. (2011) only observe a counterclockwise twist. They seem to miss the backwards rotation during the late stages of the evolution.

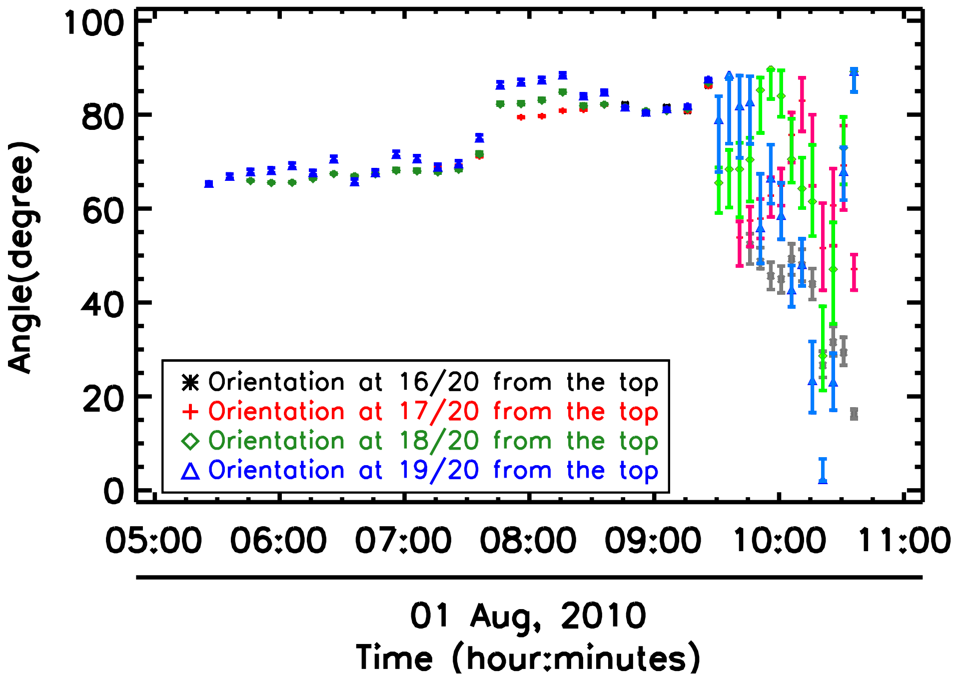

Figure 4.29: Orientation angle of the prominence (before 9:30 UT) and CME core (after 9:30 UT) with respect to a meridional plane centered on the respective structure.

4.4.3.6 Cavity

If the cavity of a CME is present then it is interpreted as the interior cross section of the erupting flux rope (Patsourakos et al. 2010) (see Section 4.2.1).
As described in Section 4.2.1, the prominence material resides in the bottom field-line pockets of the flux rope. In this sense, the flux rope diameter should approximately equal the visible cavity size defined as the distance between $\mathbf{C}_{\mathbf{top}}$ of the prominence and core material and $\mathbf{C}_{\mathbf{top}}$ of the CME leading edge. The variation of this distance is plotted in Fig. 4.30 (upper panel). In Fig. 4.30 (lower panel) we show the relation between the radial cavity size and the opening angle of the prominence as defined above. While the cavity size is a measure of the radial thickness of the flux rope the opening angle of the CME represents the azimuthal size of the flux rope. We observe that these two parameters are not well correlated in time. From the evolution of the opening angle of the prominence-core material we can see that the lateral size narrows with time (see Fig. 4.27).
The distance between the top of the prominence and the leading edge is observed to increase until about 10:25 UT. A comparison of Fig. 4.19, 4.20 shows that the top part of

the leading edge propagates with an almost constant speed of 220 km s^{-1} while the prominence/CME core gradually accelerates and reaches a comparable radial velocity only at about 10:25 UT. By this time, the cavity has reached a size of 1.3 $R_{\odot}$. The increasing size of the cavity represents a signature of the expanding flux rope.

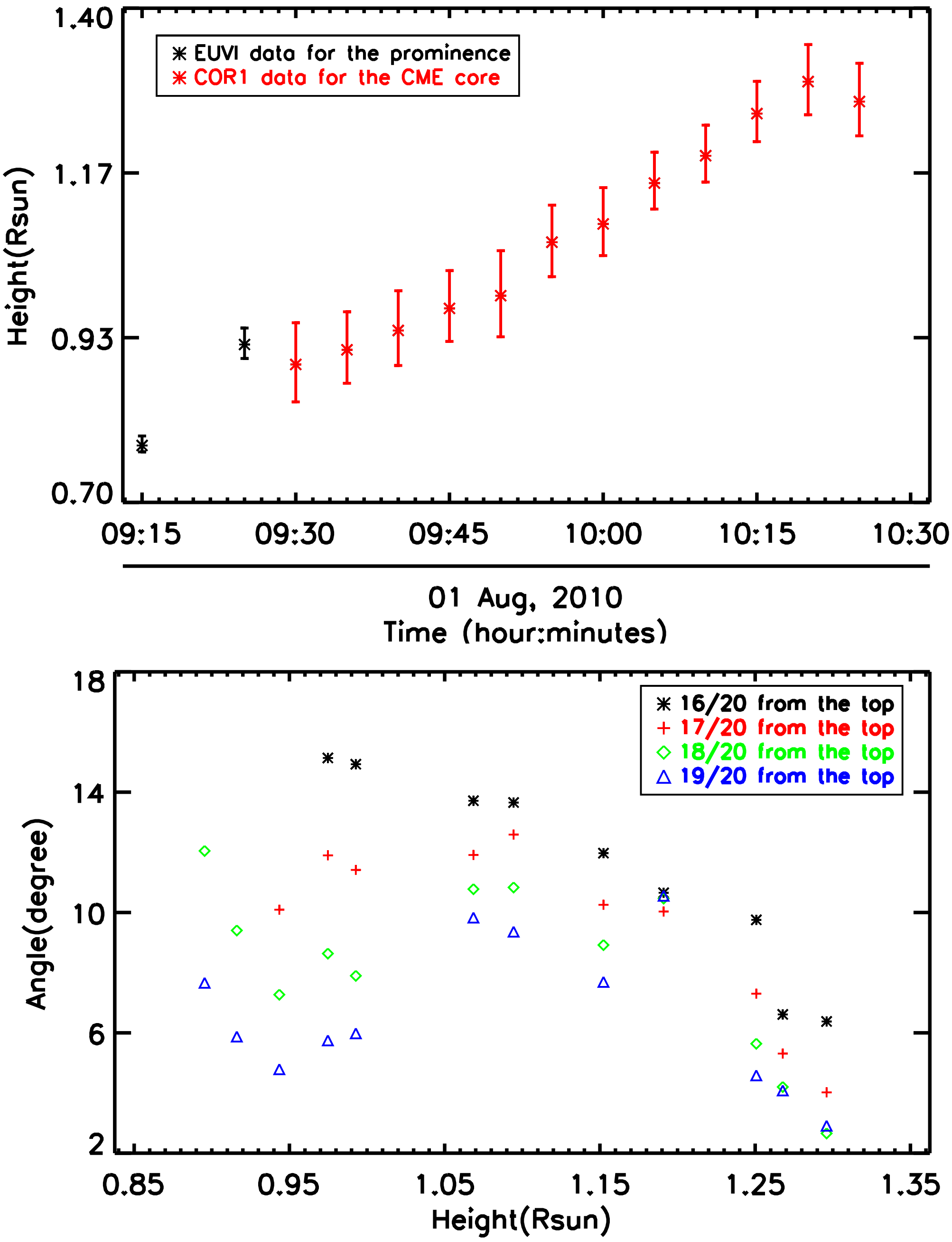

Figure 4.30: upper panel: Variation of the CME cavity size with time; lower panel: relation between cavity size and opening angle of the prominence-core at different distances from the Sun's center.

4.4.4 Discussion and summary

The eruption of the prominence can be described as a loss of the balance between the magnetic pressure and magnetic tension in the corona (Aulanier et al. 2010). The magnetic pressure forces tend to expand the magnetic configuration in the upward direction while the magnetic tension tends to restrain it downwards (Linker et al. 2003). For the prominence eruption studied, there could have been a complex magnetic reorganization which made the prominence system lose its equilibrium.
One contribution to this reorganization could have been local cancellation of flux at the photospheric inversion line below the main axis of the prominence. As the flux cancels, low-lying magnetic field lines lose their connection to the photosphere and form a flux rope. This flux rope supports the prominence material and as the flux cancellation continues, it slowly starts to rise. We can observe this behavior in the first part of the height time profile of the prominence (Fig. 4.19, 4.22).
Another contribution to the reorganization may have been produced by the change of the global coronal magnetic topology. As we have already mentioned above, the eruption of this prominence is the second in a series of eruptions. The eruption before may have weakened the coronal magnetic tension at the prominence site which subsequently triggered the fast eruption phase of the event analyzed here (Fig. 4.19, 4.20). A similar evolution was numerically simulated by Török et al. (2011) with the aim to model the chain of prominence eruptions from 1 August 2010. They configured the initial conditions of the simulation in agreement to the observed magnetogram prior to the eruption sequence. The initial configuration of the simulation is shown in Fig. 4.31a. The coronal field contains four flux ropes surrounded by magnetic arcades. The flux ropes (FR) are numbered according to the eruption order. Flux ropes FR2 and FR3 are embedded in a pseudo streamer (green arcades) enveloped by a streamer (pink lines), while FR1 is overlaid by a streamer arcade. Flux rope FR2 is equivalent with the prominence studied in our analysis. By imposing a flow at the bottom boundary toward the inversion line below FR1 an expansion of this flux rope could be triggered. FR1 rises slowly to a critical hight followed by a rapid acceleration. As the FR1 expands, it compresses the streamers of FR2 and 3 (see Fig. 4.31b). This in turn triggers a reconnection between the streamer field lines of FR2 and FR3 and the field lines of the pseudo streamer above FR2. As a consequence of the removal of stabilizing flux above FR2, the magnetic tension on FR2 decreases and the flux rope is allowed to rise. From simulations of Török et al. (2011) shown in Fig. 4.31b, a counterclockwise rotation of FR2 during the initial phase of the rise encounter can be observed which we have found in our observations. One of the conclusions of the Török et al. (2011) paper is that the chain of eruptive events is related to the structural properties of large-scale coronal field prior to the eruptions.
The eruption of the prominence analyzed here was also reconstructed and analyzed by Joshi and Srivastava (2011b) and Li et al. (2011). In both of these papers, the authors reconstruct different features of the prominence and they use only two view directions for their reconstruction, even though Li et al. (2011) analyze the event using data from three satellites.

In this work, we make use of simultaneous data from three satellites and reconstruct curves which represent the 3D location of the highest ridge of the prominence, the CME core material and the leading edge. As explained in Chapter 2, Section 2.3, with our new

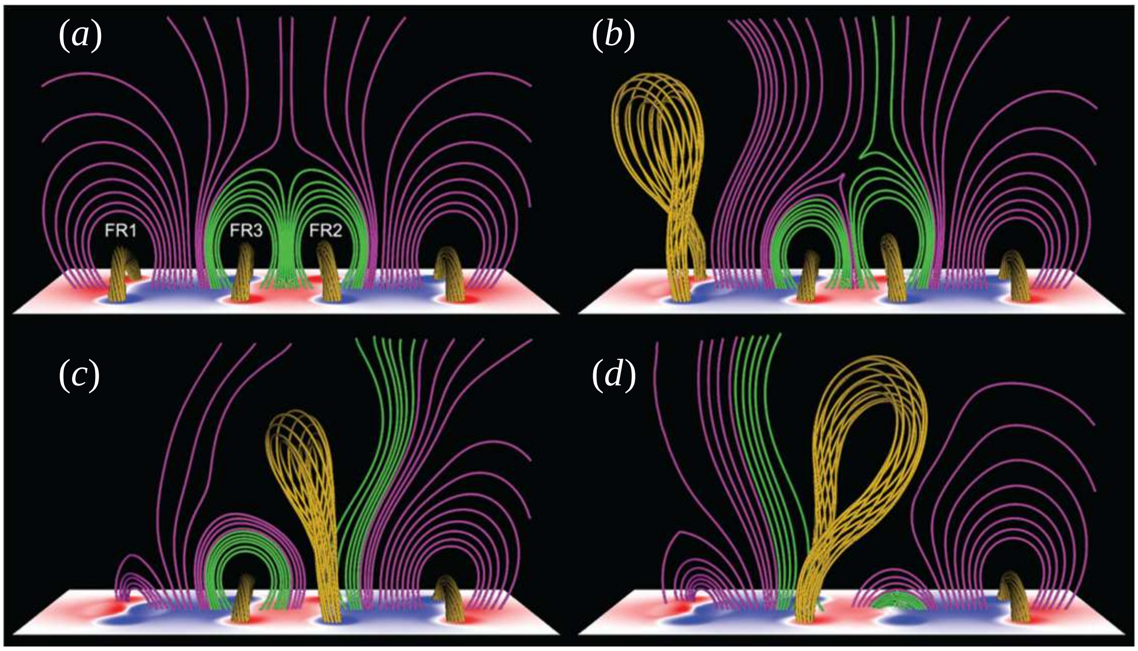

Figure 4.31: Figure taken from Török et al. (2011), showing magnetic field lines with fixed footpoints and the normal component of the magnetic field at the bottom plane, where red (blue) depicts positive (negative) fields. Orange lines belong to the flux ropes, green ones to the initial pseudo-streamer lobes, and pink ones to initially closed or (semi-) open overlying flux. Panel (a) shows the configuration after initial relaxation and panels (b) - (d) show the successive flux rope eruptions and ambient field evolution (Török et al. 2011).

method, we do not need to match individual tie-points in different images but we directly solve for the optimal spline representation of a 3D curve which matches the tie-points in all images. We are convinced that our procedure yields a more reliable and precise reconstruction compared to those of the previous authors.

Joshi and Srivastava (2011b) analyzed the evolution of the position, height and acceleration of the prominence features and Li et al. (2011) investigates the prominence velocity, using EUVI data. Joshi and Srivastava (2011a) made also an analysis of the CME triggered by the prominence eruption. They derived the 3D position, velocity and acceleration of the top point of the leading edge and of the core of the CME. With our analysis of the CME core and the leading edge of the CME we extend their analyze. While Li et al. (2011) found a maximum acceleration of around 40 m s^{-2} for the top part of the prominence, Joshi and Srivastava (2011b) only obtain a maximum acceleration of around 11 m s^{-2}. We have obtained a maximum acceleration of 33 m s^{-2} for the prominence C_{top} as observed in EUVI data. Both authors noted the counterclockwise rotation of the prominence during the easy rise phase. From our analysis we found two phases of the rotation: an initial slow counterclockwise rotation of the prominence and a subsequent fast clockwise rotation of the core material.

Due to the lack of a quantitative analysis, the evolution of the rising prominence, its core material and CME surface is often assumed to be self-similar: it can be described by a single scaling parameter which grows in time while the intrinsic shape remains unchanged. From our analysis we find that the evolution is much more complex. In future it would be desirable to relate details of the kinematic evolution to features of the coronal field. Since we presume that the major driving force is of magnetic origin, we expect that such relations exist.

In our analysis we try to follow the evolution of the eruption from the time of the initial rise of the prominence until the CME core leaves the field of view of the COR1 coronagraph. The prominence and CME core material do not evolve in a self-similar way. We calculate various parameters which characterize the 3D curves representing the prominence and CME core location.

The prominence and the CME core were observed with different instruments, the EUVI telescope and the coronagraph, respectively, which have slightly overlapping fields of view. From our analysis we find a good continuity of the radial motion of the respective top sections of the structures, and a continuous angle of rotation about the propagation direction as the prominence leaves the EUVI field of view and the CME core comes into sight of COR1. However the two structures are discontinuous in their lateral extent. From monitoring the opening angles we find that while the prominence spans over about 40 degrees, the CME core appears only about 10 degrees wide.

Using the method of Bemporad et al. (2011), we calculate the rotation at different heights for the prominence and the CME core. We could see that different parts of the structures rotate first rigidly but when the core material reaches about 2 $R_\odot$, its top part rapidly rotates in reverse direction.

In the overall dynamic evolution we could distinguish two phases, a slow and an accelerated rise of the prominence/CME core, the latter starting at about 8:30 UT. After this time, this structure is accelerating gradually to speeds above 200 km s^{-1} in roughly 2 hours while the leading edge seems to have been launched at the same time, as the prominence/core. It propagates from the beginning with a constant speed of 220 km s^{-1}. During this second phase, we see an involved motion of the prominence/CME core material which is far from a rigid or a self-similar evolution. After 8:30 UT, when the major acceleration sets in, the top part of the prominence starts also to be deflected in longitude and after an intermediate bending towards the heliographic equator, its propagation direction turns steadily towards higher latitudes. The same changes can be seen in the propagation direction of the top section of the leading edge, though somewhat less vigorous. It should be recalled that the LE curve cannot be associated with a clear localized ridge of plasma material, but is the result of the projection of an extended surface onto two observing view directions. Hence changes in the LE curve may also reflect intrinsic deformations of the surface. The evolution of the visible structures of an erupting prominence is therefore very complex. It is very probable that the accelerating forces are largely to magnetic. The complex rotation of the prominence may be due to the presence of helically twisted fields.

5 Coronal magnetic field modeling using stereoscopy constraints

In this chapter we will present the tests which we have performed for the S-NLFFF (Stereoscopic-NLFFF) method described in Chapter 2. Parts from the text of this chapter have been extracted from the paper "Coronal magnetic field modeling using stereoscopic constraints"published in Astronomy& Astrophysics journal.

5.1 Introduction

The S-NLFFF method has already been explained in Chapter 2, Section 2.5. It is an extension of the Nonlinear Force Free Field (NLFFF) variational method used for the extrapolation of the magnetic field from the photosphere into the corona.

S-NLFFF minimizes a scalar cost function $L_{\mathrm{tot}} = \sum_{n=1}^{4} L_n$ (see Eq. 2.39) which consists of four terms $Ł_n$ quantifying constraints which the final solution should satisfy. The first term $Ł_1$ (Eq. 2.36) corresponds to the Lorenz-force equation, the second term $Ł_2$ (Eq. 2.37) corresponds to the solenoidal condition and the third term, $Ł_3$ (Eq. 2.38) measures the match with the observed photospheric vector magnetograms. The last term which is a new feature of our method, $Ł_4$ (Eq. 2.42) constrains the magnetic field to be aligned to some selected loops generally obtained from a three dimensional stereoscopic reconstruction. The minimization of the functional $Ł_{tot}$ is achieved by a Landweber iteration as described in Chapter 2. At the end of the iteration process, some residual values of the cost function will be obtained. We denote these values as $Ł_i^{\infty}$, i=1...4. These indicate the convergence of the iteration and are used in the next section (5.2) to evaluate the S-NLFFF performance.

5.2 Testing the S-NLFFF (Stereoscopic-NonLinear Force Free Field) method

We test the optimization method S-NLFFF described in Chapter 2 using a semi-analytical force-free field solution proposed by Low and Lou (1990). From this field solution we calculated various simulated input data for the tests. The set of solutions of Low & Lou has been used by a large number of authors to perform tests of NLFFF codes, like (Wiegelmann and Inhester 2010, Valori et al. 2007, Thalmann et al. 2011).The solution was derived by Low and Lou (1990) by solving the Grad-Shafranov equation for an axisymmetric nonlinear force-free field in spherical geometry for which the magnetic field can be expressed in common spherical coordinates as

$$\mathbf{B} = \frac{1}{r\sin\theta}\left(\frac{\partial A}{\partial\theta}\hat{\mathbf{r}} - \frac{\partial A}{\partial r}\hat{\theta} + Q\hat{\phi}\right) . \tag{5.1}$$

Here A is the flux function which is independent of the azimuthal angle ϕ. Q takes care of ϕ component of **B** which becomes force-free if Q depends only on A with $\alpha = \frac{dA}{dQ}$ (Low and Lou 1990). The flux function then satisfies the Grad-Shafranov equation

$$\frac{\partial^2 A}{\partial r^2} + \frac{1-\mu^2}{r^2}\frac{\partial^2 A}{\partial\mu^2} + Q\frac{dQ}{dA} = 0 , \tag{5.2}$$

where $\mu = \cos\theta$. Low & Lou restrict to the special case $\alpha = \frac{dA}{dQ} \sim A^{1/n}$. The solutions are of the form:

$$Q(A) = aA^{1+\frac{1}{n}} , \tag{5.3}$$

$$A(r,\theta) = \frac{P(\mu)}{r^n} , \tag{5.4}$$

where a and n are constants and the scalar function P satisfies a nonlinear modification of the Legendre differential equation (Low and Lou 1990)

$$(1-\mu^2)\frac{d^2P}{d\mu^2} + n(n+1)P + a^2\frac{1+n}{n}P^{1+2/n} = 0 , \tag{5.5}$$

which has discrete eigenvalues since the boundaries are fixed. Then a_n are the eigenvalues for parameter $n \in \mathbb{N}$.

A value of $n = 1$ and $a = 0$ corresponds to a linear dipole field.

In our and similar tests, the center of the spherical coordinate system is placed below the bottom surface of the computational box and, in order to break the symmetry, its axis is tilted obliquely with respect to the edges of the computational box.

For our investigation we used two of the Low & Lou semi-analytical force free field solutions:

Case I : the depth for the center of the solution was chosen at $l = 0.3$ times the edge length of the computational box, a tilt angle of $\Phi = 0.6\cdot\pi/4$ degrees and a multipole order $n = 1$. The computational box has 64 x 64 x 32 grid points.

Case II: the depth for the center of the solution was chosen at $l = 0.3$ times the edge length of the computational box, a tilt angle of $\Phi = 4\cdot\pi/5$ degrees and a multipole order $n = 3$. The computational box has 64 x 64 x 32 grid points.

For both Cases (I and II) we generate by numerical minimization of $Ł_1...Ł_3$ a discrete reference field as the solution of the conventional NLFFF problem with the boundary data from the analytical Low and Lou field solution. This field is close but not identical to the analytic Low and Lou field. From this discrete reference field, we generate three (for Case I) and ten (for Case II) loops with a fourth order Runge-Kutta method. During the loop selection process, we encountered some problems which will need to be investigated in the future. The problems is related to the reference field **b**. Initially, we tried to choose loops randomly, in order to have a large coverage in the computational box. Unfortunately, some traced loops show wiggles (see Fig. 5.1 for some examples) which are unlikely to occur for the Low & Lou model field.

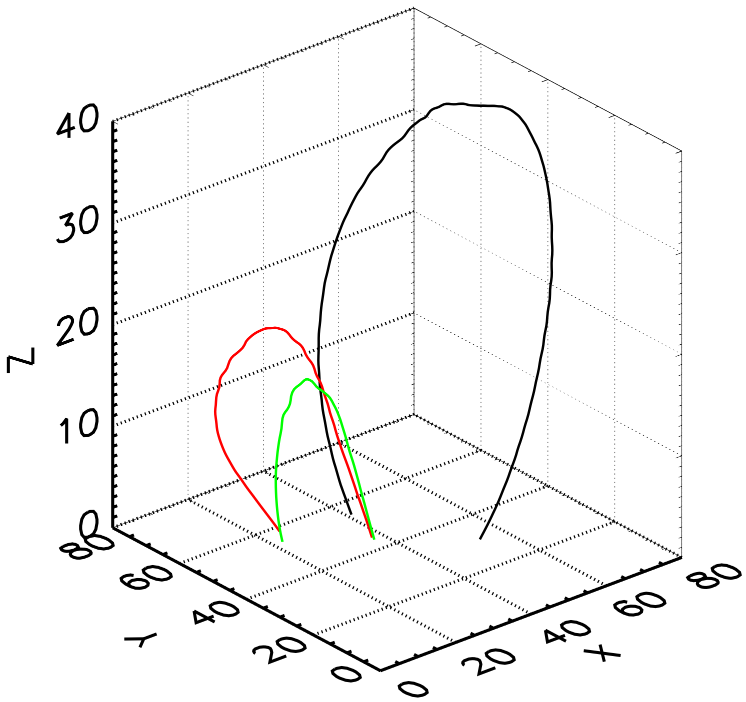

Figure 5.1: Examples of loops with wiggling.

The reason for these wiggles is probably numerical but could not yet be explained exactly.

In consequence, we chose only loops which does not present wiggles. These loops, termed *consistent loops*, will be used as the source for the loop data in our new variational term, in order to simulate the 3D reconstructed loops from observations.

We have made sure that we recover the reference solution from the new S-NLFFF code if we use the correct surface boundary data of the reference field and the *consistent loops* in the L_4 term. This test essentially proves that our discretization is consistent. The angle between the loop tangents and the field solution should be zero in this case. Because of the numerical roundoff errors mainly from the loop tracing, the actual deviation angles we recover have an average of less than one degree and a maximum value of 2.8 degrees. We will consider this maximum angle as our *standard angle error* which yields the upper bound for the deviation with which we can determine the alignment of the field and the loops.

When we apply our code to measured data, we cannot hope that boundary and loop data are consistent. We therefore perform two further tests to demonstrate that our code can help to improve the results obtained with conventional extrapolation calculations:
1) We reconstruct the Low and Lou solution in the case when the bottom surface data and the loop data are not consistent.
2) We reconstruct the Low and Lou solution in the case when the loop data is consistent

but the bottom surface data is contaminated by noise.
For both tests, we try to determine the optimum regularization parameter ξ_4 of our new variational term $Ł_4$. The relative magnitude of the other regularization parameters ξ_1, ξ_2, ξ_3 has been determined before (Wiegelmann 2004) and is not changed.

5.2.1 Testing the method for Case I

In Fig. 5.2 we show the three components, B_x, B_y, B_z, of the Low & Lou magnetic field of our choice of parameters.

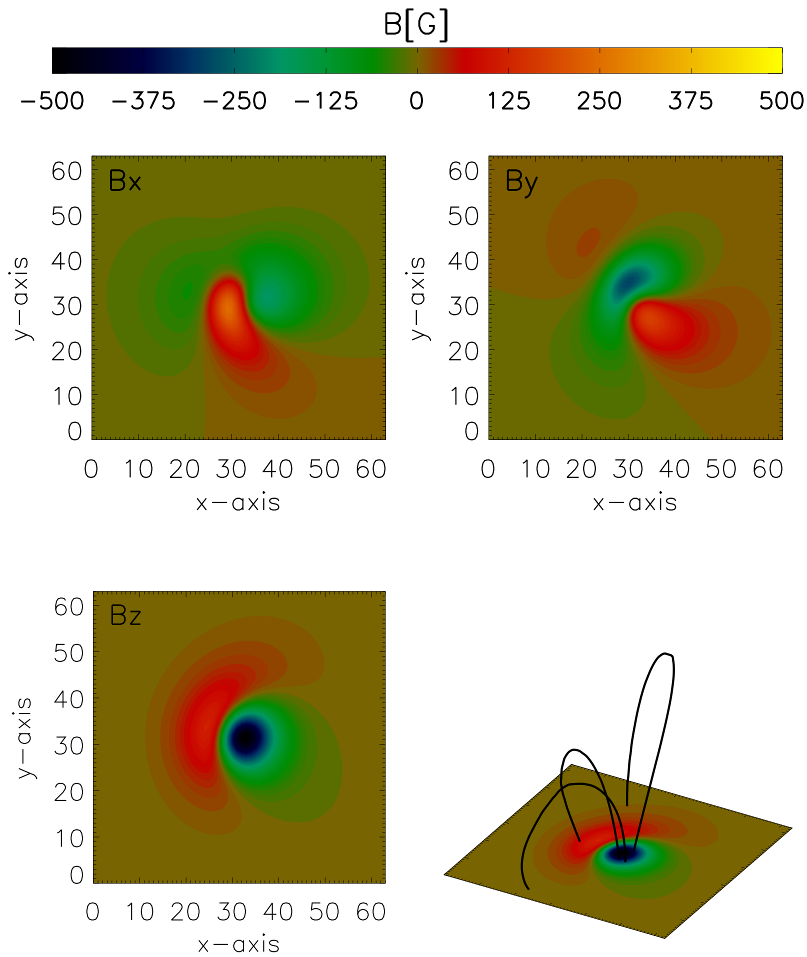

Figure 5.2: The three Cartesian components of the Low & Lou synthetic magnetogram used as bottom boundary in the 64x64x32 pixels computational box. The top row shows the B_x(left) and B_y(right) components, the bottom row the B_z(left) component and an oblique view on the B_z magnetogram with the three loops extracted for our tests (right).

5.2.1.1 Inconsistent surface and loop data

In this test, we modified the *consistent loop* coordinates by multiplying the z components of $\mathbf{c}_i(s)$ with 1.05, where $\mathbf{c}_i(s)$ represents the 3D loop position in terms of the loop parameters along its length and i stands for different loops (see Chapter 2, Section 2.5.1). Due to this manipulation, the angles between the *consistent loops* and the *modified loops* at the same loop parameter s deviate by up to 20 degrees. The *modified loops* do not fit any more to the boundary data and there is very probably no force-free magnetic field which can satisfy both input data exactly. Under these conditions, not all terms $Ł_i^\infty$ can be iterated to small values. Note also that if the z components of a magnetic field are enhanced in a similar way, the resulting field is not divergence-free any more. It is therefore probable that a magnetic field which fits the three *modified loops* differs considerably from the reference field. In Fig. 5.3 we display the angles $\theta_i(s_j)$ between the loop tangent $\mathbf{t}_i(s_j)$ of the

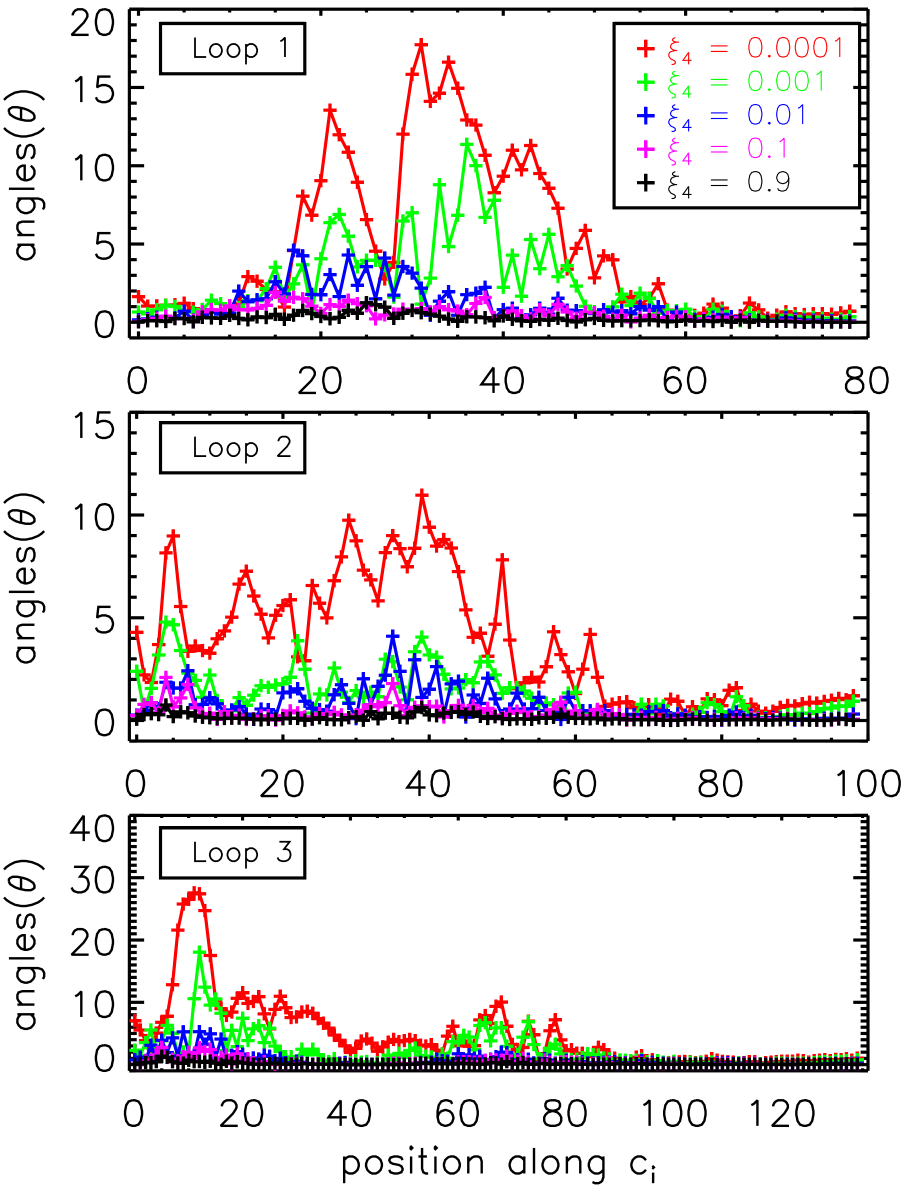

Figure 5.3: The angles $\theta_i(s)$ between the tangent of the *modified loops* $i = 1, 2, 3$ and the interpolated magnetic field $\overline{\mathbf{B}}(\mathbf{c_i}(s_j))$ at curve parameter s along the loop. The different colors represent the angles for magnetic field models obtained with different regularization parameters ξ_4 =0.9 (black), 0.1 (cyan), 0.01 (blue), 0.001 (green) and 0.0001 (red).

modified loop input data and the magnetic field $\mathbf{B}$ returned from the S-NLFFF code for various values of ξ_4 and for each loop i. The angles were determined by interpolating $\mathbf{B}$ given on the computational grid to $\mathbf{c}_i(s_j)$, where s_j is the loop parameter along its length.

Note that for $\xi_4 = 0$, we actually run the conventional NLFFF code and we obtain the reference field as a result. In this case, the angles $\theta_i(s_j)$ just represent the amount of modification applied to obtain the *modified loops*. With ξ_4 increasing, we force the returned field more and more to become aligned with the modified loops so that $\theta_i(s_j)$ decreases. The angles vary significantly along the loop and differently for different loops. With ξ_4 near unity, we can reduce the average angles for all loops to well below one degree. For the $\xi_4 = 0.90$ the maximum angle is 1.24 degrees for loop 1, 0.75 degrees for loop 2, and 1.34 degrees for loop 3. To have a better view of the dependence of the angles θ_i on the regularization parameter, we also show the decrease of the root mean square angle with ξ_4 for each loop in Fig. 5.4. The error bars have the size of the *standard angle error* determined above.

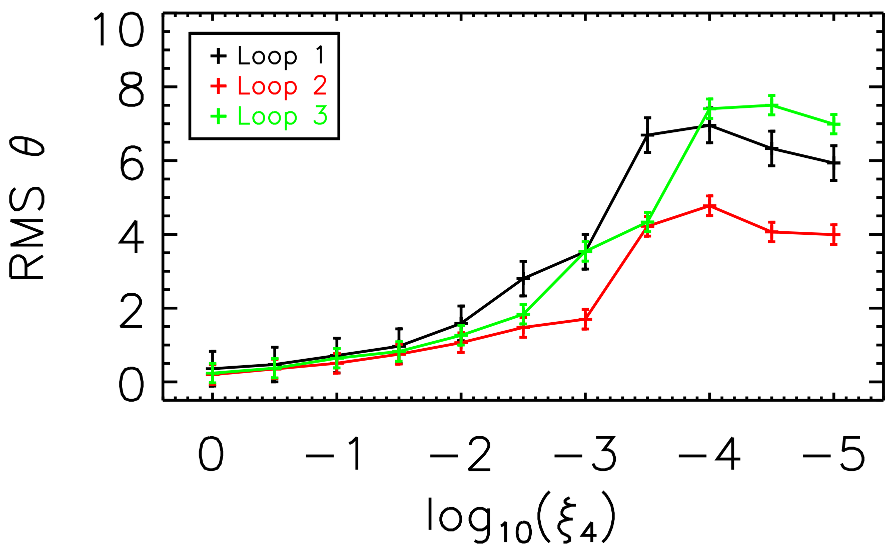

Figure 5.4: Dependence of the root mean square angle θ with ξ_4 for each *modified loop* as shown in Fig. 5.3.

This behavior is well reflected in the dependence of $Ł_4^\infty$ on the regularization parameter ξ_4 shown in Fig. 5.5 along with the variation of the other terms $Ł_i^\infty$. Again, $\xi_4 = 0$ represents the reference field solution and the values of $Ł_i^\infty$ in this case can serve as reference values which can be achieved with the discretization we have chosen. As expected from the improved angles $\theta_i(s_j)$, the term $Ł_4^\infty$ decreases with increasing ξ_4.

However, the better we fit the loop data, the bigger the discrepancy with the surface data as reflected in $Ł_3^\infty$ and for large values $\xi_4 > 1$ also with the force-free and divergence-free conditions in $Ł_1^\infty$ and $Ł_2^\infty$. Hence with the choice of ξ_4, we can shift the emphasis between the boundary magnetogram and the loop data if both are inconsistent with each other. If ξ_4 is smaller than unity, we obtain a nearly force-free magnetic field as proven by the only small variations of $Ł_1^\infty$ and $Ł_2^\infty$ with ξ_4 in this range. For values $\xi_4 > 1$, the values of $Ł_1^\infty$ and $Ł_2^\infty$ rise indicating that the field model increasingly deviates from a force-free and divergence-free solution. The optimal value of ξ_4 which minimizes $\sum \log Ł_i$ therefore lies near unity. In Fig. 5.5, right panel, we show the dependence of $\sum \log Ł_i$ from $\log \xi_4$.

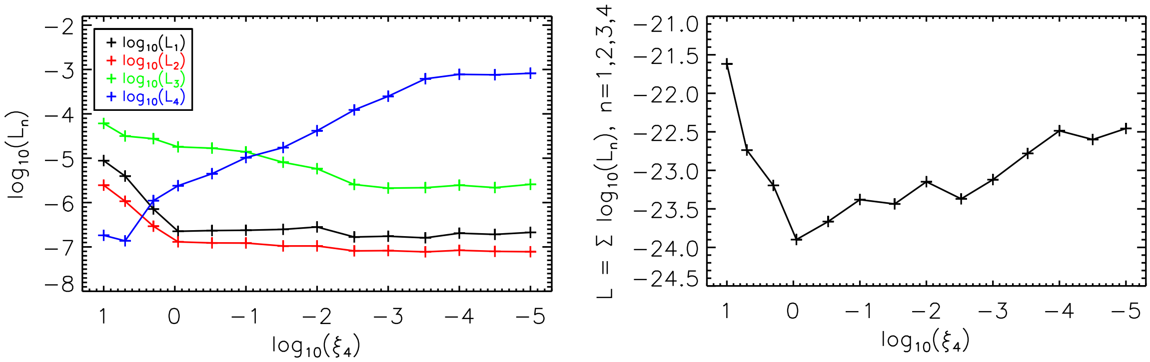

Figure 5.5: The left panel shows the dependence of $\log Ł_1^\infty$ (black), $\log Ł_2^\infty$ (red), $\log Ł_3^\infty$ (green) and $\log Ł_4^\infty$ (blue) with $\log \xi_4$ for correct bottom data and modified loop data. The right panel shows the dependence of $\sum_i \log Ł_i^\infty$ with $\log \xi_4$ for correct bottom data and modified loop data. The position of the minimum is expected to yield the optimal value for ξ_4.

5.2.1.2 Noisy surface data

In this test we use the *consistent loop* data as input but we modify the boundary data by random noise. It should be noted that a force-free field cannot be found for every boundary condition and by adding noise to the boundary data, it very probably becomes inconsistent with a force-free field above, even if we do not constrain the problem further by additional loop data. The incentive of the test is to show that adding the loop data improves the field model we compute in the end.

In Fig. 5.6 we show the modified boundary data.

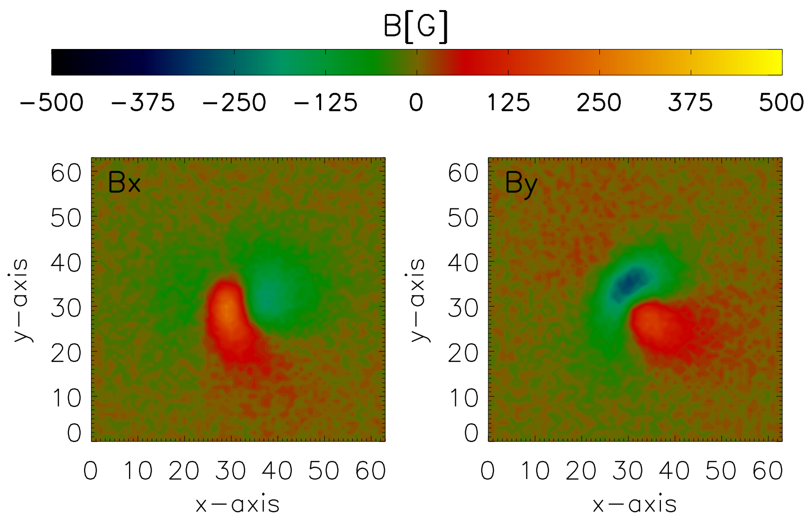

Figure 5.6: The horizontal components of Low & Lou magnetogram modified by adding noise. The vertical component is unchanged as in Fig. 5.2.

The noise added to the B_x and B_y components of the magnetic field amounts to about 3% of the maximum absolute values in the respective component. B_z is left unchanged because typically the horizontal (or plane-of-the-sky) components which are derived from

Hanle-effect measurements are much less precise than the vertical (or line-of-sight) component determined by the Zeeman-effect (Foukal 1990).

We apply these input data to the S-NLFFF code as above and vary again ξ_4 over a wide range of values. Again we can force the field model successfully to become aligned with the loop data if we increase ξ_4 up to unity (see Fig. 5.7, 5.8, 5.9).

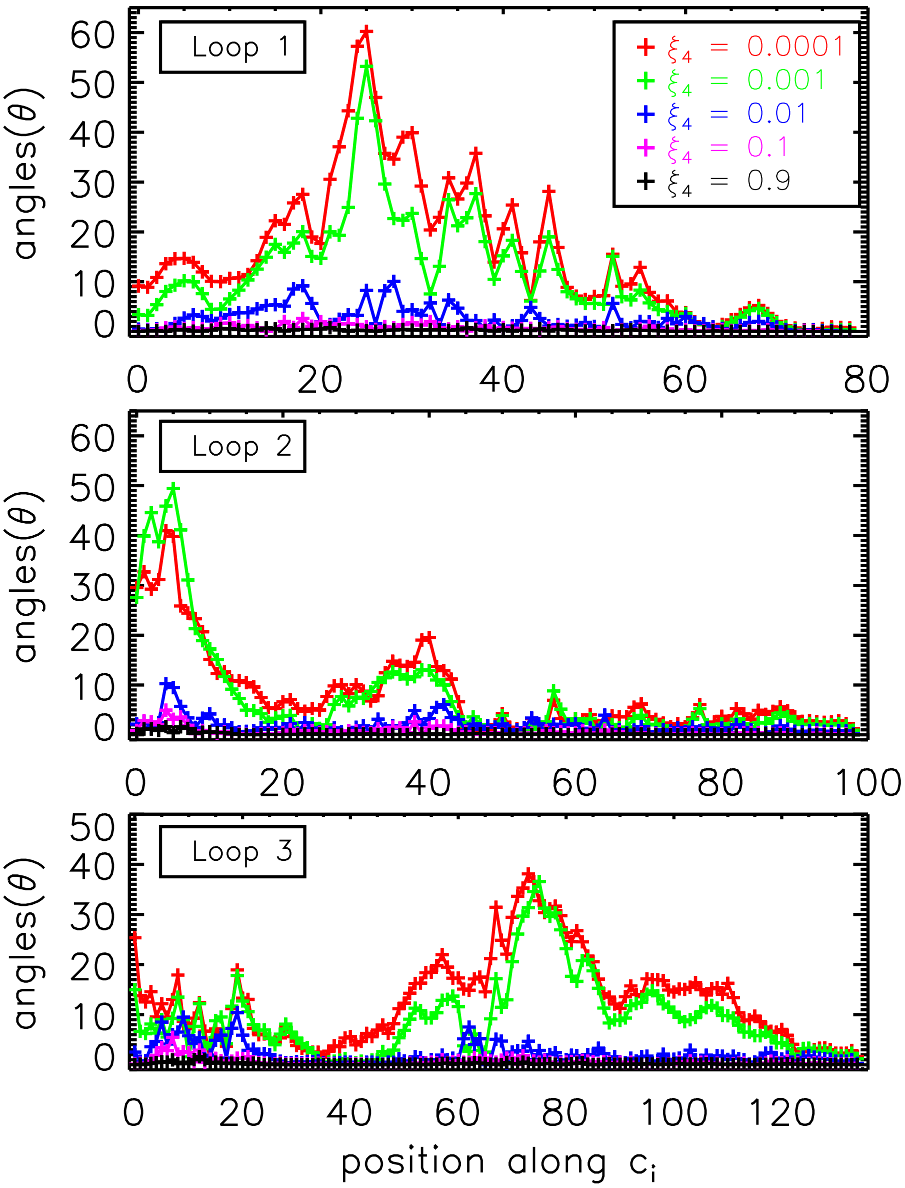

Figure 5.7: The angles $\theta_i(s)$ between tangent of the *consistent loop* $i = 1, 2, 3$ and the interpolated magnetic field $\overline{\mathbf{B}}(\mathbf{c}(s))$ at curve parameter s along the loop. The different colors represent the angles for magnetic field models obtained with different regularization parameters ξ_4 =0.9 (black), 0.1 (cyan), 0.01 (blue), 0.001 (green) and 0.0001 (red).

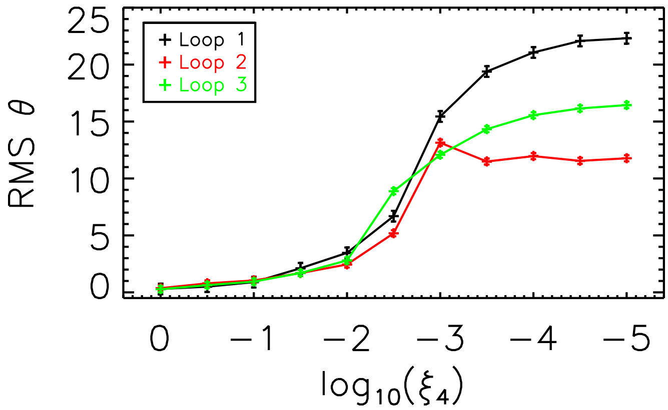

Figure 5.8: Dependence of the root mean square of the angles θ between the loop tangent and the local field direction along each of the three *consistent loops* with ξ_4.

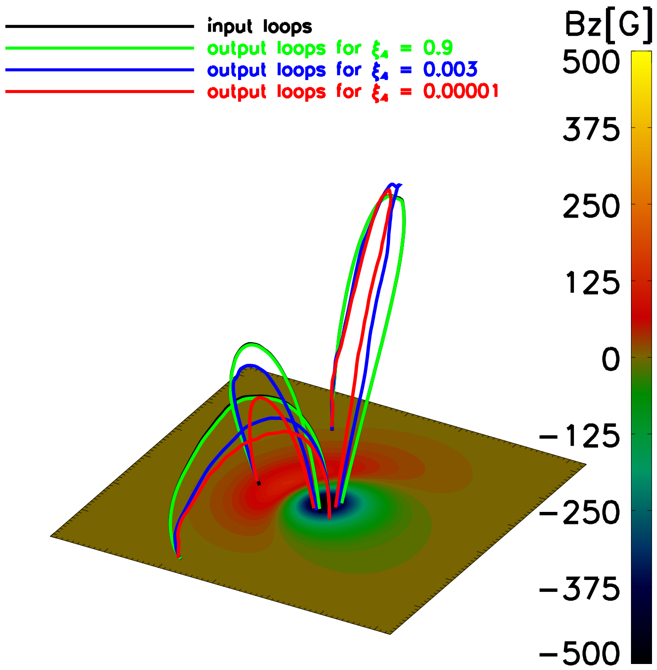

Figure 5.9: Plot of the initial loops (black) used as input data and of output loops for $\xi_4 = 0.9$ (green), for $\xi_4 = 0.003$ (blue) and for $\xi_4 = 0.00001$ (red).

In Table 5.1 we present figures of merit commonly used in the evaluation of nonlinear force free field models. They are the vector correlation (VC), Cauchy-Schwartz (CS), the normalized vector error (E_n) and the mean vector error (E_m) (Schrijver et al. 2006). Vector correlation (VC) evaluates how well two vector fields are correlated and is given by

$$VC = \frac{\sum_i \tilde{\mathbf{B}}_\mathbf{i}(\xi_4) \cdot \mathbf{b_i}}{\left(\sum_i |\tilde{\mathbf{B}}_\mathbf{i}(\xi_4)|^2 \sum_i |\mathbf{b_i}|^2\right)^{1/2}} . \tag{5.6}$$

Table 5.1: The dependence of VC, CS, E_m and E_n with ξ_4 for the analytical field 1.

ξ_4	VC	CS	E_m	E_n
10.0000	0.9614	0.8981	0.3521	0.3598
5.00000	0.9647	0.9039	0.3392	0.3502
2.00000	0.9724	0.9153	0.3035	0.3286
0.90000	0.9844	0.9369	0.2321	0.2654
0.30000	0.9842	0.9351	0.2348	0.2699
0.10000	0.9842	0.9354	0.2348	0.2788
0.03000	0.9838	0.9348	0.2373	0.2713
0.01000	0.9836	0.9352	0.2382	0.2705
0.00300	0.9838	0.9342	0.2382	0.2735
0.00100	0.9834	0.9349	0.2389	0.2698
0.00030	0.9837	0.9345	0.2373	0.2698
0.00010	0.9835	0.9327	0.2400	0.2748
0.00003	0.9835	0.9323	0.2403	0.2761
0.00001	0.9833	0.9322	0.2412	0.2765
0.00000	0.9833	0.9319	0.2416	0.2775

Here $\mathbf{b}$ is the NLFFF field model when the exact Low and Lou solution is used as magnetogram input , $\tilde{\mathbf{B}}(\xi_4)$ is the S-NLFFF field model, when the Low and Lou magnetogram perturbed by noise is used. Here, i sums over the N grid points in the computational domain.

Cauchy-Schwartz (CS) metric evaluates only the angle between the two vector fields and is given by

$$CS \equiv \frac{1}{N}\sum_i \frac{\tilde{\mathbf{B}}_\mathbf{i}(\xi_4)\cdot\mathbf{b}_\mathbf{i}}{|\tilde{\mathbf{B}}_\mathbf{i}(\xi_4)||\mathbf{b}_\mathbf{i}|} \equiv \frac{1}{N}\sum_i \cos\gamma_i\,, \tag{5.7}$$

where N is the total number of vector element and γ_i is the angle between any two vectors, $\tilde{\mathbf{B}}_\mathbf{i}(\xi_4)$ and $\mathbf{b}_\mathbf{i}$, at point i. The CS metric is unity when the two vectors are parallel, -1 when $\tilde{\mathbf{B}}_\mathbf{i}(\xi_4)$ and $\mathbf{b}_\mathbf{i}$ are anti-parallel and CS is zero when the two vectors are on average perpendicular to each other.

Two other metrics are the average vector norm (E_n) and the mean vector error (E_m), defined by:

$$E_n = \frac{\sum_i |\mathbf{b}_\mathbf{i} - \tilde{\mathbf{B}}_\mathbf{i}(\xi_4)|}{\sum_i |\tilde{\mathbf{B}}_\mathbf{i}(\xi_4)|}\,, \tag{5.8}$$

$$E_m = \frac{1}{N}\sum_i \frac{|\mathbf{b}_\mathbf{i} - \tilde{\mathbf{B}}_\mathbf{i}(\xi_4)|}{|\tilde{\mathbf{B}}_\mathbf{i}(\xi_4)|}\,. \tag{5.9}$$

$E_n = E_m = 0$ means the two vector fields are identical.

In Fig. 5.8 the root mean square angle is shown between the loop tangents and the local magnetic field $\overline{\mathbf{B}}$ interpolated at the respective position $\mathbf{c}_i(s_j)$. For the optimal value $\xi_4 = 0.90$ of the regularization parameter, the root mean square angle is well below 1 degree. The maximum absolute deviation of the local field from the loop tangent is 2.1 degrees which is of the order of the *standard angle error* introduced above. These norms also include angles close to the foot points where the field if extrapolated without the loop data, i.e. for $\xi_4 = 10^{-5}$, is varying heavily due to the influence of the noisy boundary data. Therefore the root mean square angle for $\xi_4 = 10^{-5}$ in Fig. 5.8 is strongly enhanced. The field extrapolated from the noisy boundary data makes in this case an average angle of up to 20 degrees with the consistent loop direction.

In Fig. 5.10 we display the dependence of the terms $Ł_i^\infty$ with ξ_4.

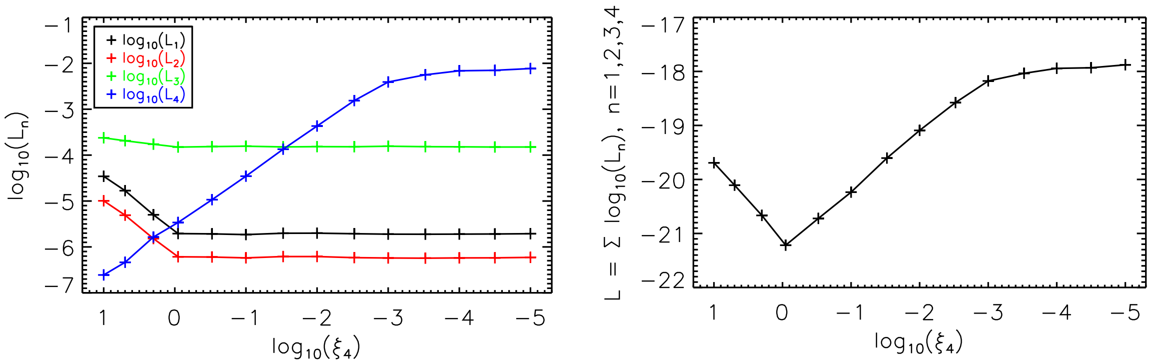

Figure 5.10: The left panel shows the dependence of $\log Ł_1^\infty$ (black), $\log Ł_2^\infty$ (red), $\log Ł_3^\infty$ (green) and $\log Ł_4^\infty$ (blue) with $\log \xi_4$ for noisy bottom data and consistent loop data. The right panel shows the dependence of $\sum_i \log Ł_i^\infty$ with $\log \xi_4$ for noisy bottom data and consistent loop data. The position of the minimum is assumed to yield the optimal value for ξ_4.

Probably due to the influence of the boundary noise in the regions not accessed by the three loops, the extrapolated field there has larger gradients than the standard field, so that the terms $Ł_1^\infty$ and $Ł_2^\infty$ measuring the residual forces and divergence which are about a factor 7-10 larger than for the noiseless reference field. These values hardly depend on ξ_4 as long as $\xi_4 \leq 1$ probably because the region influenced by the loops is small compared to the total computational volume. Definitely, for the different ξ_4 values chosen (Fig. 5.10), different field solutions were produced (see Fig. 5.9). Their variation however, has little effect on the terms $Ł_1^\infty$, $Ł_2^\infty$ and $Ł_3^\infty$. This shows that small changes in the magnetogram boundary produces different field lines at some distance from the surface. This sensitivity is only constrained by the new term $Ł_4^\infty$ as shown by its variation in Fig. 5.10.

Also the boundary data term $Ł_3^\infty$ hardly depends on ξ_4 in this particular test because the noise level chosen here is high and even with $\xi_4 = 0$ a force-free magnetic field cannot be fitted to the boundary data to make $\log Ł_3^\infty$ drop below about -0.2. However, as expressed already by the root mean square angle, we can effectively align the field along the loop depending on how strongly we shift the emphasis onto the loop term $Ł_4$ by varying ξ_4. The optimal ξ_4 is again close to unity.

5.2.2 Testing the method for Case II

For the second Low and Lou semi-analytical force-free field solution (see the introduction of the Section 5.2 for the configuration of the field) we only performed the test for the case

when a solution is perturbed by noise. We applied random noise to the boundary data in the same manner as for the analytical field 1. The noisy boundary data together with the *consistent loops* were used as input to the S_NLFFF code for different ξ_4 values. The test was applied only for the noisy magnetogram because it represents a case more close to the real situation. We want to show here that, if we use more loops and a more complicated configuration of the field, we still obtain good results as shown below.
In Fig. 5.11 we show the noisy boundary data and the *consistent loops* used as input for S-NLFFF model for different ξ_4 values. For this test case we have chosen ten *consistent loops*.

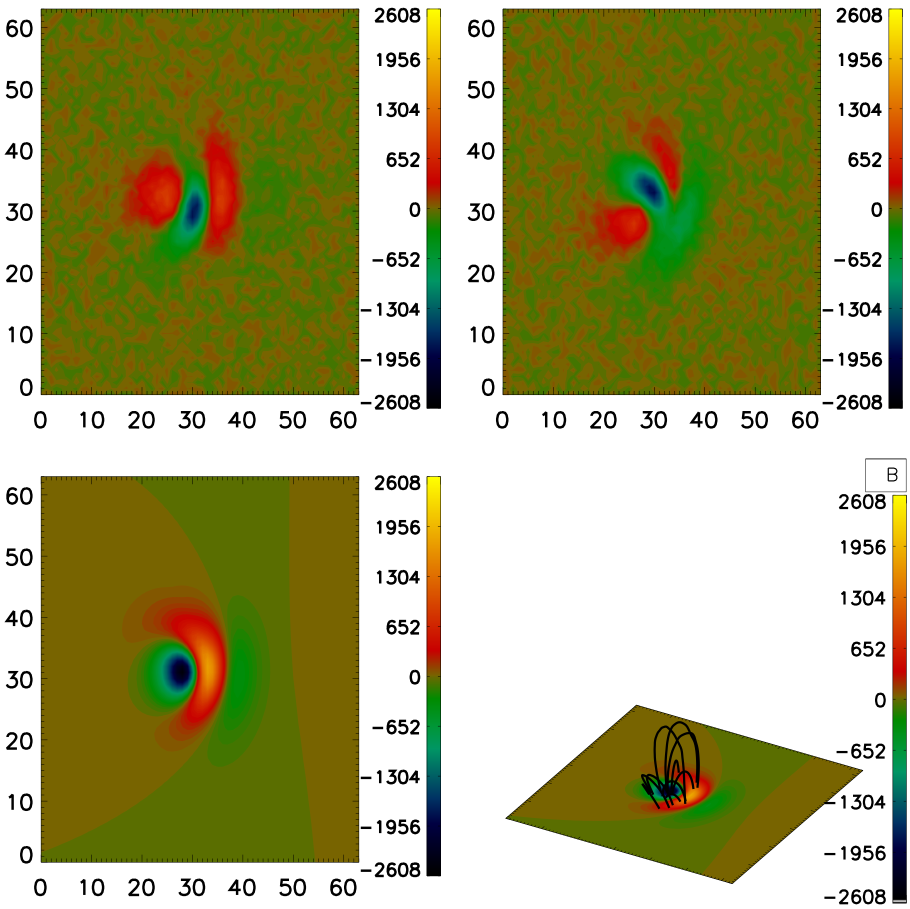

Figure 5.11: The three Cartesian components of the Low & Lou synthetic magnetogram The top row shows the B_x (left) and B_y (right) components, the bottom row the B_z (left) component and an oblique view on the B_z magnetogram with the ten loops extracted for our tests.

We try to find again the best solution for the functional $Ł_{tot}$ with ξ_4. For this test case we varied ξ_4 in the interval 10^{-5} to 1. In Fig. 5.12, left panel, we plot the variation of each term $Ł_i^{\infty}$ with ξ_4 on a logarithmic scale and the right panel shows the same for the sum of $\log Ł_i^{\infty}$.

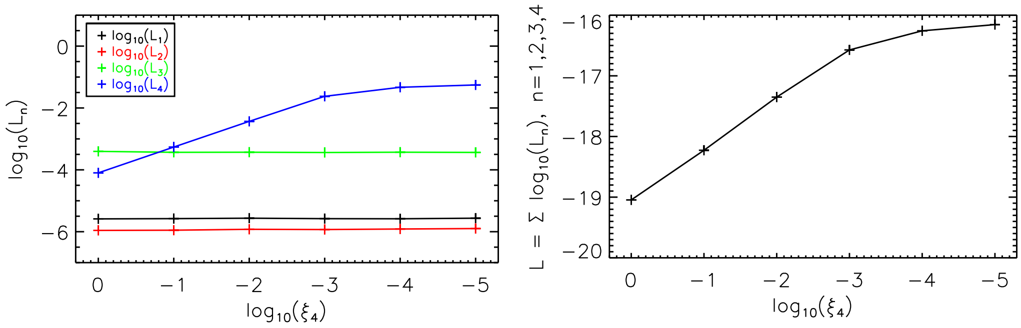

Figure 5.12: The left panel shows the dependence of $\log Ł_1^\infty$ (black), $\log Ł_2^\infty$ (red), $\log Ł_3^\infty$ (green) and $\log Ł_4^\infty$ (blue) with $\log \xi_4$ for noisy bottom data and consistent loop data. The right panel shows the dependence of $\sum_i \log Ł_i^\infty$ with $\log \xi_4$ for noisy bottom data and consistent loop data. The position of the minimum is supposed to yield the optimal value for ξ_4.

Like in the Case I, the values of the force-free terms ($Ł_1^\infty$ and $Ł_2^\infty$) and boundary term ($Ł_3^\infty$) vary slightly with ξ_4 and $Ł_4$ decreases with ξ_4. The minimum value of $\sum_i \log Ł_i^\infty$ from Fig. 5.12 (right side) again occurs at the optimum value for $\xi_4 = 0.9$.
In Table 5.2 we display the output values of the force-free term ($Ł_1^\infty$), the divergence free term ($Ł_2^\infty$), the lower boundary term ($Ł_3^\infty$) and the loop term ($Ł_4^\infty$).

Table 5.2: The dependence of $Ł_1^\infty$, $Ł_2^\infty$, $Ł_3^\infty$ and $Ł_4^\infty$ with each ξ_4 for the analytical field 2.

ξ_4	$Ł_1^\infty$	$Ł_2^\infty$	$Ł_3^\infty$	$Ł_4^\infty$
0.90000	0.3401	0.1441	1.6179	0.0280
0.10000	0.3467	0.1463	1.5077	0.1918
0.01000	0.3582	0.1564	0.5180	1.2977
0.00100	0.3456	0.1538	0.4874	8.3740
0.00010	0.3430	0.1599	1.5189	16.4119
0.00001	0.3581	0.1654	1.4978	19.5104
0.00000	0.3518	0.1637	1.4976	0.00000

The quality of the extrapolated field **B** is again measured by the figures of merit (5.6) - (5.8) where as reference we use again the field **b** which is obtained from the exact Low & Lou boundary values. The obtained values of the four terms (VC, CS, E_m, E_n) as a function of ξ_4 are presented in table 5.3. For $\xi_4 = 0.9$ we again obtain the best solutions for these metrics.

Table 5.3: The dependence of VC, CS, E_m and E_n with each ξ_4 for the analytical field 2.

ξ_4	VC	CS	E_m	E_n
0.90000	0.9907	0.8512	0.2920	0.5224
0.10000	0.9884	0.8297	0.3253	0.5875
0.01000	0.9876	0.8338	0.3324	0.5762
0.00100	0.9872	0.8305	0.3527	0.6132
0.00010	0.9877	0.8386	0.3463	0.5901
0.00001	0.9876	0.8358	0.3505	0.6009

The optimum $\xi_4 = 0.9$ can be found also in the evaluation of the angles between the loop tangents and the interpolated magnetic field at the loop points. Fig. 5.13 shows the root mean square of the angles (θ_i) with $\log \xi_4$ for each of the ten loops used as input.

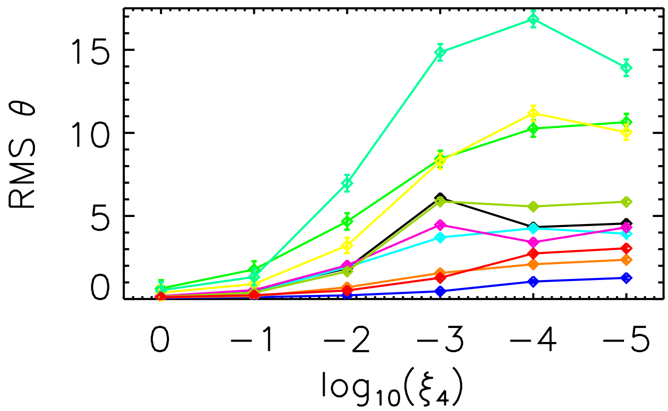

Figure 5.13: Dependence of the root mean square of the angles θ between the loop tangent and the local field direction along each of the ten *consistent loops* with ξ_4.

Finally, we check whether the new term can help to improve the magnetic field model beyond what we can achieve with the noisy boundary data alone. We define three different sub-volumes inside the computational box (SV_1, SV_2, SV_3). SV_1 is the union of the smallest possible quadrilateral boxes around each loop with edges in x, y, z direction. $SV_{2,3}$ comprise the same boxes with edge lengths enhanced by a factor k equal 1.25 and 1.5, respectively. The edges of the smallest quadrilateral around one loop is defined as $\tilde{x}^{(1)}_{min} = \min_s(c_i(s) \cdot \hat{e}_x)$ and similarly for the y and z components.

Then the enhanced boxes SV_j, $j = 1, 2, 3$ are:

$$\tilde{x}^j_{min} = \left[\tilde{x}^{(1)}_{min} - \frac{1}{2}\left(\tilde{x}^{(1)}_{max} + \tilde{x}^{(1)}_{min}\right)\right] k_j + \frac{1}{2}\left(\tilde{x}^{(1)}_{max} + \tilde{x}^{(1)}_{min}\right) , \tag{5.10}$$

$$\tilde{x}^j_{max} = \left[\tilde{x}^{(1)}_{max} - \frac{1}{2}\left(\tilde{x}^{(1)}_{max} + \tilde{x}^{(1)}_{min}\right)\right] k_j + \frac{1}{2}\left(\tilde{x}^{(1)}_{max} + \tilde{x}^{(1)}_{min}\right) , \tag{5.11}$$

$$k_j = \{1, 1.25, 1.5\} \text{ for } j = 1, 2, 3, \text{ respectively} .$$

The $\tilde{y}^j_{min}, \tilde{y}^j_{max}$ and $\tilde{z}^j_{min}, \tilde{z}^j_{max}$ edges are found in the same manner as $\tilde{x}^j_{min}, \tilde{x}^j_{max}$. The sub-volume SV_j is given by

$$SV_1 = [\tilde{x}^j_{min}, \tilde{x}^j_{max}] \times [\tilde{y}^j_{min}, \tilde{y}^j_{max}] \times [\tilde{z}^j_{min}, \tilde{z}^j_{max}] . \tag{5.12}$$

In Fig. 5.14 we show the boxes SV_j and how they are arranged relative to the loops.

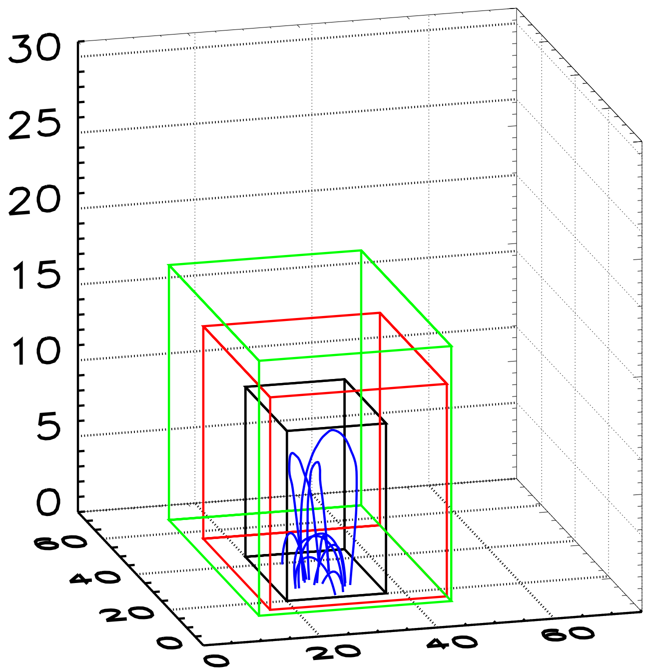

Figure 5.14: The average vector difference between S-NLFFF and NLFFF output magnetic field with $\log \xi_4$.

In Fig. 5.15, we display the average error of the extrapolated field

$$< \delta\mathbf{B} >=< \tilde{\mathbf{B}}(\xi_4) - \mathbf{b} > , \tag{5.13}$$

calculated inside the three sub-volumes (SV_1 - black asterisk, SV_2 - red asterisk, SV_3 - green asterisk) for different values of ξ_4.

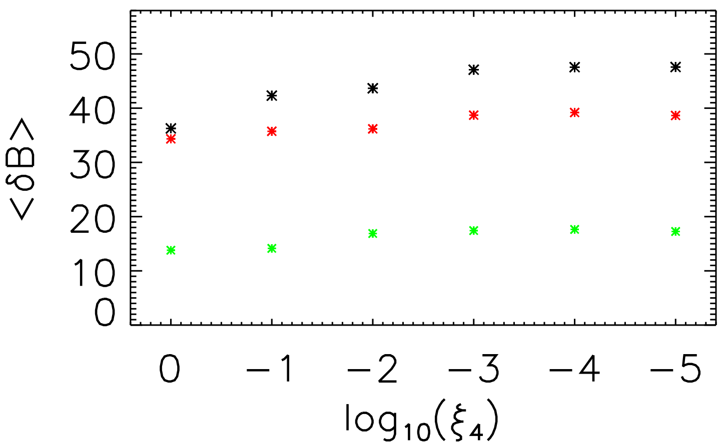

Figure 5.15: The average vector difference between S-NLFFF and NLFFF output magnetic field with $\log \xi_4$.

Even if we have used ten loops, the improvement of the field model by the new term is relatively small if the optimal value of $\xi_4 = 1$ is used. These ten field lines impact only a small subvolume (0.26%) of the total computational box. The reference field here is a gain the extrapolation for ideal boundary data unperturbed by noise. For this case, ξ_4 can be set to zero because the loop data is unnecessary for ideal boundary data. In Eq. (5.13), $\tilde{\mathbf{B}}(\xi_4)$ is the magnetic field model obtained from the S-NLFFF extrapolation code when the noisy magnetogram and the correct loops are used as input.

For each of the boxes the error slightly decreases with increasing ξ_4. The improvement with the new term is most pronounced for the smallest box and only marginal for the biggest box. We conclude that forcing the field into the right direction along the loop improves the field only in the immediate neighborhood of the loop. Moreover the term Ł$_4$ only influences the direction, not the magnitude of the magnetic field at the loop point. Part of the error $< \delta\mathbf{B} >$ is due to magnitude deviation between $\mathbf{B}(\xi_4)$ and $\mathbf{b}$.

5.3 Discussions and conclusions

We have proposed a new algorithm to improve the magnetic field model obtained from force-free field extrapolations of photospheric vector magnetogram data. The new feature of the procedure is to incorporate the information of field-aligned loops obtained from EUV image pairs and processed by stereoscopy to 3D curves.

If the magnetogram data is exact and the loop data are consistent, we find that the algorithm produces the unique solution as expected. In this theoretical case, the correct solution is also obtained even if the loop data is omitted. In most practical cases it can however not be expected that the magnetogram data or the loop reconstruction are without errors. We have tested these situations in which the two data sets are not entirely consistent. We found that for realistic error amplitudes we can achieve a good alignment of the magnetic model field with the loop curves without deteriorating the level of force-freeness. If these errors are present, it turns out that a whole set of force-free fields is possible as solution with slightly different fields at the lower boundary which deviate from the magnetogram data within a typical measurement error. In these cases the additional loop information constrains the solution effectively and from all solutions possible, we obtain the one which is best aligned with the imposed loop shapes.

The conclusion that noisy data allows multiple solutions if small deviations are allowed between the magnetogram data and the lower boundary of the model field can also be drawn from the results of the paper of De Rosa et al. (2009). All NLFFF codes produced model fields which closely matched the observed magnetogram data, but they were mutually different at larger altitudes and differed from the 3D loop shapes derived from stereoscopy. We attribute this deficiency to the ill-posedness of the boundary value problem: little noise in the magnetogram data may cause changes in the solution especially at larger distances from the surface. From our tests, this is demonstrated by the fact that we can modify the solution within some bounds by choosing different values for the regularization parameter ξ_4 without much affecting the force-freeness, divergence-freeness or the boundary data error. The new variational term we introduce makes use of this freedom in order to align the model field with the loop shapes.

Using the regularization parameter ξ_4, we can allow either the magnetogram or the loop data to gain more influence on the final solution without significantly affecting the vanishing of the divergence or the Lorentz force. If both data terms are properly normalized by their measurement error, $\xi_4 \simeq 1$ turns out to be the optimal value. In the cases tested, the angles of the local field to the field line direction could then be reduced to less than a degree on average.

6 Summary and outlook

The focus of this thesis is to study the reconstruction of different objects in the solar corona using data from different spacecraft. The objects studied were prominences, coronal loops and coronal mass ejections. We have used images in the EUV wavelength $\lambda = 304\text{Å}$ and in white light (coronographic) from the SDO and the STEREO A and B spacecraft.

With our MBSR method we performed a 3D reconstruction using data from two and three view directions. We have applied MBSR from two view directions to a CME core which showed an exceptionally low polarization. With MBSR we identified the correct 3D location of the low polarized patch well inside the CME. This way we could exclude that the bright core signal was produced by Thomson scattering, but it is consistent with intense resonant scattering of the Hα line.

Another application of MBSR, this time using data from three spacecraft, was the reconstruction of an eruptive prominence, which triggered a CME. Using MBSR we could see the evolution of these two phenomena. We analyzed their kinematics and morphology within some limitations. One of the limitations was that our method is suitable for the reconstruction of curve-like shapes, whereas the CME is a voluminous object bounded by surfaces. We were therefore only able to extract the visible leading edge of the CME. Another limitation relates to the use of data from a varying number of viewpoints. As the MBSR code is written now, a loop has to be reconstructed separately on each curve section which is seen from different numbers of view directions. In principle, this separation is unnecessary and it should be abolished in future versions of the code.

Our third project aimed at an improvement of magnetic field extrapolations of magnetograms from the solar surface using the shape information of coronal loops reconstructed by stereoscopy. Conventional extrapolation models of coronal magnetic field often show a disagreement between the observed magnetic field and the shape of coronal loops. With our model S-NLFFF we try to reconcile the coronal magnetic field model with observed coronal loops by closely as possible. We have tested the model with synthetic magnetograms and loops with special emphasis on whether inconsistencies in the magnetograms could be compensated by the additional loop data.

Our algorithm still has to be applied to real data. An investigation of this kind is underway. Applying our algorithm to real data implies the following steps:

1. processing the EUVI images from the STEREO and/or the SDO spacecraft. The low spatial resolution of the STEREO telescopes makes it difficult the to identify coronal loops correctly in the images. On top of that, the instrument noise adds to the difficulty of loop identification. The images have to be cleaned from the noise, contrast must be enhanced to have a balance in luminosity. There are some

methods which can improve the quality of an image, like wavelet transform. We are planning to apply a better image processing in order to obtain a better and easier identification of different coronal magnetic loops.

2. 3D reconstruction of couple of active region loops using our Multi-view B-spline Stereoscopic Reconstruction method.

3. preprocessing the vector magnetograms provided by the SDO spacecraft.

4. using S-NLFFF code to model the coronal magnetic field with the 3D information of loop curves and the vector magnetogram as input data.

Provided that all the data are available, we are confident that we will be able to produce a more reliable force-free magnetic field model for the corona than with conventional tools.

In many cases, a vector photospheric magnetogram and two simultaneous solar EUV images are not available. We therefore intend to modify our code to also cope with the case when the field extrapolation is constrained just by the loop projection from one EUV image only. This is a more difficult approach since we will not have the full 3D loop information available.

A Appendix

In order to determine the position of the 3D object we need to find α_1 and α_2 (see Eq. 2.11) from the two distances σ_i (Fig. A.1) along the epipolar line in the respective image. First we have the edge length of the similar triangles OAB and OA'B' from Fig. (A.1):

$$\frac{\sigma_i}{f'} = \frac{\overline{A'B'}}{\overline{A'O}} = \frac{(\mathbf{\Delta r} - z\hat{\mathbf{\Omega}}) \cdot \hat{\tilde{\mathbf{e}}}_\mathbf{i}}{|\tilde{r}_i| - a - b} \tag{A.1}$$

The distance from the observer to the Sun center $|\tilde{r}_i|$ and the epipolar directions in each image $\hat{\tilde{\mathbf{e}}}_\mathbf{i}$ are known from the position of both the spacecraft and z, the epipolar plane parameter (defined in Eq. 2.15). The image axis along the epipolar line is defined as

$$\hat{\tilde{\mathbf{e}}}_\mathbf{i} = \frac{\hat{\mathbf{n}}(z) \times \mathbf{r}_i}{|\hat{\mathbf{n}}(z) \times \mathbf{r}_i|} \tag{A.2}$$

where $\hat{\mathbf{n}}(z)$ is the epipolar normal and $\mathbf{r}_i$ is the spacecraft position.

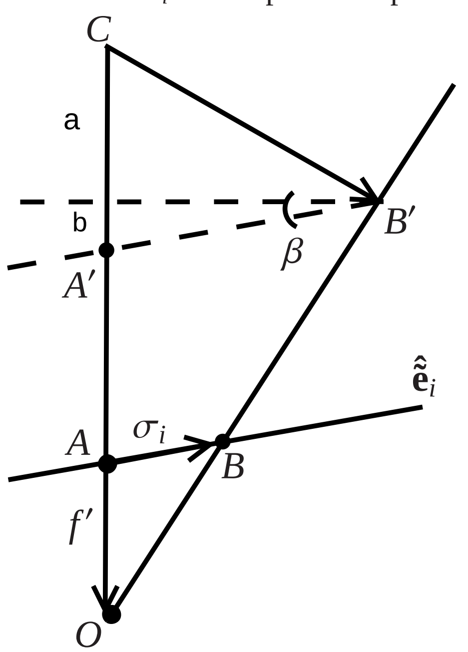

Figure A.1: Reconstruction of a point with projective geometry in the epipolar plane. The vectors $\mathbf{\Delta r}$, $z\hat{\mathbf{\Omega}}$, $\tilde{r}_i$ all lie in the same epipolar plane marked by points B'CO.

From Fig. A.2 we can see that

$$f' = \frac{f}{\sqrt{1 + (z/r_i)^2}} \tag{A.3}$$

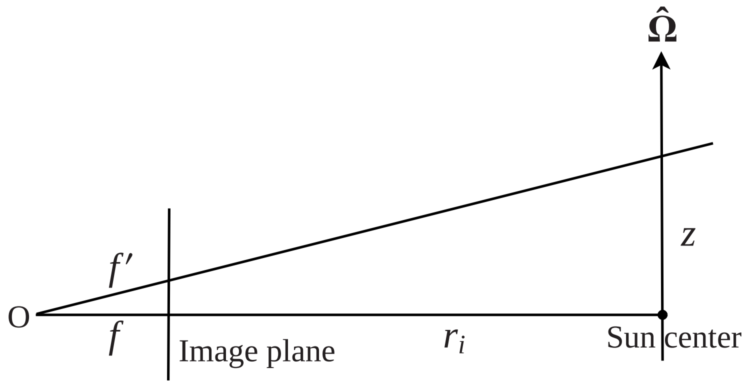

Figure A.2: Reconstruction of a point with projective geometry in the epipolar plane

is a small correction to the focal length where for typical observations $z/r_i \lesssim 1/200$.

The formula (A.1) takes account of fact that $\tilde{\mathbf{e}}_\mathbf{i}$ is not perpendicular to $\tilde{\mathbf{r}}_\mathbf{i}$. From Fig. A.1 we have

$$a = (\mathbf{\Delta r} - z\hat{\mathbf{\Omega}}) \cdot \hat{\tilde{\mathbf{r}}}_\mathbf{i} \tag{A.4}$$

$$\begin{aligned} b &= (\mathbf{\Delta r} - z\hat{\mathbf{\Omega}}) \cdot \hat{\tilde{\mathbf{e}}}_\mathbf{i} \sin\beta \\ &= -[(\mathbf{\Delta r} - z\hat{\mathbf{\Omega}}) \cdot \hat{\tilde{\mathbf{e}}}_\mathbf{i}](\hat{\tilde{\mathbf{e}}}_\mathbf{i} \cdot \hat{\tilde{\mathbf{r}}}_\mathbf{i}) \end{aligned} \tag{A.5}$$

Inserting Eq. (A.4) and (A.5) in Eq. (A.1) brings us to the following expression

$$\frac{\sigma_i}{f'} = \frac{\hat{\tilde{\mathbf{e}}}_\mathbf{i} \cdot (\mathbf{\Delta r} - z\hat{\mathbf{\Omega}})}{|\tilde{\mathbf{r}}_\mathbf{i}| - \hat{\tilde{\mathbf{r}}}_\mathbf{i}(1 - \hat{\tilde{\mathbf{e}}}_\mathbf{i}\hat{\tilde{\mathbf{e}}}_\mathbf{i})(\mathbf{\Delta r} - z\hat{\mathbf{\Omega}})} \tag{A.6}$$

Using Eq. (2.16), we can rewrite expression (A.6)

$$|\tilde{\mathbf{r}}_\mathbf{i}|\frac{\sigma_i}{f'} = \left[\hat{\tilde{\mathbf{e}}}_\mathbf{i} + \frac{\sigma_i}{f'}\hat{\tilde{\mathbf{r}}}_\mathbf{i}(1 - \hat{\tilde{\mathbf{e}}}_\mathbf{i}\hat{\tilde{\mathbf{e}}}_\mathbf{i})\right](\alpha_1\tilde{\mathbf{r}}_\mathbf{1} + \alpha_2\tilde{\mathbf{r}}_\mathbf{2}) \tag{A.7}$$

which is what we need to derive α_1 and α_2.

Bibliography

Amari, T., Aly, J.-J., Mikic, Z., Linker, J., 2010, Coronal Mass Ejection Initiation: On the Nature of the Flux Cancellation Model, ApJ, 717, L26–L30

Antiochos, S. K., DeVore, C. R., Klimchuk, J. A., 1999, A Model for Solar Coronal Mass Ejections, ApJ, 510, 485–493

Antunes, A., Thernisien, A., Yahil, A., 2009, Hybrid Reconstruction to Derive 3D Height - Time Evolution for Coronal Mass Ejections, Sol. Phys., 259, 199–212

Anzer, U., Heinzel, P., 2005, On the Nature of Dark Extreme Ultraviolet Structures Seen by SOHO/EIT and TRACE, ApJ, 622, 714–721

Anzer, U., Heinzel, P., 2008, Prominence modelling: from observed emission measures to temperature profiles, A&A, 480, 537–542

Arregui, I., Oliver, R., Ballester, J. L., 2012, Prominence Oscillations, Living Reviews in Solar Physics, 9, 2

Artzner, G., Gosain, S., B., S., 2010, A Technique for Removing Background Features in SECCHI – EUVI He II 304 Å Filtergrams: Application to the Filament Eruption of 22 May 2008, Sol. Phys., 262, 437–447

Aschwanden, M. J., 2004, Physics of the Solar Corona. An Introduction, Berlin:Springer

Aschwanden, M. J., 2011, Solar Stereoscopy and Tomography, Living Reviews in Solar Physics, 8, 5

Aschwanden, M. J., Wülser, J.-P., Nitta, N. V., Lemen, J. R., 2008, First Three-Dimensional Reconstructions of Coronal Loops with the STEREO A and B Spacecraft. I. Geometry, ApJ, 679, 827–842

Aulanier, G., Török, T., Démoulin, P., DeLuca, E. E., 2010, Formation of Torus-Unstable Flux Ropes and Electric Currents in Erupting Sigmoids, ApJ, 708, 314–333

Bastian, T. S., Gary, D. E., 1997, On the feasibility of imaging coronal mass ejections at radio wavelengths, J. Geophys. Res., 102, 14 031–14 040

Bemporad, A., Mierla, M., Tripathi, D., 2011, Rotation of an erupting filament observed by the STEREO EUVI and COR1 instruments, A&A, 531, A147

Billings, D. E., 1966, A guide to the solar corona, New York: Academic Press

Bothmer, V., Daglis, I. A., 2007, Radiation belts and ring current, Berlin:Springer

Brueckner, G. E., Howard, R. A., Koomen, M. J., Korendyke, C. M., Michels, D. J., Moses, J. D., Socker, D. G., Dere, K. P., Lamy, P. L., Llebaria, A., Bout, M. V., Schwenn, R., Simnett, G. M., Bedford, D. K., Eyles, C. J., 1995, The Large Angle Spectroscopic Coronagraph (LASCO), Sol. Phys., 162, 357–402

Brun, A. S., 2004, D MHD Simulations of the Solar Convection Zone and Tachocline, in SOHO 14 Helio- and Asteroseismology: Towards a Golden Future, (Ed.) D. Danesy, vol. 559 of ESA Special Publication, p. 271

Cargill, P. J., 2004, On the Aerodynamic Drag Force Acting on Interplanetary Coronal Mass Ejections, Sol. Phys., 221, 135–149

Chae, J., Ahn, K., Lim, E.-K., Choe, G. S., Sakurai, T., 2008, Persistent Horizontal Flows and Magnetic Support of Vertical Threads in a Quiescent Prominence, ApJ, 689, L73–L76

Charbonneau, P., 2010, Dynamo Models of the Solar Cycle, Living Reviews in Solar Physics, 7, 3

Charbonneau, P., Christensen-Dalsgaard, J., Henning, R., Larsen, R. M., Schou, J., Thompson, M. J., Tomczyk, S., 1999, Helioseismic Constraints on the Structure of the Solar Tachocline, ApJ, 527, 445–460

Chen, P. F., 2011, Coronal Mass Ejections: Models and Their Observational Basis, Living Reviews in Solar Physics, 8, 1

Chen, P. F., Shibata, K., 2000, An Emerging Flux Trigger Mechanism for Coronal Mass Ejections, ApJ, 545, 524–531

Chifu, I., Inhester, B., Mierla, M., Chifu, V., Wiegelmann, T., 2012, First 4D Reconstruction of an Eruptive Prominence Using Three Simultaneous View Directions, Sol. Phys., 281, 121–135

Colaninno, R. C., Vourlidas, A., 2009, First Determination of the True Mass of Coronal Mass Ejections: A Novel Approach to Using the Two STEREO Viewpoints, ApJ, 698, 852–858

Couvidat, S., Schou, J., Shine, R. A., Bush, R. I., Miles, J. W., Scherrer, P. H., Rairden, R. L., 2012, Wavelength Dependence of the Helioseismic and Magnetic Imager (HMI) Instrument onboard the Solar Dynamics Observatory (SDO), Sol. Phys., 275, 285–325

Cremades, H., Bothmer, V., 2004, On the three-dimensional configuration of coronal mass ejections, A&A, 422, 307–322

Crifo, F., Picat, J. P., Cailloux, M., 1983, Coronal transients - Loop or bubble, Sol. Phys., 83, 143–152

Daglis, I. A., 1999, The terrestrial ring current: origin, formation, and decay, Reviews of Geophysics, 37, 407–438 de Boor, C., 1985, A practical guide to splines, New York:Springer-Verlag New York Inc.

De Rosa, M. L., Schrijver, C. J., Barnes, G., Leka, K. D., Lites, B. W., Aschwanden, M. J., Amari, T., Canou, A., McTiernan, J. M., Régnier, S., Thalmann, J. K., Valori, G., Wheatland, M. S., Wiegelmann, T., Cheung, M. C. M., Conlon, P. A., Fuhrmann, M., Inhester, B., Tadesse, T., 2009, A Critical Assessment of Nonlinear Force-Free Field Modeling of the Solar Corona for Active Region 10953, ApJ, 696, 1780–1791

Dere, K. P., Brueckner, G. E., Howard, R. A., Koomen, M. J., Korendyke, C. M., Kreplin, R. W., Michels, D. J., Moses, J. D., Moulton, N. E., Socker, D. G., St. Cyr, O. C., Delaboudinière, J. P., Artzner, G. E., Brunaud, J., Gabriel, A. H., Hochedez, J. F., Millier, F., Song, X. Y., Chauvineau, J. P., Marioge, J. P., Defise, J. M., Jamar, C., Rochus, P., Catura, R. C., Lemen, J. R., Gurman, J. B., Neupert, W., Clette, F., Cugnon, P., van Dessel, E. L., Lamy, P. L., Llebaria, A., Schwenn, R., Simnett, G. M., 1997, EIT and LASCO Observations of the Initiation of a Coronal Mass Ejection, Sol. Phys., 175, 601–612

Dikpati, M., Gilman, P. A., 2009, Flux-Transport Solar Dynamos, Space Sci. Rev., 144, 67–75

Eddy, J. A., 1974, A Nineteenth-century Coronal Transient, A&A, 34, 235

Feng, L., Wiegelmann, T., Inhester, B., Solanki, S., Gan, W. Q., Ruan, P., 2007, Magnetic Stereoscopy of Coronal Loops in NOAA 8891, Sol. Phys., 241, 235–249

Feng, L., Inhester, B., Wei, Y., Gan, W. Q., Zhang, T. L., Wang, M. Y., 2012, Morphological Evolution of a Three-dimensional Coronal Mass Ejection Cloud Reconstructed from Three Viewpoints, ApJ, 751, 18

Filippov, B. P., Den, O. G., 2000, Prominence Height and Vertical Gradient in Magnetic Field, Astronomy Letters, 26, 322–327

Fisher, G. H., Fan, Y., Longcope, D. W., Linton, M. G., Pevtsov, A. A., 2000, The Solar Dynamo and Emerging Flux, Sol. Phys., 192, 119–139

Forbes, T. G., Linker, J. A., Chen, J., Cid, C., Kóta, J., Lee, M. A., Mann, G., Mikić, Z., Potgieter, M. S., Schmidt, J. M., Siscoe, G. L., Vainio, R., Antiochos, S. K., Riley, P., 2006, CME Theory and Models, p. 251

Foukal, P., 1990, Solar astrophysics, New York: Wiley-Interscience

Gary, D. E., Keller, C. U. (Eds.), 2004, Radio Observations of Coronal Mass Ejections, vol. 314 of Astrophysics and Space Science Library

Gary, G. A., 2001, Plasma Beta above a Solar Active Region: Rethinking the Paradigm, Sol. Phys., 203, 71–86

Gonzalez, W. D., Joselyn, J. A., Kamide, Y., Kroehl, H. W., Rostoker, G., Tsurutani, B. T., Vasyliunas, V. M., 1994, What is a geomagnetic storm?, J. Geophys. Res., 99, 5771–5792

Gopalswamy, N., 2010, Corona Mass Ejections: a Summary of Recent Results, in 20th National Solar Physics Meeting, (Ed.) I. Dorotovic, pp. 108–130

Gopalswamy, N., Yashiro, S., Akiyama, S., 2007, Geoeffectiveness of halo coronal mass ejections, Journal of Geophysical Research, 112, A06112

Gosain, S., Schmieder, B., 2010, Estimation of width and inclination of a filament sheet using He II 304 Å observations by STEREO/EUVI, Annales Geophysicae, 28, 149–153

Gosain, S., Schmieder, B., Venkatakrishnan, P., Chandra, R., Artzner, G., 2009, 3D Evolution of a Filament Disappearance Event Observed by STEREO, Sol. Phys., 259, 13–30

Gouttebroze, P., Heinzel, P., Vial, J. C., 1993, The hydrogen spectrum of model prominences, A&AS, 99, 513–543

Hansen, P. C., 2010, Discrete inverse problems insight and algorithms, Philadelphia:Society for Industrial and Applied Mathematics

Hartley, R., Zisserman, A., 2003, Multiple View Geometry in Computer Vision, Cambridge:Cambridge University Press

Hasted, J. B., 1964, Physics of atomic collisions, London: Butterworths

Hildner, E., Gosling, J. T., Hansen, R. T., Bohlin, J. D., 1975, The sources of material comprising a mass ejection coronal transient, Sol. Phys., 45, 363–376

Howard, R. A., Moses, J. D., Vourlidas, A., Newmark, J. S., Socker, D. G., Plunkett, S. P., Korendyke, C. M., Cook, J. W., Hurley, A., Davila, J. M., Thompson, W. T., St Cyr, O. C., Mentzell, E., Mehalick, K., Lemen, J. R., Wuelser, J. P., Duncan, D. W., Tarbell, T. D., Wolfson, C. J., Moore, A., Harrison, R. A., Waltham, N. R., Lang, J., Davis, C. J., Eyles, C. J., Mapson-Menard, H., Simnett, G. M., Halain, J. P., Defise, J. M., Mazy, E., Rochus, P., Mercier, R., Ravet, M. F., Delmotte, F., Auchere, F., Delaboudiniere, J. P., Bothmer, V., Deutsch, W., Wang, D., Rich, N., Cooper, S., Stephens, V., Maahs, G., Baugh, R., McMullin, D., Carter, T., 2008a, Sun Earth Connection Coronal and Heliospheric Investigation (SECCHI), Space Sci. Rev., 136, 67–115

Howard, R. A., Moses, J. D., Vourlidas, A., Newmark, J. S., Socker, D. G., Plunkett, S. P., et al., 2008b, Sun Earth Connection Coronal and Heliospheric Investigation (SECCHI), ßr, 136, 67–115

Howard, T. A., Tappin, S. J., 2008, Three-Dimensional Reconstruction of Two Solar Coronal Mass Ejections Using the STEREO Spacecraft, Sol. Phys., 252, 373–383

Illing, R. M. E., Hundhausen, A. J., 1986, Disruption of a coronal streamer by an eruptive prominence and coronal mass ejection, J. Geophys. Res., 91, 10 951–10 960

Inhester, B., 2006, Stereoscopy basics for the STEREO mission, ArXiv Astrophysics e-prints:arXiv:astro-ph/0612649v1

Inhester, B., Wiegelmann, T., 2006, Nonlinear Force-Free Magnetic Field Extrapolations: Comparison of the Grad Rubin and Wheatland Sturrock Roumeliotis Algorithm, Sol. Phys., 235, 201–221

Jejčič, S., Heinzel, P., 2009, Electron Densities in Quiescent Prominences Derived from Eclipse Observations, Sol. Phys., 254, 89–100

Joshi, A. D., Srivastava, N., 2011a, Kinematics of Two Eruptive Prominences Observed by EUVI/STEREO, ApJ, 730, 104

Joshi, A. D., Srivastava, N., 2011b, Kinematics of Two Eruptive Prominences Observed by EUVI/STEREO, ApJ, 730, 104

Kaiser, M. L., Kucera, T. A., Davila, J. M., St. Cyr, O. C., Guhathakurta, M., Christian, E., et al., 2007, The STEREO Mission: An Introduction, Space Sci. Rev., 136, 5–16

Klimchuk, J. A., 2009, Coronal Loop Models and Those Annoying Observations! (Keynote), in The Second Hinode Science Meeting: Beyond Discovery-Toward Understanding, (Eds.) B. Lites, M. Cheung, T. Magara, J. Mariska, K. Reeves, vol. 415 of Astronomical Society of the Pacific Conference Series, p. 221

Kuperus, M., Raadu, M. A., 1974, The Support of Prominences Formed in Neutral Sheets, A&A, 31, 189

Kuperus, M., Tandberg-Hanssen, E., 1967, The Nature of Quiescent Solar Prominences, Sol. Phys., 2, 39–48

Labrosse, N., Heinzel, P., Vial, J.-C., Kucera, T., Parenti, S., Gunár, S., Schmieder, B., Kilper, G., 2010, Physics of Solar Prominences: Spectral Diagnostics and Non-LTE Modelling, Space Sci. Rev., 151, 243–332

Landi, E., Young, P. R., Dere, K. P., Del Zanna, G., Mason, H. E., 2013, CHIANTI-An Atomic Database for Emission Lines. XIII. Soft X-Ray Improvements and Other Changes, ApJ, 763, 86

Leake, J. E., Linton, M. G., Antiochos, S. K., 2014, Simulations of Emerging Magnetic Flux. II: The formation of Unstable Coronal Flux Ropes and the Initiation of CMEs, ArXiv e-prints, 1402.2645

Lemen, J. R., et al., 2012, The Atmospheric Imaging Assembly (AIA) on the Solar Dynamic Observatory (SDO), Sol. Phys.

Lenz, D. D., 1999, Energetics and Structure of Multispecies Solar Coronal Loops, ApJ, 517, 497–509

Li, T., Zhang, J., Zhang, Y., Yang, S., 2011, Three-dimensional Reconstruction of an Erupting Filament with Solar Dynamics Observatory and STEREO Observations, ApJ, 739, 43

Liewer, P. C., Hall, J. R., Howard, R. A., de Jong, E. M., Thompson, W. T., Thernisien, A., 2011, Stereoscopic analysis of STEREO/SECCHI data for CME trajectory determination, J. of Atm. Solar-Terr. Phys., 73, 1173–1186

Linker, J. A., Mikić, Z., Riley, P., Lionello, R., Odstrcil, D., 2003, Models of Coronal Mass Ejections: A Review with A Look to The Future, in Solar Wind Ten, (Eds.) M. Velli, R. Bruno, F. Malara, B. Bucci, vol. 679 of American Institute of Physics Conference Series, pp. 703–710

Low, B. C., Lou, Y. Q., 1990, Modeling solar force-free magnetic fields, ApJ, 352, 343–352

Lynch, B. J., Antiochos, S. K., de Vore, C. R., Zurbuchen, T. H., 2005, The Breakout Model for CME Initiation in 3-Dimensions, in Solar Wind 11/SOHO 16, Connecting Sun and Heliosphere, (Eds.) B. Fleck, T. H. Zurbuchen, H. Lacoste, vol. 592 of ESA Special Publication, p. 297

Mackay, D. H., Karpen, J. T., Ballester, J. L., Schmieder, B., Aulanier, G., 2010, Physics of Solar Prominences: Magnetic Structure and Dynamics, Space Sci. Rev., 151, 333–399

Martin, S., 2000, Solar Prominence Formation, Encyclopedia of Astronomy and Astrophysics

Martin, S. F., 1990, Conditions for the formation of prominences as inferred from optical observations, in IAU Colloq. 117: Dynamics of Quiescent Prominences, (Eds.) V. Ruzdjak, E. Tandberg-Hanssen, vol. 363 of Lecture Notes in Physics, Berlin Springer Verlag, pp. 1–44

Martin, S. F., 1998, Conditions for the Formation and Maintenance of Filaments (Invited Review), Sol. Phys., 182, 107–137

Martin, S. F., Livi, S. H. B., Wang, J., 1985, The cancellation of magnetic flux. II - In a decaying active region, Australian Journal of Physics, 38, 929–959

Metcalf, T. R., Leka, K. D., Barnes, G., Lites, B. W., Georgoulis, M. K., Pevtsov, A. A., Balasubramaniam, K. S., Gary, G. A., Jing, J., Li, J., Liu, Y., Wang, H. N., Abramenko, V., Yurchyshyn, V., Moon, Y.-J., 2006, An Overview of Existing Algorithms for Resolving the 180 Ambiguity in Vector Magnetic Fields: Quantitative Tests with Synthetic Data, Sol. Phys., 237, 267–296

Mierla, M., Inhester, B., Marqué, C., Rodriguez, L., Gissot, S., Zhukov, A. N., Berghmans, D., Davila, J., 2009, On 3D Reconstruction of Coronal Mass Ejections: I. Method Description and Application to SECCHI-COR Data, Sol. Phys., 259, 123–141

Mierla, M., Inhester, B., Antunes, A., Boursier, Y., Byrne, J. P., Colaninno, R., Davila, J., de Koning, C. A., Gallagher, P. T., Gissot, S., Howard, R. A., Howard, T. A., Kramar, M., Lamy, P., Liewer, P. C., Maloney, S., Marqué, C., McAteer, R. T. J., Moran, T., Rodriguez, L., Srivastava, N., St. Cyr, O. C., Stenborg, G., Temmer, M., Thernisien, A., Vourlidas, A., West, M. J., Wood, B. E., Zhukov, A. N., 2010, On the 3-D reconstruction of Coronal Mass Ejections using coronagraph data, Annales Geophysicae, 28, 203–215

Mierla, M., Chifu, I., Inhester, B., Rodriguez, L., Zhukov, A., 2011, Low polarised emission from the core of coronal mass ejections, A&A, 530, L1

Mikić, Z., Lee, M. A., 2006, An Introduction to Theory and Models of CMEs, Shocks, and Solar Energetic Particles, Space Sci. Rev., 123, 57–80

Moran, T. G., Davila, J. M., 2004, Three-Dimensional Polarimetric Imaging of Coronal Mass Ejections, Science, 305, 66–71

Morgan, H., Habbal, S. R., 2007, The long-term stability of the visible F corona at heights of 3-6 R_sun, A&A, 471, L47–L50

Parenti, S., Vial, J.-C., 2007, Prominence and quiet-Sun plasma parameters derived from FUV spectral emission, A&A, 469, 1109–1115

Parenti, S., Schmieder, B., Heinzel, P., Golub, L., 2012, On the Nature of Prominence Emission Observed by SDO/AIA, ApJ, 754, 66

Park, H., Chae, J., Song, D., Maurya, R. A., Yang, H., Park, Y.-D., Jang, B.-H., Nah, J., Cho, K.-S., Kim, Y.-H., Ahn, K., Cao, W., Goode, P. R., 2013, Temperature of Solar Prominences Obtained with the Fast Imaging Solar Spectrograph on the 1.6 m New Solar Telescope at the Big Bear Solar Observatory, Sol. Phys., 288, 105–116

Parker, E. N., 1975, The generation of magnetic fields in astrophysical bodies. X - Magnetic buoyancy and the solar dynamo, ApJ, 198, 205–209

Patsourakos, S., Vourlidas, A., Kliem, B., 2010, Toward understanding the early stages of an impulsively accelerated coronal mass ejection. SECCHI observations, A&A, 522, A100

Pesnell, W. D., Thompson, B. J., Chamberlin, P. C., 2012, The Solar Dynamics Observatory (SDO), Sol. Phys., 275, 3–15

Peter, H., Bingert, S., Klimchuk, J. A., de Forest, C., Cirtain, J. W., Golub, L., Winebarger, A. R., Kobayashi, K., Korreck, K. E., 2013, Structure of solar coronal loops: from miniature to large-scale, A&A, 556, A104

Petrie, G. J. D., 2006, Coronal Loop Widths and Pressure Scale Heights, ApJ, 649, 1078–1083

Pevtsov, A. A., Balasubramaniam, K. S., Rogers, J. W., 2003, Chirality of Chromospheric Filaments, ApJ, 595, 500–505

Pizzo, V. J., Biesecker, D. A., 2004, Geometric localization of STEREO CMEs, Geophys. Res. Lett., 31, L21802

Poland, A. I., Munro, R. H., 1976, Interpretation of broad-band polarimetry of solar coronal transients - Importance of H-alpha emission, ApJ, 209, 927–934

Priest, E. R., 1982, Solar magneto-hydrodynamics, Dordrecht: D. Reidel

Reale, F., 2010, Coronal Loops: Observations and Modeling of Confined Plasma, Living Reviews in Solar Physics, 7

Schrijver, C. J., Siscoe, G. L., 2009, Heliophysics: Plasma Physics of the Local Cosmos, Cambridge:Cambridge University Press

Schrijver, C. J., Title, A. M., 2011, Long-range magnetic couplings between solar flares and coronal mass ejections observed by SDO and STEREO, J. Geophys. Res., 116, A04 108

Schrijver, C. J., De Rosa, M. L., Metcalf, T. R., Liu, Y., McTiernan, J., Régnier, S., Valori, G., Wheatland, M. S., Wiegelmann, T., 2006, Nonlinear Force-Free Modeling of Coronal Magnetic Fields Part I: A Quantitative Comparison of Methods, Sol. Phys., 235, 161–190

Schwenn, R., Raymond, J. C., Alexander, D., Ciaravella, A., Gopalswamy, N., Howard, R., Hudson, H., Kaufmann, P., Klassen, A., Maia, D., Munoz-Martinez, G., Pick, M., Reiner, M., Srivastava, N., Tripathi, D., Vourlidas, A., Wang, Y.-M., Zhang, J., 2006, Coronal Observations of CMEs. Report of Working Group A, Space Sci. Rev., 123, 127–176

Solanki, S. K., Inhester, B., Schüssler, M., 2006, The solar magnetic field, Reports on Progress in Physics, 69, 563–668

Stix, M., 2002, The sun: an introduction, Berlin:Springer

Syntelis, P., Gontikakis, C., Georgoulis, M. K., Alissandrakis, C. E., Tsinganos, K., 2012, Study of the Three-Dimensional Shape and Dynamics of Coronal Loops Observed by Hinode/EIS, Sol. Phys., 280, 475–489

Tadesse, T., Wiegelmann, T., Inhester, B., Pevtsov, A., 2011, Nonlinear force-free field extrapolation in spherical geometry: improved boundary data treatment applied to a SOLIS/VSM vector magnetogram, A&A, 527, A30

Tandberg-Hanssen, E., 1977, Prominences, in Illustrated Glossary for Solar and Solar-Terrestrial Physics, (Eds.) A. Bruzek, C. J. Durrant, vol. 69 of Astrophysics and Space Science Library, p. 97

Thalmann, J. K., Inhester, B., Wiegelmann, T., 2011, Estimating the Relative Helicity of Coronal Magnetic Fields, Sol. Phys., 272, 243–255

Thernisien, A., 2011, Implementation of the Graduated Cylindrical Shell Model for the Three-dimensional Reconstruction of Coronal Mass Ejections, ApJS, 194, 33

Thernisien, A., Vourlidas, A., Howard, R. A., 2009, Forward Modeling of Coronal Mass Ejections Using STEREO/SECCHI Data, Sol. Phys., 256, 111–130

Thernisien, A. F. R., Howard, R. A., Vourlidas, A., 2006, Modeling of Flux Rope Coronal Mass Ejections, ApJ, 652, 763–773

Thompson, W. T., 2006, Coordinate systems for solar image data, A&A, 449, 791–803

Thompson, W. T., Wei, K., Burkepile, J. T., Davila, J. M., St. Cyr, O. C., 2010, Background Subtraction for the SECCHI/COR1 Telescope Aboard STEREO, Sol. Phys., 262, 213–231

Török, T., Panasenco, O., Titov, V. S., Mikić, Z., Reeves, K. K., Velli, M., Linker, J. A., De Toma, G., 2011, A Model for Magnetically Coupled Sympathetic Eruptions, ApJ, 739, L63

Vaiana, G. S., Krieger, A. S., Timothy, A. F., 1973, Identification and Analysis of Structures in the Corona from X-Ray Photography, Sol. Phys., 32, 81–116

Valori, G., Kliem, B., Fuhrmann, M., 2007, Magnetofrictional Extrapolations of Low and Lou's Force-Free Equilibria, Sol. Phys., 245, 263–285

van Ballegooijen, A. A., Martens, P. C. H., 1989, Formation and eruption of solar prominences, ApJ, 343, 971–984

Vourlidas, A., Howard, R. A., Esfandiari, E., Patsourakos, S., Yashiro, S., Michalek, G., 2010, Comprehensive Analysis of Coronal Mass Ejection Mass and Energy Properties Over a Full Solar Cycle, ApJ, 722, 1522

Webb, D. F., Howard, T. A., 2012, Coronal Mass Ejections: Observations, Living Reviews in Solar Physics, 9, 3

Wheatland, M. S., Sturrock, P. A., Roumeliotis, G., 2000, An Optimization Approach to Reconstructing Force-free Fields, ApJ, 540, 1150–1155

Wiegelmann, T., 2004, Optimization code with weighting function for the reconstruction of coronal magnetic fields, Sol. Phys., 219, 87–108

Wiegelmann, T., Inhester, B., 2010, How to deal with measurement errors and lacking data in nonlinear force-free coronal magnetic field modelling?, A&A, 516, A107

Wiegelmann, T., Neukirch, T., 2003, Computing nonlinear force free coronal magnetic fields, Nonlinear Processes in Geophysics, 10, 313–322

Wiegelmann, T., Sakurai, T., 2012, Solar Force-free Magnetic Fields, Living Reviews in Solar Physics, 9, 5

Wiegelmann, T., Lagg, A., Solanki, S. K., Inhester, B., Woch, J., 2005, Comparing magnetic field extrapolations with measurements of magnetic loops, A&A, 433, 701–705

Wiehr, E., Bianda, M., 2003, Solar prominence polarimetry, A&A, 404, L25–L28

Winebarger, A. R., Schmelz, J. T., Warren, H. P., Saar, S. H., Kashyap, V. L., 2011, Using a Differential Emission Measure and Density Measurements in an Active Region Core to Test a Steady Heating Model, ApJ, 740, 2

Woods, T. N., Eparvier, F. G., Hock, R., Jones, A. R., Woodraska, D., Judge, D., Didkovsky, L., Lean, J., Mariska, J., Warren, H., McMullin, D., Chamberlin, P., Berthiaume, G., Bailey, S., Fuller-Rowell, T., Sojka, J., Tobiska, W. K., Viereck, R., 2012, Extreme Ultraviolet Variability Experiment (EVE) on the Solar Dynamics Observatory (SDO): Overview of Science Objectives, Instrument Design, Data Products, and Model Developments, Sol. Phys., 275, 115–143

Wuelser, J.-P., Lemen, J. R., Tarbell, T. D., Wolfson, C. J., Cannon, J. C., Carpenter, B. A., Duncan, D. W., Gradwohl, G. S., Meyer, S. B., Moore, A. S., Navarro, R. L., Pearson, J. D., Rossi, G. R., Springer, L. A., Howard, R. A., Moses, J. D., Newmark, J. S., Delaboudiniere, J.-P., Artzner, G. E., Auchere, F., Bougnet, M., Bouyries, P., Bridou, F., Clotaire, J.-Y., Colas, G., Delmotte, F., Jerome, A., Lamare, M., Mercier, R., Mullot, M., Ravet, M.-F., Song, X., Bothmer, V., Deutsch, W., 2004, EUVI: the STEREO-SECCHI extreme ultraviolet imager, in Society of Photo-Optical Instrumentation Engineers (SPIE) Conference Series, (Ed.) S. Fineschi and M. A. Gummin, vol. 5171 of Society of Photo-Optical Instrumentation Engineers (SPIE) Conference Series, pp. 111–122

Zhukov, A. N., Veselovsky, I. S., 2007, Global coronal mass ejections, ApJ, 664, 131–134

Publications

- Mierla, M., Chifu, I., Inhester, B., Rodriguez, L., Zhukov, A., 2011, Low polarised emission from the core of coronal mass ejections, Astronomy and Astrophysics, 530, L1
- Chifu, I., Inhester, B., Mierla, M., Chifu, V., Wiegelmann, T., 2012, First 4D Reconstruction of an Eruptive Prominence Using Three Simultaneous View Directions, Solar Physics, 281, 121-135
- Mierla, M.; Seaton, D. B.; Berghmans, D.; Chifu, I.; De Groof, A.; Inhester, B.; Rodriguez, L.; Stenborg, G.; Zhukov, A. N., 2013, Study of a Prominence Eruption using PROBA2/SWAP and STEREO/EUVI Data, Solar Physics, 286, 241-253
- Chifu, I., Inhester, B., Wiegelmann, T., 2015, Coronal magnetic field modeling using stereoscopy constraints, Astronomy and Astrophysics, 577, 123

Acknowledgements

I would like to thank all my supervisors for their support, Dr. Bernd Inhester, Dr. Thomas Wiegelmann, Prof. Dr. Sami Solanki and Prof. Dr. Karl-Heinz Glassmeier.

I am profoundly grateful to my supervisor Dr. Bernd Inhester. Even though our research group had weekly meetings, Bernd was always reachable and available to discuss any problem I had. He taught us how to tackle the problems from different perspectives. Dr. Bernd gave his insights from various scientific fields and helped us understand our scientific issues. I genuinely am thankful him for his huge patience with me, for extremely careful reading of the papers and this thesis. For me, he is the model of how to be a good scientist.

Thanks, Dr. Thomas Wiegelmann for always being optimistic and supportive during my Ph.D. thesis and always being available to answer all the questions.

The research was conducted at the Max-Planck-Institute for Solar System Research (MPS) in Göttingen. I would like to thank MPS and especially the International Max Planck Research School (IMPRS) for giving me this great opportunity to carry out my Ph.D. studies in a professional environment. I would like to thank the Director, Prof. Dr. Sami Solanki, for offering us a professional working environment where I had the opportunity to model myself as a scientist. I am grateful for the support he offered me during my stay here.

I would like to thank Sonja Schuh, the coordinator of the International Max Planck Research School of Solar System Science, for being so open and always finding time to help me.

Last but not least, I would like to thank my family who always supported me in everything I did. They were always there when I was in trouble, helping me overpass all the difficulties.

This thesis in dedicated to my parents!

Curriculum vitae

Personal data

Name:	Iulia Ana Maria Chifu
Day of birth:	19.07.1980
Place of birth:	Bucharest, Romania

Education

02/2010 - 2014 :	PhD student Max Planck Institute for Solar System Research, Germany Technische Universität Carolo-Wilhelmina zu Braunschweig, Germany
10/2007 - 02/2009 :	M.Sc (Environment protection, Atmospheric Physics and Earth Science) Faculty of Physics, University of Bucharest
10/2003 - 06/2007 :	B.Sc. (Physics) Faculty of Physics, University of Bucharest
10/2000 - 06/2005 :	B.Sc. (Communication and Public Relation) Faculty of Communication and Public Relation “David Ogilvy”, The National School of Political and Administrative Studies

Professional details

08/2007 - present:	Research assistant at Astronomical Institute of Romanian Academy, Solar Physics department, Bucharest, Romania
02/2001 - 02/2002 :	Marketing research operator - Institute of marketing research GFK, Bucharest, Romania
12/2000 - 08/2003 :	Office manager, journalist at the nongovernmental organization Romanian Environmental Journalist Association (REJA) - Perspective magazine, Bucharest, Romania

Prizes

19/12/2013	Stefan Hepites prize awarded by Romanian Academy, Bucharest, Romania